UNIVERSIDADE ESTADUAL DE CAMPINAS
Instituto de Física "Gleb Wataghin"

INGRID DE ALMEIDA RIBEIRO

Mechanical properties of ice I$_h$ and structural and dynamical properties of supercooled water

PROPRIEDADES MECÂNICAS DO GELO I$_h$ E PROPRIEDADES ESTRUTURAIS E DINÂMICAS DA ÁGUA SUPER-RESFRIADA

Campinas
2021

Ingrid de Almeida Ribeiro

Mechanical properties of ice I$_h$ and structural and dynamical properties of supercooled water

Propriedades mecânicas do gelo I$_h$ e propriedades estruturais e dinâmicas da água super-resfriada

Thesis presented to the Institute of Physics "Gleb Wataghin" of the University of Campinas in partial fulfillment of the requirements for the degree of Doctor of Sciences, in the area of Physics.

Tese apresentada ao Instituto de Física "Gleb Wataghin" da Universidade Estadual de Campinas como parte dos requisitos exigidos para a obtenção do título de Doutora em Ciências, na área de Física.

Orientador: Prof. Dr. Maurice de Koning

Este exemplar corresponde à versão final da tese defendida pela aluna Ingrid de Almeida Ribeiro, e orientada pelo Prof. Dr. Maurice de Koning.

Campinas

2021

R354m   Ribeiro, Ingrid de Almeida, 1991-
Mechanical properties of ice Ih and structural and dynamical properties of supercooled water / Ingrid de Almeida Ribeiro. – Campinas, SP : [s.n.], 2021.

Orientador: Maurice de Koning.
Tese (doutorado) – Universidade Estadual de Campinas, Instituto de Física Gleb Wataghin.

1. Gelo - Propriedades mecânicas. 2. Gelo hexagonal. 3. Contorno de grão. 4. Água super-resfriada. 5. Dinâmica molecular. I. Koning, Maurice de, 1969-. II. Universidade Estadual de Campinas. Instituto de Física Gleb Wataghin. III. Título.

Informações para Biblioteca Digital

Título em outro idioma: Propriedades mecânicas do gelo Ih e propriedades estruturais e dinâmicas da água super-resfriada
Palavras-chave em inglês:
Ice - Mechanical properties
Hexagonal ice
Grain boundaries
Supercooled water
Molecular dynamics
Área de concentração: Física
Titulação: Doutora em Ciências
Banca examinadora:
Maurice de Koning [Orientador]
Alex Antonelli
Marcus Aloizio Martinez de Aguiar
Luana Sucupira Pedroza
Rodrigo Moura Freitas
Data de defesa: 13-08-2021
Programa de Pós-Graduação: Física

Identificação e informações acadêmicas do(a) aluno(a)
- ORCID do autor: https://orcid.org/0000-0002-8418-3806
- Currículo Lattes do autor: http://lattes.cnpq.br/8016225566610662

MEMBROS DA COMISSÃO JULGADORA DA TESE DE DOUTORADO DE INGRID DE ALMEIDA RIBEIRO – RA 180522 APRESENTADA E APROVADA AO INSTITUTO DE FÍSICA "GLEB WATAGHIN", DA UNIVERSIDADE ESTADUAL DE CAMPINAS, EM   13 / 08 / 2021.

COMISSÃO JULGADORA:

- Prof.   Dr.   Maurice de Koning – Orientador – DFMC/IFGW/UNICAMP

- Prof.   Dr.   Alex Antonelli – DFMC/IFGW/UNICAMP

- Prof.   Dr.   Marcus Aloizio Martinez de Aguiar – DFMC/IFGW/UNICAMP

- Profa.   Dra.   Luana Sucupira Pedroza – CCNH/UFABC

- Prof.   Dr.   Rodrigo Moura Freitas - DMSE/MIT

CAMPINAS

2021

Dedico este trabalho aos meus pais e aos meus avós.
Vocês são os pilares da minha formação.

Acklowledgements

I thank,

Prof. Maurice de Koning for his orientation, patience and support necessary for the completion of this Thesis. I am extremely grateful for all the constructive criticisms and discussions!

Prof. Valeria Molinero and Prof. Roberto Veiga for the collaboration and many great discussions. I especially thank Valeria for inviting me to participate, even remotely, in her group.

My research group: Jéssica, Pedro, Danilo, Vitor, Rodolfo, and Filipe. Thanks for all the discussions and group meetings!

My friends and colleagues in Unicamp and Barão Geraldo. I am grateful for all the great conversations. Some of you have made these past years very enjoyable!

My husband Leonardo for his companionship, patience and affection every day. With you, everything was much easier! I also thank my parents-in-law, Alzira and Lair, for supporting me. My friend Henrique, for all support and kindness. I thank my mother Adriana, my grandparents Maria Imaculada and Gonçalo, my uncle Júlio César and Léia, for all their support and affection. I also thank my grandparents Otacília and Rivail, and my father Giovani. Even for those who are no longer with us, your honesty and resilience are going to be with me always!

Abstract

Using classical molecular dynamics (MD) simulations with all-atom potentials, we investigate the mechanical properties of ice I_h by observing in detail the deformation mechanisms at the nanoscale. As the second part of this Thesis, we investigate the influence of dynamical effects on the viscosity of supercooled water. At last, we study the methodology of a pulsed heating scheme based on a novel experimental technique to probe supercooled water structure.

In the part related to ice I_h, we study the process of grain-boundary (GB) sliding, and we focus on the $\Sigma 35$ symmetric tilt boundary. In particular, we contrast two cases: one in which the GB interface features the presence of a quasi-liquid layer (QLL) at 250 K and another in which there is not, at 150 K. We find that the QLL significantly facilitates GB sliding. Since GBs are the customary place for impurities in polycrystalline ice I_h, sodium chloride (NaCl) is among the most common impurities found in the microstructure of ice. Thus, we also investigate how the presence of NaCl ions affects the structural and dynamical properties of GBs in ice I_h.

In the second part, we investigate the shear-rate dependence of the viscosity of supercooled water. We show the existence of a distinct cross-over from Newtonian to non-Newtonian behavior characterized by a power-law shear-thinning regime. We find that the viscosity reduction is due to the decrease in the connectivity of the hydrogen-bond network. At last, we perform a theoretical analysis of the experimental technique which uses fast heating pulses to gradually evolve supercooled water from the amorphous side as a way to bypass the rapid ice crystallization at "no man's land". We find that supercooled water can be equilibrated in steps; however, care must be taken when interpreting the structural properties obtained at the glassy state.

Keywords: Ice, Mechanical Properties, Grain-Boundaries, Supercooled water, Molecular Dynamics.

Resumo

Usando simulações de dinâmica molecular (MD) clássica, investigamos as propriedades mecânicas do gelo I_h observando em detalhes os mecanismos de deformação na escala nanométrica. Na segunda parte da Tese, investigamos a influência dos efeitos dinâmicos sobre a viscosidade da água super-resfriada. Finalmente, estudamos a metodologia de uma técnica experimental que usa esquema de aquecimento pulsado para estudar a estrutura da água super-resfriada.

Na parte relacionada ao gelo I_h, estudamos o processo de deslizamento do contorno de grão (GB) e nos concentramos no GB simétrico $\Sigma 35$. Em particular, comparamos dois casos: um onde o GB apresenta a presença de uma camada quase-líquida (QLL) à 250 K e outro no qual não há o QLL, à 150 K. Verificamos que o QLL facilita significativamente o deslizamento do GB. Como os GBs representam o local comum para concentrar impurezas no gelo policristalino I_h, o cloreto de sódio (NaCl) está entre as impurezas mais comuns encontradas na microestrutura do gelo. Assim, também investigamos como a presença de NaCl afeta as propriedades estruturais e dinâmicas dos GBs.

Na segunda parte, investigamos a dependência da taxa de cisalhamento na viscosidade da água super-resfriada. Mostramos a existência de um comportamento Newtoniano e não-Newtoniano caracterizado pela taxa de deformação. Constatamos que a redução da viscosidade se deve à diminuição da conectividade da rede de ligações de hidrogênio. Finalmente, fazemos uma análise teórica de uma técnica experimental que utiliza pulsos de aquecimento rápido para liquefazer o amorfo como uma forma de contornar a rápida cristalização do gelo. Observamos que a água super-resfriada pode ser equilibrada em etapas; entretanto, é preciso ter cuidado ao interpretar as propriedades estruturais do líquido obtidas no estado vítreo.

Palavras-chave: Gelo, Propriedades Mecânicas, Contorno de Grão, Água Super-Resfriada, Dinâmica Molecular.

List of Figures

Contents

Chapter 1

Introduction

1.1 The isolated water molecule

Water has a simple molecular structure, and it is the most plentiful compound found on Earth. Nevertheless, it is capable of forming a liquid with many interesting and unique features that are essential for life and the environment. Many of these unexpected properties of water can be explained by the structure of the water molecule and the characteristics of the atoms it contains.

In order to describe its molecular simplicity, Figure 1.1a) represents the water molecule in equilibrium depicting the "v" shape, and without considering its vibrational motion. It has two hydrogens that are connected to an oxygen through a covalent bond, where the O-H distance is 0.9572 ± 0.0003Å and the angle H-O-H is $104.52 \pm 0.05°$. [1] Regarding the electronic distribution, the two hydrogen atoms share electrons with the

| (a) | (b) |

Figure 1.1: The isolated water molecule. Figure 1.1a) shows the O-H distance and the angle H-O-H. Figure 1.1b) represents the "lone pairs" as well as the region with positive (green) and negative (purple) charge.

oxygen, while there are two pairs of electrons that do not participate in the covalent bond, namely the "lone pairs". In this way, Figure 1.1b) indicates that the purple region has an excess of negative charge, while the green region has an excess of positive charge, but the overall net charge is zero. As a result of water's polarity, the connection between different water molecules is mediated by the hydrogen bond, in which one molecule acts as a proton donor, while the other acts as a proton acceptor. The most notable properties of water and ice, such as the diversity of the phase diagram and the anomalous properties of water, as are going to be discussed in this Thesis, are a consequence of the versatility of the water molecule as to the formation of hydrogen bonds.

1.2 The structure and mechanical behavior of ice

Figure 1.2 shows the solid-liquid phase diagram of water. So far, there are currently 17 experimentally confirmed crystalline phases of ice and several more predicted computationally. [2] In a general way, each ice phase has a very different crystalline structure, and this is a consequence of the unique electronic structure of the isolated water molecule. Ice I_h, or hexagonal ice, is the most common form of ice. It is the one present in the glaciers as well as in the fridge of our houses. This particular form of ice is obtained by cooling water down to temperatures below the melting point T_m, that is 273.15 K or 0 ^{o}C under atmospheric pressure conditions. Apart from ice I_h, on Earth, the other phases can only be found in laboratory, due to the extreme temperature and pressure conditions,
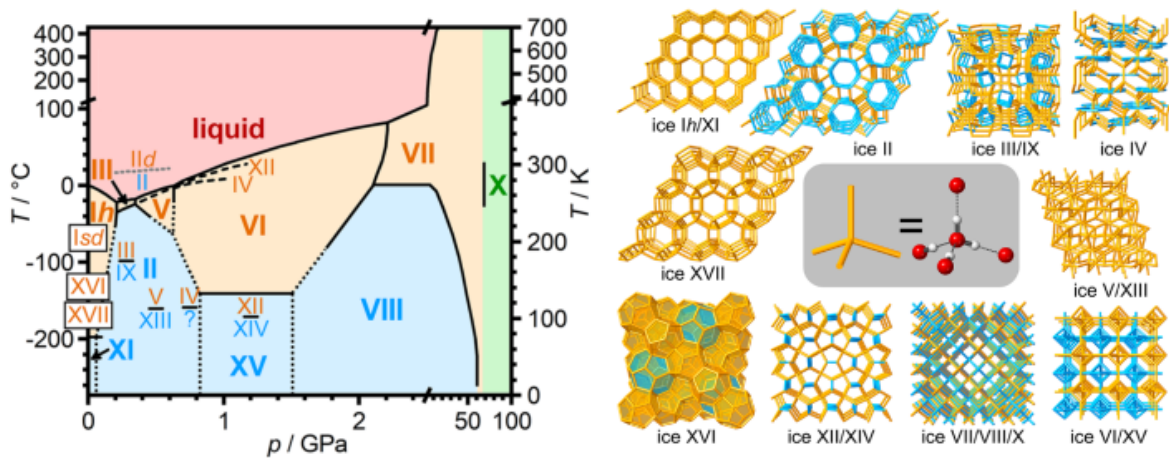
Figure 1.2: On the left is the solid-liquid phase diagram of water showing regions different crystalline phases of water, and on the right it is depicted some of these different structures formed by the oxygen lattice. Figure adapted and reproduced from reference [2].

that are not commonly found in nature. However, there is compeling evidence that other ice phases exist throughout the solar system. [3]

Looking into more detail about the crystalline structure of ice I_h, the oxygen lattice forms an hexagonal diamond structure of the wurtzite type, where each oxygen is tetrahedrally surrounded by other four oxygens. In this particular structure, each water molecule forms four hydrogen bonds, in which two protons are donated and two protons are accepted. On the other hand, hydrogens do not follow any particular orientation, and obey the Bernal-Fowler ice-rules. [4, 5] The first rule states that there are two hydrogens convalently bonded to each oxygen, which means that ice I_h is composed by water molecules. The second rule says that there is exactly one proton between each pair of first neighbor oxygens. Because of this lack of ordering regarding the hydrogen positions, ice I_h is usually called proton-disordered ice I_h.

Due to the relevance of glaciers and ice sheets to the Earth climate, it is fundamental to model and understand how these large ice masses behave. For instance, as shown in Figure 1.3, a glacier is a very large polycrystalline ice that slowly flows over its own weight. In particular, this mechanical deformation process is known as creep, where a material is under a constant stress for a very long period of time, and as a result it flows very slowly. In this context, it is important to study what happens during the flow process at the microscopic level. Another interesting example is sea ice, as also shown in Figure 1.3. When ice is formed from seawater, there are impurities, specially salts, that do not stay in the crystal structure of ice and are rejected during ice formation. As a result, Figure 1.4 shows *in situ* microscopic images of very thin interconnect brine channels of concentrated impurties, and these channels represent the main habitat for sea
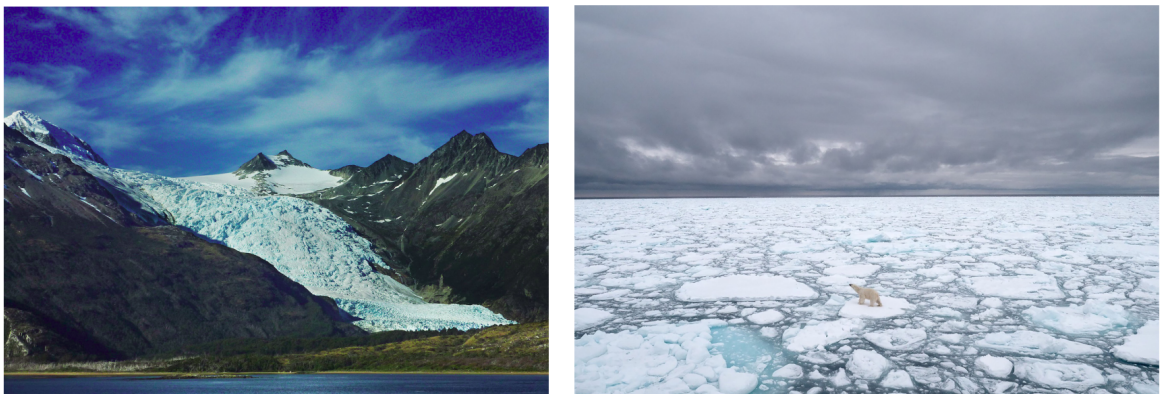
Figure 1.3: A picture of the Holanda glacier in Chile and part of the Arctic ocean in Svalbard, Norway. Reproduced from references [6] and [7].
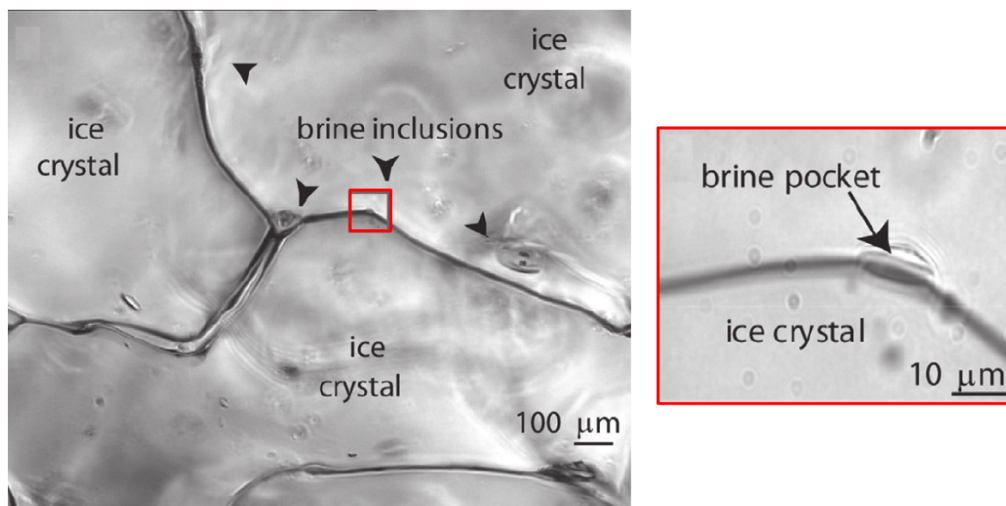
Figure 1.4: Scanning electron microscopy (SEM) image of brine channels in sea ice. Adapted and reproduced from reference [8].

ice microorganisms. How these impurities in the microstructure of ice affects transport properties and the flow process is still an open question.

Regarding the microstructure of any material, a crystal is formed by atoms or molecules arranged in an ordered microscopic structure in order to form a crystal lattice that extends in all directions. A monocrystalline solid is a material in which the atoms form a periodic arrangement throughout its entire volume. By the other hand, when liquid water starts to freeze, the phase change is nucleated from small monocrystals that starts to grow until it forms a polycrystalline structure that can have many different shapes, sizes and orientations. In this manner, the resulting ice contains grains with periodic arrangements of atoms, but the polycrystal as a whole does not have a periodic arrangement, because the periodic pattern is broken at the grain boundaries. Thus, the grain-boundary (GB) is an interface between the grains of a polycrystalline material, and since the atoms in this region do not follow any particular orientation, the grain-boundary is a disordered region. It belongs to a class of crystal defects, and it is considered to be a two-dimensional or planar defect. In ice I_h, the grain-boundary is known to form a network of veins and nodes, and it is also a commonplace for impurities. Nevertheless, it is experimentally challenging to observe what happens at these internal interfaces at the microscopic level. In the modeling of grain-boundaries, there is a model called coincidence site lattice (CSL), with some special orientations as there are an infinite number of possible orientations of two grains relative to each other. In this model, the value Σ represents the ratio between the unit cell volume of the coincident lattice and the generating lattice.
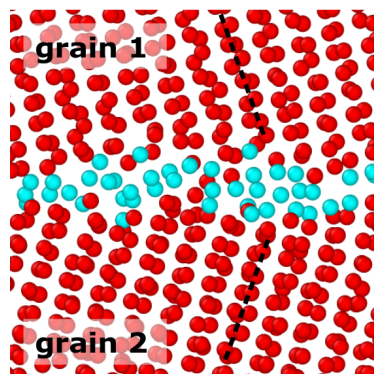
Figure 1.5: Simulation snapshot of a $\Sigma 35$ symmetric tilt grain-boundary in ice I_h at the nanoscale, showing only the oxygens for simplicity. The red spheres represent the crystalline oxygen structure and the cyan spheres represent the disordered region.

Figure 1.5 shows a simulation snapshot of a $\Sigma 35$ symmetric tilt grain-boundary in ice I_h. This particular grain-boundary has been observed in ice I_h experimentally [9, 10], and there is evidence of both experimental [11, 12, 13] and theoretical /computational, [14, 15, 16, 17] that the disordered region displays liquid-like characteristics for temperatures below the melting point.

Regarding the external interfaces of ice, such as the ice-vapor interface, as shown in Figure 1.6, it is an experimental fact that there is a liquid-like (LLL) or quasi-liquid layer (QLL) between ice and vapor, with thickness up to 3 nm for temperatures just below
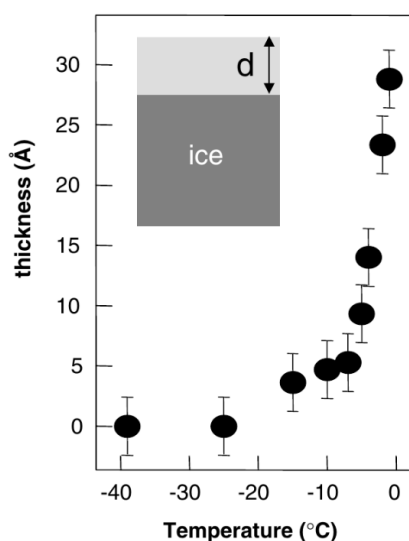
Figure 1.6: Thickness of the quasi-liquid layer that covers the external surface of ice as a function of temperature obtained from x-ray photoelectron spectroscopy measurements. Reproduced from reference [18].
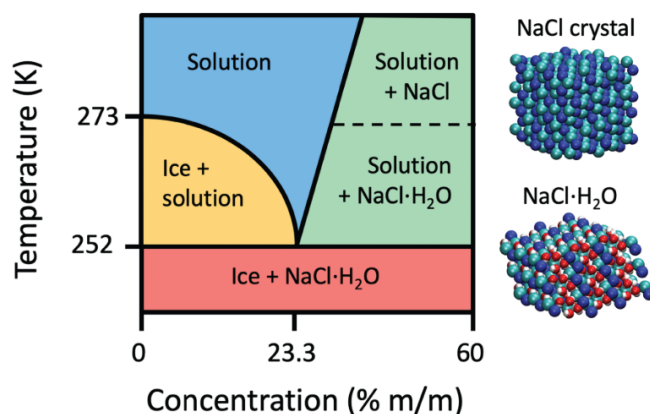
Figure 1.7: Phase diagram of the NaCl aqueous solution. Reproduced from reference [22].

T_m and low as -20 ℃. The wording "liquid-like" or "quasi-liquid" relating to the fact that the properties of this superficial liquid are manifestly different from those of bulk supercooled liquid water. This very thin external QLL is known to make the surface of ice slippery. Since there is also evidence of internal QLLs, it is still an open question if it could ease the process of grain-boundary sliding, by which two crystal grains slide relative to each other along the GB interface. This is relevant information because the process of grain-boundary sliding is a fundamental mechanism for mechanical deformation processes of polycrystalline ice.

Among the salts and impurities present in seawater, almost 87 % is represented by sodium chloride (NaCl) [19]. In this context, it is important to study the effect of NaCl at the brine channels inside polycrystalline ice I_h. As illustrated in Figure 1.7, above the melting point and considering low concentrations of NaCl, the bulk NaCl solution is in the liquid phase. At higher concentrations, saturation leads to the formation of NaCl crystals for temperatures above 273 K and NaCl·2H2O known as crystalline sodium chloride dihydrate for temperatures below 273 K. Between the freezing point and the eutectic temperature of $\sim$ 252 K, the system will consist of almost pure polycrystalline ice in equilibrium with brine. [20] When the temperature falls below the eutectic temperature, on the other hand, the eutectic reaction results in the transformation of brine into ice and NaCl·2H$_2$O. In ice I_h, nuclear magnetic ressonance (NMR) experiments suggest that this liquid-like behavior of these so-called quasi-brine layers (QBL) [21] persist even at $\sim$ 20 K below the eutectic point for which, in bulk equilibrium, all NaCl would have precipitated as crystalline sodium chloride dihydrate. [21] Thus, it is an open question how the presence of NaCl affects the structural and dynamical properties of internal interfaces in ice I_h.
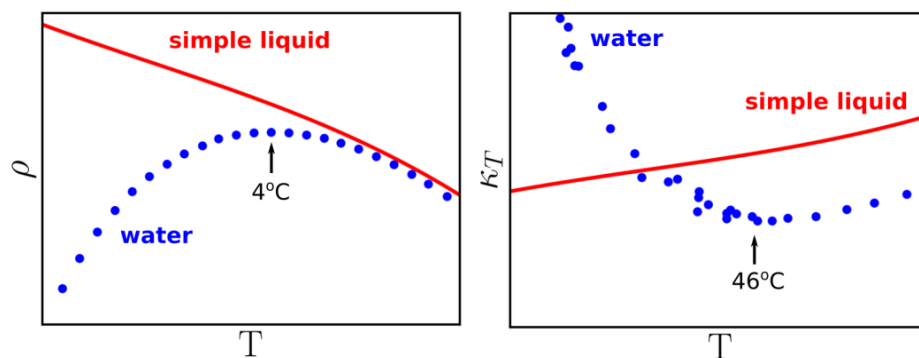
Figure 1.8: Density ρ and isothermal compressibility k_T as a function of temperature for simple liquids and water. Adapted and reproduced from reference [23].

1.3   Fundamental properties of supercooled water

It is known that a lot of water properties display unusual behavior when compared to other liquids. More precisely, there are 41 water anomalies that have been reported so far. [24]. For instance, with respect to thermodynamic response functions, Figure 1.8 shows that, for simple liquids, such as ethanol, as the temperature decreases, the density ρ increases. Meanwhile, water shows a maximum at about 4 ^oC. As a second example, while the isothermal compressibility k_T decreases as the temperature decreases for simple liquids, water shows a minimum at about 46 ^oC. In both examples, an apparent divergence appears as the temperature decreases, and there is a lot of experimental/theoretical evidence that these different behavior become intensified for lower temperatures.

Figure 1.9 shows a different phase diagram of water when compared to Figure 1.2. In the low pressure region of the diagram, if water is cooled down to temperatures below 0° C, in such a way that, it still remains liquid, water becomes what is known as super-cooled water. The supercooled state is a metastable state, meaning that it corresponds to a stable state, but it is not the system's state of least energy. Thus, supercooled water is thermodynamically less stable than ice. Additionally, if water is cooled down extremely fast to much lower temperatures, that is temperatures below the glass transition temperature ($T_g \sim$136 K), it becomes the low density amorphous (LDA) ice. The amorphous ice or glassy water represents a nonequilibrium state of matter. It is solid as ice I_h, but there is no crystalline order because its structure is very similiar to that of the liquid. In the timescale of experimental measurements, it is challenging to perform any kind of measurement of supercooled water before the liquid freezes. There is largely experimental evidence missing at the region called "no man's land" due to the rapid crystallization
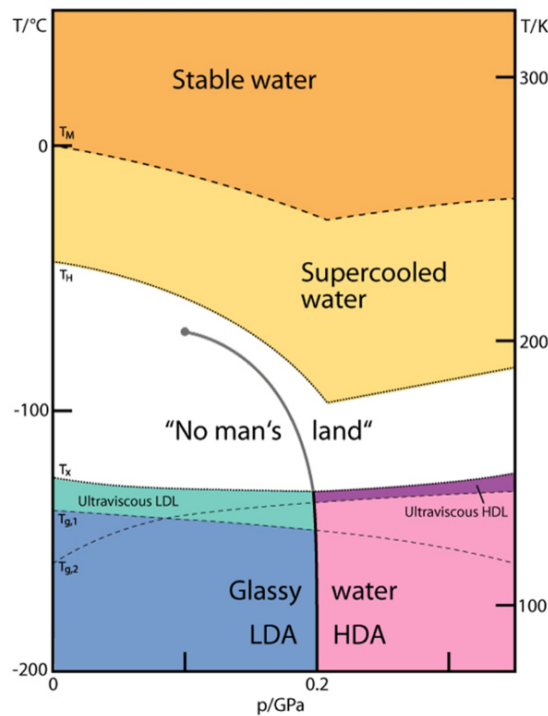
Figure 1.9: Water phase diagram showing the noncrystalline phases. Reproduced from reference [23].

kinetics.

There is a lot of theoretical/experimental investigation regarding the thermodynamic properties of water, but little is known about the flow characteristics of water, specially in its supercooled state. Viscosity is a measure of a fluid's resistance to flow. It is an experimental fact that viscosity of glass-forming liquids increases dramatically upon cooling, until dynamical arrest when a glassy state is reached. As it describes the internal friction of a moving fluid, it also brings additional information regarding the chemical bonds. The potential energy landscape (PEL) [25, 26, 27] is a concept to help understanding the physical picture of supercooled liquids and glasses. For a liquid in three dimensions, each possible configuration is represented by a point over the PEL, and the dynamics of the system can be thought of as the motion of this point over the PEL. The local minima of the PEL correspond to locally stable configurations of the particle system, and the absolute minimum is the crystal. [28] At high temperatures, the PEL of a liquid is composed by basins separated by energy barriers of equal size. As the temperature decreases and approaches the glass transition temperature T_g, the basins may become separated by energy barriers of different size. The size of these energy barriers is related to the cost of breaking and forming chemical bonds. As a connection between dynamics
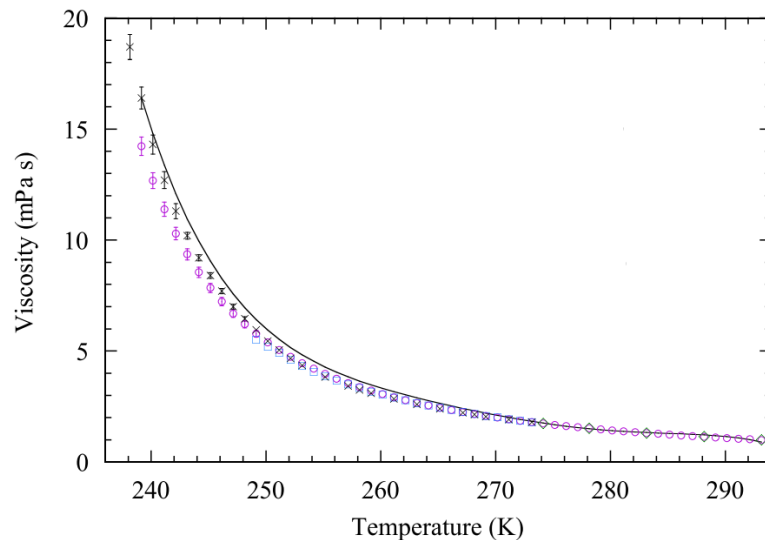
Figure 1.10: Experimental measurements of the viscosity of water for different temperatures, including the stable and the supercooled region, obtained from Brownian motion of spheres suspended in water. Reproduced from reference [30].

and thermodynamics of glass-forming liquids, based on a phenomenological description, the viscosity displays an Arrhenius behavior, $\eta = \exp(E_A/k_B T)$, if the size of the energy barriers E_A is always the same independently of the temperature. In this case, according to the classification originally proposed by Angell [29], the liquid is classified as strong. On the other hand, if E_A is not constant, and the PEL displays energy barriers of different size, the viscosity significantly deviates from the Arrhenius behavior, and the liquid is classified as fragile.

Water is known to be a poor glassformer, and the supercooled liquid crystallizes easily, making the measurement of its viscosity a challenging task. Figure 1.10 shows experimental measurements of supercooled water's viscosity for different temperatures, including the supercooled state. The viscosity η of a viscous fluid is defined as the proportionality constant between the shear stress σ and the corresponding strain rate $\dot{\gamma}$ according to $\sigma = \eta \dot{\gamma}$ [31, 32]. If, for given temperature and pressure, the relation between σ and $\dot{\gamma}$ is linear, i.e., η is constant, the flow behavior of the fluid is said to be Newtonian [32]. When this linearity is violated the flow behavior is referred to non-Newtonian. Many fluids display Newtonian flow behavior for sufficiently small rates $\dot{\gamma}$. Liquid water in thermodynamic equilibrium is an example, with a viscosity that is known to be constant across several orders of magnitude of $\dot{\gamma}$ [33]. Much less is known, however, about the dynamical effects on the viscosity of water in its supercooled state, and the question as to whether it displays a shear-rate dependence remains open.

Several theories have been proposed to explain the anomalous thermodynamic behavior of water. [34, 35, 36] One of the popular theories to explain the origin of water anomalous behavior is related to the theoretical liquid-liquid critical point (LLCP). [34] Using molecular dynamics simulations based on the ST2 model of water, Poole et $al.$ found a first-order phase transition from low-density liquid (LDL) to high-density liquid (HDL) with an LLCP located at T_c ~235 K and P_c ~200 MPa, with the LDL exhibiting more ice-like local order, while HDL leading to perturbed hydrogen-bonding and higher density. In this scenario, the liquid-liquid phase transition (LLPT) is determined by extending the high-density amorphous (HDA) and the low-density amorphous (LDA) first-order phase transition into the higher temperature and lower pressure region of the phase diagram, as illustrated in Figure 1.9. The proposed liquid-liquid transition line terminates at a critical point in the supercooled region. Thus, the anomalous behavior of thermodynamic response functions in supercooled water is attributed to the hypothetical LLCP at which the response functions should diverge, while at the one-phase region located at low pressures, the response functions show maxima. Away from the hypothetical LLCP at low pressures, liquid water may consist of a fluctuating mixture of molecules with local ordering similar to those found in LDL and HDL, with pronounced structure fluctuations close to the Widom line, at which the correlation length reaches its maximum value.

In the one-phase region located at low pressures, based on different water models, and a variety of criteria to sort the water molecules into two different categories depending on their local structures [37, 38, 39, 40, 41, 42], computer simulations show a sigmoid-like dependence of each component with respect to the temperature, that is the structure of the liquid changes dramatically at some point. [38] At ambient conditions, it is experimentally challenging to verify these local components in water, because such structural motifs would form and disappear very fast due to large thermal fluctuations. On the other hand, even with slower water dynamics in the supercooled region, it is difficult to overcome the rapid crystallization kinetics in the timescale of the experimental measurements. To overcome this difficulty, there have been many recent experimental attempts to probe supercooled water properties in the temperature region known as "no man's land", that is above ~160 K and below ~230 K. [43, 44, 45, 46, 47, 48] Recently, Kringle et $al.$ used a laser heating scheme, as illustrated in Figure 1.11, to study the structural and relaxation properties of deeply supercooled water [43, 44]. Basically, a ~15 nm water film on Pt(111) or graphene/Pt(111) with the structure of low-density amorphous (LDA) ice is prepared by vapor deposition at 70 K, followed by annealing at a temperature just below the glass transition T_g ~ 136 K. The LDA film is then repeatedly heated to a temperature T_{max}
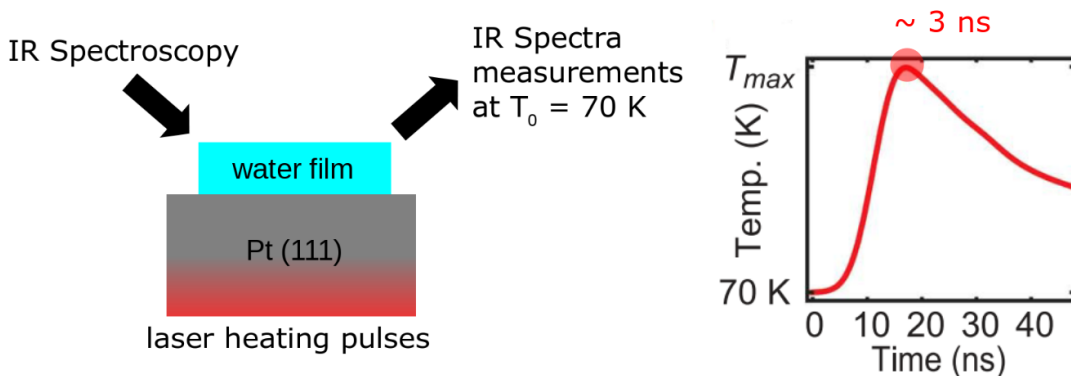
Figure 1.11: Pulsed laser heating system to evolve the water film structure and the temperature evolution in a single heat pulse. Adapted and reproduced from reference [43].

with nanosecond laser pulses with heating rates greater than 10^9 K/s. For each pulse, the films spent $\sim$3 ns near T_{max}, where the sample is supposed to be in the liquid state, and then the system is quenched to the base temperature $T_0 = 70$ K with cooling rates also greater than 10^9 K/s. After quenching, the system stays at the glassy state for a much larger period of time, about 1 s during which its structure is interrogated with infrared spectroscopy to assign the fraction of water molecules with vibrational signals of ice, LDA and high temperature liquid water. The fast heating and cooling pulses are repeated for a finite number of times while the evolution of the film is followed at $T_0 = 70$ K. This procedure allows for a decoupling of the measurement time at T_0 from the relaxation time at T_{max}. The use of this methodology to derive properties of liquid supercooled water is based on two assumptions. First, that evolving the film through a series of pulses that transiently heat water to near T_{max}, is equivalent to evolving the film in an isothermal experiment during a time that corresponds to the sum of those of the heating pulses. Second, that the quenched IR spectra measured at T_0 reflects the steady-state structure of water at T_{max}. To date, the validity of these assumptions has not been verified.

1.4   Molecular dynamics

Molecular dynamics (MD) simulations provide a set of computational tools that make it possible to follow the trajectories of atoms. The methods used in MD calculate the behavior of a molecular/atomic system over time, and in this way it is possible to investigate the structure, dynamics, and thermodynamics in liquid, solid, and gas

phases. [49, 50, 51]

As computational speed is a particular concern when describing condensed phase systems, meaning that real systems will consist of hundreds of thousands or millions of atoms, some approximations and simplifications must be made. Classical molecular models usually consist of point particles carrying mass and electric charge. As for the practical aspects, the geometry of the system as well as the number of particles must be defined. Since it is impractical to contain system with millions of atoms, periodic boundary conditions allow one to simulate nanoscale systems with accurate estimation of bulk properties. Thus, the initial positions and velocities allow to define the initial conditions needed for the solution of the equations of motion. In particular, the initial velocities are randomly assigned in a way to obtain the Maxwell-Boltzmann distribution at the desired temperature. Even though velocities are assigned according to the correct distribution, a thermostat is needed in order to to add or remove heat from the system, and maintain a certain target temperature. Based on a thermodynamic concept, the temperature of a MD simulation is usually calculated using time-averaged kinetic energies according to the equipartition theorem

$$\frac{3}{2}Nk_BT = \left\langle \sum_{i=1}^{N} \frac{1}{2}m_iv_i^2 \right\rangle, \tag{1.1}$$

where N is the total number of particles, k_B is the Boltzmann constant, T is the temperature of the system, m_i is the particle mass, and v_i is the instantaneous velocity of each particle.

In laboratory experiments, thermodynamic properties of interest are usually measured under more controlled conditions, such as constant temperature and pressure. In MD simulations, the temperature and pressure of the system are controlled through the use of thermostats and barostats, and one must choose a particular thermodynamic ensemble, such as the microcanonical (NVE), canonical (NVT), isothermal-isobaric (NPT) or isoenthalpic-isobaric (NPH) emsemble, to sample a particular state defined by a target energy, temperature, and pressure.

Thermostat algorithms basically work by altering the Newtonian equations of motion, and they can be either deterministic or stochastic depending on whether or not random numbers are used to guide the dynamics. To name a few, there is simple the velocity rescaling [52], Nosé-Hoover [52], and Langevin [53] thermostats, for the first two

being deterministic, and the latter being stochastic. In the velocity rescaling method, the momenta of the particles are simply rescaled to match the target temperature, and in this case, it is designed to sample the isokinetic ensemble rather than the canonical one. The Nosé-Hoover thermostat adds a thermal bath by including a Hamiltonian with an extra degree of freedom. This fictitious degree of freedom has a "mass" that can be changed to interact with the particles while maintaining the canonical ensemble. In many simulation packages, the choice of "mass" of the fictitious particle is expressed as a time damping parameter, and affects the fluctuations that will be observed. The Langevin thermostat alters the equations of motion with Brownian dynamics, by including random collision forces, to mimic what happens in a solvent. Addressing the Langevin formalism in more detail, the equation of motion of each particle is described by

$$
\frac{d\mathbf{r}_i(t)}{dt} = \frac{\mathbf{p}_i(t)}{m_i},
$$
$$
\frac{d\mathbf{p}_i(t)}{dt} = F_i(t) - \gamma \mathbf{p}_i + \mathbf{R}_i(t),
$$

(1.2)

where $\mathbf{r}_i$ and $\mathbf{p}_i$ represent the cartesian position and the linear momentum of each particle, respectively, m_i is the particle mass, F_i is the resulting force on particle i, γ is the friction coefficient that represents a damping viscosity due to the fictitious particles of the thermal bath, and $\mathbf{R_i}$ is a random force related to the collisions with the fictitious particles. Such random forces are classified to be what is called white noise, that is $\langle R \rangle = 0$ and $\langle R(0)R(t) \rangle = \delta(t)$.

In a NPT or NPH simulation, when the dimensions of the simulation box fluctuate around constant values, the simulation is said to have equilibrated to a specific volume. The pressure of a MD simulation is commonly computed using the virial theorem

$$
PV = Nk_BT - \frac{1}{3k_BT} \sum_{i=1}^{N} \sum_{j=i+1}^{N} r_{ij} \; f_{ij},
$$

(1.3)

where P is the pressure, V is the volume, N is the total number of particles, k_B is the Boltzmann constant, T is the temperature of the system, r_{ij} is the distance between particle i and j, and f_{ij} represents the interatomic force between i and j.

Similar to thermostats, a barostat algorithm is needed to sample the isothermal-isobaric or the isoenthalpic-isobaric ensembles. In the Andersen [54] barostat, the system is coupled to a fictitious pressure bath, by adding an additional degree of freedom to the

equations of motion, similar to the Nosé-Hoover thermostat. This particular barostat can only control the pressure isotropically, and can be applied to liquid or gas phases, which have no well defined shape. The Parrinello-Rahman [55] barostat is an extension to the Andersen barostat, as it supports the anisotropic scaling of the size and shape of the simulation box, and can be quite useful in solid simulations.

When considering electrostatic interactions, pairwise distances represent an expensive computation that grows with the square of the number of atoms involved. As the Coulombic interactions fall off only very slowly with distance, that is r^{-1}, to calculate all Coulomb interactions over a periodic system simulations is expensive. Fortunately, there are special techniques such as the Particle-Particle Particle-Mesh (PPPM) [56] method to deal with these long-range interactions with accuracy and reduced computational cost.

A sofisticated set of classical MD algorithms is already implemented in the Large-scale Atomic/Molecular Massively Parallel Simulator (LAMMPS) package. [57] All simulations performed in the work of this Thesis were obtained through LAMMPS.

1.5   Water models

In the modeling of water using classical MD, there are numerous proposed models, to name a few: SPC/E, mW, TIP4P/Ice, TIP4P/2005, TIP5P [58, 59, 60, 61, 62, 63]. In general, the parameters of these models are determined from *ab initio* calculations, experimental results, or a combination of these. Thus, the MD simulations technique aligned with a statistical approach to the interpretation of molecular data, make it possible to predict physical properties of the water phases.

In particular, the potentials used in this Thesis, are based on the transferable intermolecular potential with 4 points (TIP4P). Additionally, it is much more computationally efficient to freeze the internal degrees of freedom and treat the molecule as a rigid body. As depicted in Figure 1.12, the water molecule is described as a rigid body, with each molar mass placed at fixed distances. In order to impose such geometrical constraints in Newton's equation of motion, the SHAKE algorithm [64] is responsible to add a constraint force, which makes the intramolecular bond lengths and angles fixed in the MD simulations. The intermolecular interations in this model consists of the Coulomb interaction
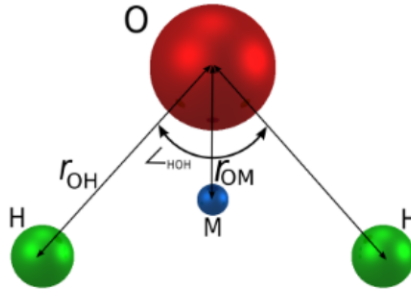
Figure 1.12: Schematics of the TIP4P model showing the hydrogens (green), the oxygen (red), and the massless charge site (blue). The r_{OH} distance is 0.9572 Å, the HOH angle is 104.52^o, and the r_{OM} distance is 0.15 Å. There are charges of +0.52 on the hydrogens and -1.04 on the massless charge site. Reproduced from reference [65].

between the charged sites and a single Lennard-Jones term between the oxygens

$$V_{ab} = \sum_{i}^{on\ a}\sum_{j}^{on\ b} \frac{q_i q_j}{r_{ij}} + \frac{A}{r^{12}} - \frac{B}{r^6}, \tag{1.4}$$

where q is the charge, and A and B are constants, and r is the distance between two particles. In general, these parameters are varied in order to reproduce some of the physical properties of water. Both models, TIP4P/Ice and TIP4P/2005, are a reparametrization of TIP4P. Even with great agreement with respect to some properties, such as density, melting point, diffusion coefficients, and shear viscosity, still these models fail to reproduce all known properties of water.

1.6   Objectives

As mentioned in some examples in Section 1.2, the molecular mechanisms behind processes such as the flow process of large ice masses are still not well understood. Although good progress has been made to understand the properties of ice, in general, the physics of ice still needs to be extensively studied at the molecular scale especially with regard to mechanical properties due to its environmental impact. Therefore, a fundamental understanding of what happens at the molecular level at interfaces is important for understanding macroscopic behavior. The major challenge is to study these types of interfaces experimentally. Thus, the aim of this Thesis is to investigate the structure and dynamics of grain boundaries in I_h ice using a computational approach through atom-

istic simulations. The chosen form of approach is based on classical molecular dynamics (MD) simulations, which allow a microscopic analysis that cannot be performed through laboratory experiments. In Chapter 2, we will show the study related to the process of grain-boundary sliding in ice I_h. We focus on the $\Sigma 35$ symmetric tilt boundary, which has been observed experimentally in polycrystalline samples, and employ the explicit-proton TIP4P/Ice model to describe the interactions between the water molecules. In Chapter 3, we will present the study related to the effect of sodium chloride on internal quasi-liquid layers in ice I_h. In this study, we focus on the same $\Sigma 35$ symmetric tilt boundary, and we employ the explicit-proton TIP4P/2005 model to describe the interactions between the water molecules, and the approximation of scaled charges for the ions.

Related to the part more specific to liquid water, atomistic simulations can serve as an alternative if performing the experiment in a conventional laboratory is very difficult or even impossible. As mentioned in Section 1.3, the viscosity of supercooled water has been a subject of intense study, in particular with respect to its temperature dependence. Much less is known, however, about the influence of dynamical effects on the viscosity in its supercooled state. In Chapter 4, we address this issue for the first time, using molecular dynamics simulations to investigate the shear-rate dependence of the viscosity of supercooled water as described by the TIP4P/Ice model.

Computer simulations can be considered as a complementary tool to the conventional laboratory in the sense that it offers the power of interpretation in the analysis of the results obtained in a realistic experiment. In chapter 5, we will exhibit results related to the theoretical validation of a novel experimental technique to probe supercooled water structure by the pulsed heating technique starting from the amorphous side of the phase diagram, as mentioned in Section 1.3. In particular, we employ the explicit-proton TIP4P/Ice model to describe the interactions between the water molecules.

Finally, in Chapter 6 we will sumarize the main conclusions of this Thesis and briefly discuss the future perspectives.

Chapter 2

Grain-boundary sliding in ice I$_h$: tribology and rheology at the nanoscale

2.1 Introduction

Starting with Michael Faraday's nineteenth-century reports on regelation, [66, 67] the interfacial properties of water ice have been the subject of intense scientific scrutiny that persists to this day. [68, 69, 70, 71, 72, 73] The ice-vapor/air surface is one of the most investigated interfaces involving ice crystals, being involved in a wide variety of atmospheric phenomena, including cloud electrification [20] and a diversity of chemical reactions associated with enhanced proton activity. [68, 69, 70, 71] A further intriguing characteristic is the presence of the so-called quasi-liquid or liquid-like layer on top of the interface, even at temperatures up to 40 K below the melting point, [11, 74, 75, 76, 77] with the wording "liquid-like" relating to the fact that the properties of this superficial liquid are manifestly different from those of bulk supercooled liquid water.

One of the consequences of the presence of the liquid-like layer on the crystalline ice surface is that it fundamentally affects the friction in processes in which a sliding object is moving across an ice surface. [78, 79] In fact, along with substantial phenomenological

data on macroscopic scales, [80, 81, 82] a recent experimental study [83] was able to bridge the gap between macroscopic and nanoscale tribometry, establishing that the mechanical behavior of the QLL on the ice-vapor/air surface is characterized by a complex rheological response, with a viscosity that is two orders of magnitude larger than that of pristine liquid water. [84]

These observations raise the question whether such disordered interfacial layers may also be involved in sliding processes at other kinds of ice surfaces. In particular, there is compelling evidence, both experimental [11, 12, 13] and theoretical/computational, [14, 15, 16, 17] that a liquid-like disordered layer also exists at the *internal* interfaces of polycrystalline ice samples, as formed by grain boundaries (GBs). [85, 86, 87] Not only are such internal interfaces commonplace in the polycrystalline structure of large ice masses such as glaciers and ice sheets, the process of GB sliding, by which two crystal grains slide relative to each other along the GB interface, is one of the fundamental mechanisms for mechanical deformation of such systems. [88] In this light, GBs and the presence of disorder in their vicinity may be directly involved in a number of geophysical phenomena, including the dynamics of ice sheets and the flow of glaciers. [11, 89]

Even so, relatively little is known about GB sliding in ice. Experimental data is very scarce [90, 91] and the interpretation of the results in terms of molecular processes is mostly indirect. In this scenario, molecular simulation techniques serve as a useful complementary approach, providing a tool for *in situ* computational "microscopy" that is helpful in the identification of molecular-level unit mechanisms that control mechanical response. [92, 93] In this light, the purpose of the present chapter is to apply such techniques to obtain molecular-level insight into the response of the GB region in sliding processes in proton-disordered ice I$_h$. In particular, we focus on the coincident-site-lattice (CSL) [85] $\Sigma 35$ symmetric tilt boundary, which has been observed experimentally [9, 10] and features a liquid-like layer in the vicinity of the melting point. [16] While it is known that this layer displays glassy-like diffusive behavior [16] and a viscosity that is much larger compared to that on the ice-vapor surface [17], there is essentially no insight as to what happens during dynamic processes in which adjacent crystal grains slide past each other. Cao *et al.* [94] have recently carried out similar simulations but their setup involves special bi-crystal arrangements that maintain crystallinity up to the GB dividing plane. Here, we assess the behavior of the disordered GB layer as a function of temperature, sliding velocity as well as direction, quantifying the rheological and tribological response in the sliding process.
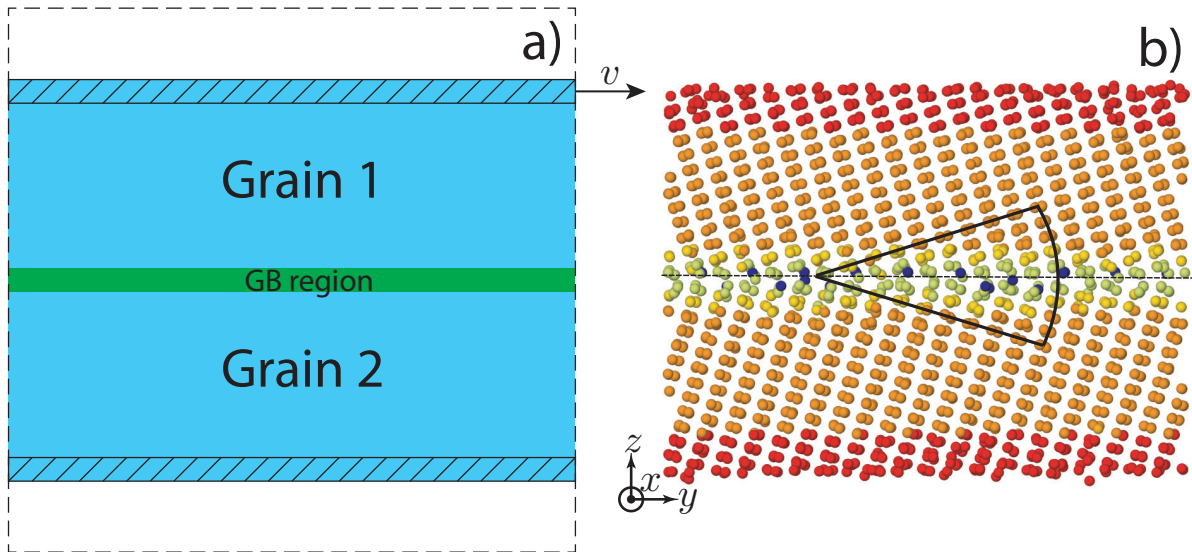
Figure 2.1: a) Set-up of computational cell employed in sliding simulations. Cell is periodic in all three directions, with contour depicted by dashed lines. Areas of vacuum are included to guarantee a single contact interface during sliding simulations. Motion of molecules in shaded regions are constrained during sliding process. While molecules in the bottom region are held fixed, those in the top shaded areas move with a fixed velocity v in a direction parallel to the GB surface region. b) Typical molecular structure of bi-crystal cell containing $\Sigma 35$ symmetric tilt boundary, showing only oxygen atoms. Oxygens in red correspond to those in the two constrained regions. Remaining colors indicate different crystalline environments as determined using the IDS order parameter (see text), with orange indicating hexagonal diamond (HD) surroundings, yellow representing HD first neighbor and green indicating HD second neighbors. Blue oxygens are those classified as disordered.

2.2 Computational details

2.2.1 Computational cell

All simulations of the GB sliding process are based on a bi-crystal cell set-up as depicted schematically in Fig. 2.1a). The contour of the computational cell is depicted by the dashed lines and it is periodic in all three directions. In addition to the two crystal grains, the cell contains an area of vacuum to configure a grain sliding process in which there is only one direct contact interface between both grains, i.e., that of the GB region. The motion of the molecules located in the shaded areas of both grains is constrained, as described in more detail below.

Figure 2.1 b) displays a typical molecular structure of the $\Sigma 35$ symmetric-tilt GB in ice I$_h$ considered in this work, showing only the oxygens. The cell measures approx-

imately 7.6 nm $\times$ 7.5 nm $\times$ 5.4 nm, containing 10800 water molecules. This particular CSL GB is characterized by a rotation of 34.05^o about the $\langle\overline{1}100\rangle$ direction and a $(11\overline{2}\overline{1})$ intersection plane, [9, 10, 95] giving rise to the familiar kite structure often seen for tilt GBs. [96, 97, 98] The cells have been prepared as described in Ref. [16], producing fully proton-disordered configurations. The oxygens shown in red are those that are part of the constrained regions, whereas the other colors represent local crystallinity determined by the `Identify-diamond-structure` (IDS) order parameter [99] as implemented in the Open Visualization Tool (`Ovito`) package. [100] Whereas orange, yellow and green represent crystalline environments associated with hexagonal diamond (HD), HD first neighbor and HD second neighbor, respectively, the blue oxygens are those classified as belonging to disordered surroundings. The IDS order parameter uses the relative positions of neighboring oxygen atoms, and the identification is based on the characterization of the geometric arrangement of second nearest neighbors.

2.2.2 Water model

To describe the interactions between the water molecules we employ the rigid-molecule TIP4P/Ice model [61], which is among the best explicit-proton models for water. [101, 102] It has a melting temperature of T_m = 271 K [103] that is close to the experimental value and it has reproduced the presence of a QLL on free surfaces of ice. [103, 104] The motivation for using an explicit-proton water model instead of the computationally cheaper coarse-grained descriptions in which hydrogen bonding is handled implicitly [60, 94, 105] is that the latter type has been shown to give an excessively ductile kinetics for mechanical deformation processes for ice I$_h$. [104, 106]

2.2.3 Equilibration

Prior to the sliding simulations, the GB cells are first equilibrated. To this end, a vacuum layer is added along the z-coordinate displayed in Fig. 2.1a) by increasing the length of the periodic cell repeat vector perpendicular to the GB region. The thickness is chosen to be 10 nm which is more than twice the distance between the top-most and bottom molecular layers in the cell. Subsequently, the system is relaxed without any constraints at zero external pressure and constant temperature through the anisotropic NPT ensemble as implemented in the `LAMMPS` molecular dynamics (MD) package,[57]

using a Parrinello-Rahman-type barostat [55, 107, 108] and a Langevin thermostat [53] with damping parameters of 2 ps and 0.2 ps, respectively. The corresponding equations of motion are integrated using a time step of 2 fs. The long-range intermolecular electrostatic interactions for the TIP4P/Ice model are handled using the particle-particle particle-mesh (PPPM) scheme [56] and the intramolecular bond lengths and angles are held fixed using the SHAKE algorithm. [64] The equilibration runs have a duration of 10 ns, which is sufficient for full relaxation of all molecular coordinates, stress components and the temperature.

2.2.4 GB sliding simulations

Using the geometries obtained after the initial equilibration, the GB cells to be used in the sliding simulations are prepared by implementing the following modification. We define two subsets of molecules that will have their motion constrained during the sliding simulations (marked as the shaded regions in Fig. 2.1a). In particular, they are the groups of molecules located in slabs with a thickness $\Delta z \simeq 7$ Å at the top and bottom of the GB configurations, respectively, each containing approximately 1500 molecules. A typical case is shown as the oxygens in red in Fig. 2.1 b).

The sliding process is implemented by rigidly moving the molecules in the top slab with a constant velocity in a direction parallel to the GB region. In particular, the time evolution of the x and y coordinates of the molecules i in the top slab is imposed to be

$$\begin{pmatrix} x_i(t) \\ y_i(t) \end{pmatrix} = \begin{pmatrix} x_i(0) \\ y_i(0) \end{pmatrix} + \begin{pmatrix} v_x \\ v_y \end{pmatrix} t, \tag{2.1}$$

where $x_i(0)$ and $y_i(0)$ are their initial values and v_x and v_y are the components of the imposed velocity. The absolute values of the sliding velocities are 0.1 m/s, 1.0 m/s and 10 m/s. The z coordinates of the molecules are allowed to evolve freely during the process to relieve possible normal stresses. In contrast, the positions of the molecules in the bottom layer are held fixed during the process. The remaining molecules evolve under conditions of constant temperature, controlled by a Langevin thermostat [53] with a damping parameter of 0.2 ps, and a fixed cell geometry. The corresponding equations of motion as implemented in `LAMMPS` are integrated using a time step of 1 fs. By monitoring the individual velocities, apart from the thermal vibrations, there was no temperature gradient observed along the z-axis. All the stress components were calculated based on

the standard virial definition [109].

2.3   Results and discussion

Figure 2.2 displays a typical evolution of the system during a sliding simulation at a temperature of 250 K, for which the disordered GB layer is liquid-like. Fig. 2.2a) displays the equilibrated initial condition, showing only the oxygen atoms, with the green-colored rows serving as references to visualize the relative displacements of both grains and the remaining colors indicating the crystalline environment according to the same scheme as in Fig. 2.1 b). The blue-shaded area depicts the extent of the region containing molecules in a non-crystalline environment, as determined by applying the polyhedral-surface-mesh algorithm [110] on the set of oxygens that have been labeled as non-crystalline by the IDS order parameter. Fig. 2.2 b) then shows the structure after the top layer has been displaced by 4nm in the y direction at a velocity of 0.1 m/s. The green-colored reference rows clearly show that the imposed motion of the constrained top layer leads to GB sliding, with the top grain moving to the right with respect to the lower one. A further observation is that the thickness of the disordered region in the vicinity of the GB has
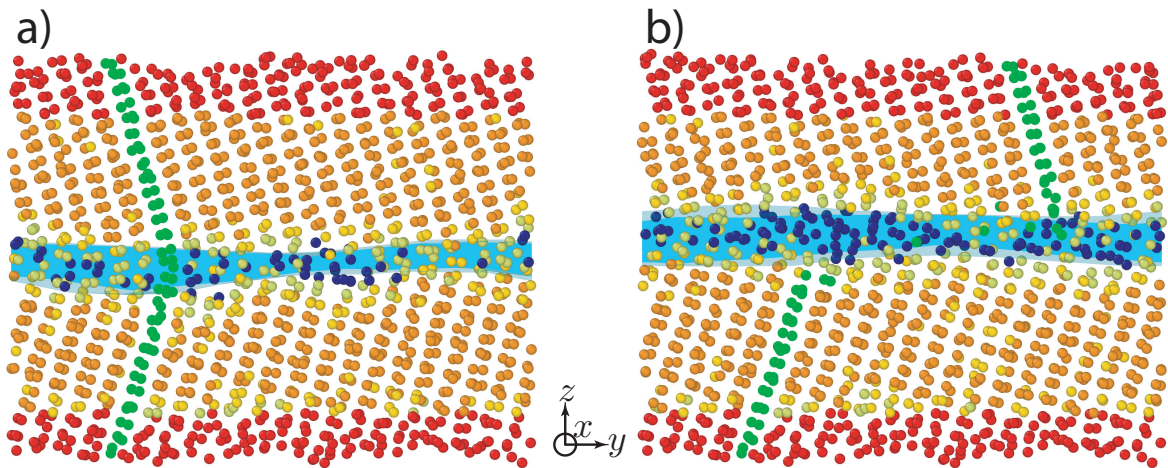
Figure 2.2: Typical evolution of system during sliding simulations, displaying only oxygen atoms. Oxygens colored in green serve as references to visualize relative displacement of grains. Red oxygens belong to constrained slabs (see text). Remaining colors indicate crystalline environment according to the same scheme as in Fig. 2.1 b). Blue-shaded areas depict extent of the regions containing molecules in a non-crystalline environment, as determined using the polyhedral surface mesh algorithm [110] implemented in OVITO. [100] (a) Initial configuration at 250 K, prior to sliding protocol. (b) Snapshot after top slab has moved by 4 nm along y direction at a velocity of 0.1 m/s.

increased compared to the initial equilibrium configuration and that, in this particular case, the lower grain has grown somewhat at the expense of the top grain. Even so, in all studied cases the sliding simulations reach a steady state in which the top grain slides with respect to the lower grain, with both the grain sizes as well as the extent of the disordered regions attaining stationary values.

Figure 2.3 displays the evolution of the shear stress in the system, comparing results for two temperatures and various sliding velocities along the y axis. In particular, to assess the influence of the nature of the GB layer on the sliding process, we consider temperatures of 150 K and 250 K, respectively. Whereas in the latter case the GB interface displays liquid-like characteristics, [17] in the former it does not. The resulting σ_{yz} shear-stress values are plotted as a function of the shear strain, defined as $\gamma \equiv v\,t/L_z$, where v is the imposed sliding velocity, t is time and L_z is the distance between the outermost layers along the z axis.

For both temperatures the stress response is manifestly non-monotonic, resembling the typical viscoelastic behavior observed for a number of polymeric and/or glassy systems subjected to shear deformation, [111, 112, 113, 114, 115, 116, 117, 118, 119] including bulk supercooled liquid water. [120] The initial response is elastic in nature, with σ_{yz} increasing linearly as a function of the strain γ and the slope being independent of the sliding velocity (see insets in Fig. 2.3a) and b)). In the elastic regime the displacement of the top layer is small, $\lesssim 3$ Å , giving rise to elastic shear deformations of the crystal grains, but without sliding activity at the interface. Subsequently, viscous relaxation processes set in, first
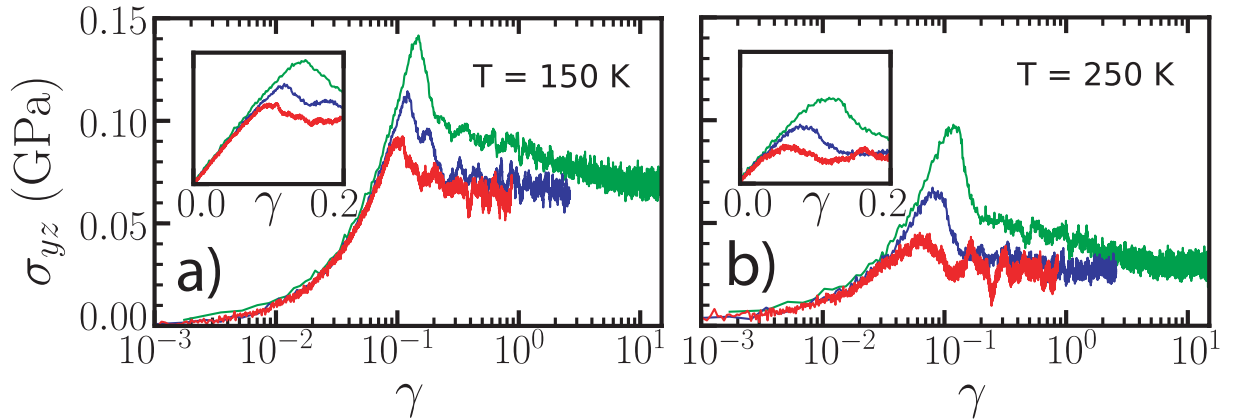
Figure 2.3: Shear stress σ_{yz} as a function of the strain γ for T = 150 K (a), and T = 250 K (b) for sliding processes in the y direction. Different colors correspond to different sliding velocities: 10 (green), 1 (blue), and 0.1 (red) m/s. Insets detail the elastic-response regimes, employing a linear scale for γ.
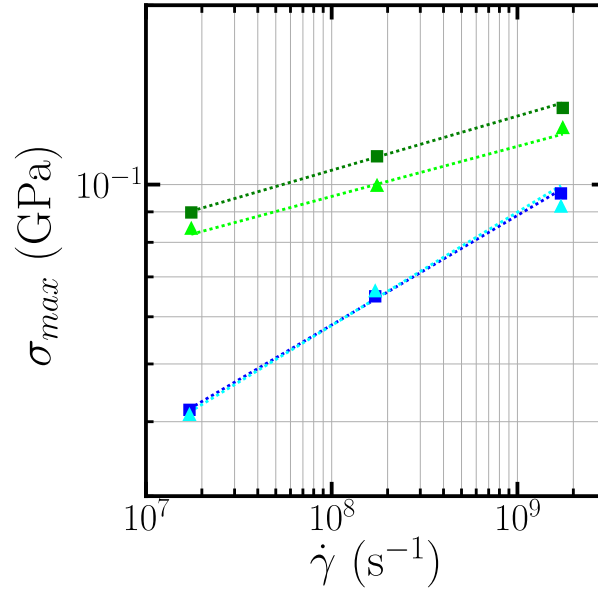
Figure 2.4: Yield stress as a function of sliding velocity represented in terms of the shear rate (see main text). Green and blue data points correspond to results for 150 and 250 K, respectively. Triangles and squares represent data for sliding in the x and y directions respectively. Dashed lines serve as guides to the eye.

reducing the elastic increase of the shear stress to reach a maximum, $\sigma_{yz}^{\mathrm{max}}$, also referred to as the yield stress at which rheological response commences, followed by a final decay to a steady-state plateau value, σ_{yz}^{∞}, that corresponds to a stationary viscous sliding regime. The yield and stationary-state stresses can be interpreted in terms of effective static and dynamic frictional agents, respectively. Similar to what is seen in viscoelastic systems, both $\sigma_{yz}^{\mathrm{max}}$ and σ_{yz}^{∞} decrease as the imposed sliding velocity is reduced, allowing stress relaxation mechanisms to be active during longer periods of time for a given displacement of the top layer.

The role of the character of the GB interface becomes apparent when considering the temperature dependence as well as anisotropy of the rheological onset. Figure 2.4 displays the yield stress as a function of the sliding velocity, represented in terms of the shear rate $\dot{\gamma} \equiv v/L_z$, for sliding along the x and y directions at both considered temperatures. The results indicate that the presence of a liquid-like layer in the interface at 250 K eases GB sliding. First, it facilitates the onset of sliding, with the yield stress being systematically lower compared to the case of 150 K, an effect that becomes more pronounced as the imposed velocity is reduced and the liquid-like interface has more time to relax under the imposed shear. Also, it causes the onset of sliding to be isotropic, with the yield-stress values being independent of the direction of sliding. In contrast, in the
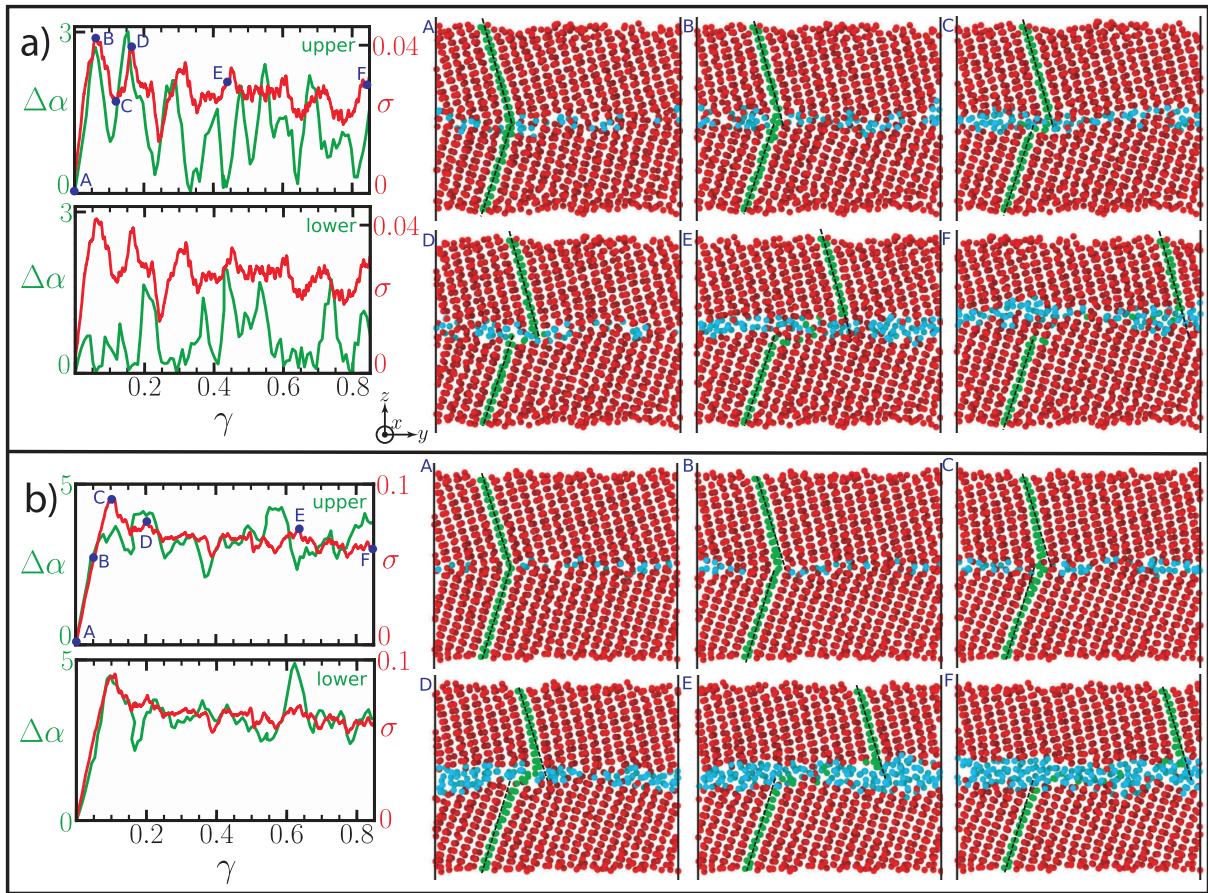
Figure 2.5: Correlation between shear stress evolution and molecular configurations at a sliding velocity of 0.1 m/s in the y-direction at 250 K (a) and 150 K (b). Capital letters in the molecular snapshots on the right correspond to stress/strain values marked in the upper graphs on the left. Red spheres correspond to molecules in a crystalline environment, oxygens in non-crystalline surroundings are shown in light blue. Oxygens shown in green are reference rows used to track deformation and relative translation of grains. Dashed lines mark inclination of reference rows before the sliding process. Upper and lower graphs on the left display the shear stress as a function of the shear strain (red curves, right vertical axis, in units of GPa) and the angular deviation $\Delta\alpha$ of the reference rows with respect to their initial inclination (green curves, left vertical axis, in degrees) for the upper and lower grains, respectively.

absence of a liquid-like layer at 150 K, the onset of sliding is evidently anisotropic, being most easily initiated along the x axis, which, for this particular GB, coincides with the rotation axis defining the misorientation of both grains.

After the yield stress has been reached and the relative displacement of the grains initiates, the evolution of the shear stress along the sliding process is irregular, as shown in Fig. 2.5. Figure 2.5 a) and b) correlate the shear stress evolution with the corresponding molecular configurations for the sliding velocity of 0.1 m/s at 250 and 150 K, respectively. The deformation and displacement of the grains is traced by monitoring the orientations
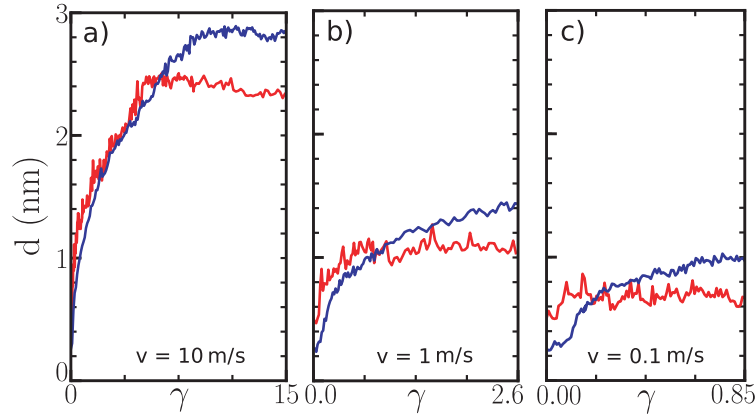
Figure 2.6: Thickness of disordered GB region during sliding simulation at 250 K (red lines) and 150 K (blue lines) for sliding velocities of 10 (a), 1 (b) and 0.1 (c) m/s.

and positions of the reference atomic rows shown in green. Initially, before the sliding process, these two atomic rows connect at the GB plane and their inclinations are indicated by the dashed lines. As the motion of the upper grain progresses, both the relative positions as well as the angles of reference rows vary with respect to the initial situation. The two graphs in Fig. 2.5a) and b) show the evolution of the shear stress together with the variation of the angle of the atomic rows in the upper and lower grain with respect to the initial inclination for 250 K and 150 K, respectively. At 250 K, the stress evolution is accompanied by a stick-slip-like succession of increasing elastic deformation, as signaled by a deviation of the atomic-row inclination $\Delta\alpha \simeq 1 - 3°$ from its initial value, followed by a sudden and complete relaxation in which the inclination returns to its undeformed state. At 150 K, on the other hand, the deviation of the row inclination is significantly larger and maintains an average value of $\Delta\alpha \simeq 3 - 4°$, without relaxing to its initial value. For sliding in the x direction a similar picture is observed, as can be seen in Fig. S1 of the Supporting Information.

A further difference between the two temperatures is the extent of the GB region. To estimate the thickness of the disordered region for a given configuration we determine the volume of the polyhedral-surface mesh (see Fig. 2.2) for the oxygens classified as non-crystalline by the IDS order parameter and divide it by the area of the xy plane of the cell. The results are shown in Fig. 2.6 which displays the layer thickness during the sliding process for velocities of 10, 1 and 0.1 m/s. In all cases the thickness of the GB region increases significantly for 150 K, meaning that the sliding process gives rise to substantial amorphization, an effect that is more pronounced as the sliding velocity is increased. For 250 K the increase of the GB layer is considerably smaller, and essentially absent
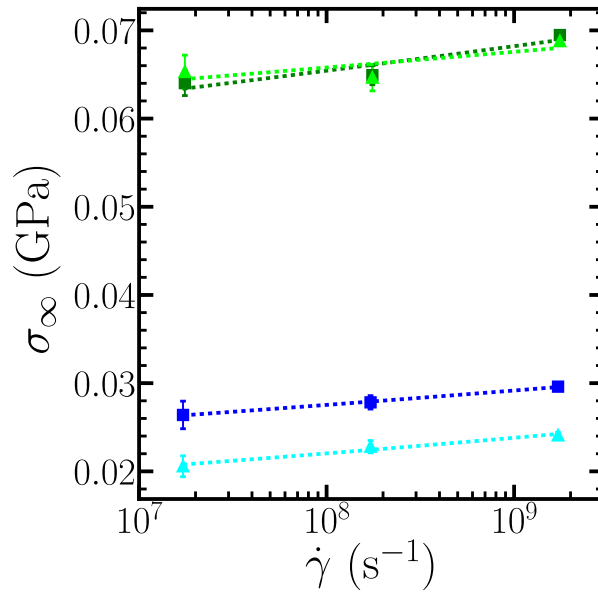
Figure 2.7: Steady-state shear stress required to maintain sliding process as a function of the imposed shear rate $\dot{\gamma}$. Green and blue data points correspond to results for 150 and 250 K, respectively. Triangles and squares represent data for sliding in the x and y directions respectively. Dashed lines serve as guides to the eye.

altogether for the lowest sliding velocity. This indicates that, when displacement speeds are relatively small, the disordered GB layer at 250 K effectively acts as a boundary lubricant [121] in the grain sliding process. This is also reflected in the values of the steady-state shear stresses required to maintain the sliding process, as shown in Fig. 2.7. In contrast to the yield stress, which can be interpreted in terms of a static frictional force, with the effective frictional force for 250 K being more than two times smaller compared to the case of 150 K. It should also be noted that, in contrast to the yield stress, there is a moderate anisotropy in the steady-state stress at 250 K. This is due to the fact that the thickness of the GB layer for sliding in the x-direction is slightly larger compared to sliding in the y-direction (see Figure S2 in the Supporting Information), further facilitating sliding. At 150 K, even though there is significant GB amorphization, there is no efficient shear stress release due to lower molecular mobility.

In addition to the extent of the GB region, there are also notable differences between the two temperatures as far the structural characteristics are concerned. This is shown in Fig. 2.8, which depicts the fraction of molecules in non-crystalline surroundings as a function of the z position in the cell. These fractions are computed by dividing the cell into slabs with a z-direction width of 2.72 Å and computing the proportion of non-crystalline oxygens as classified by the IDS order parameter. Comparing both
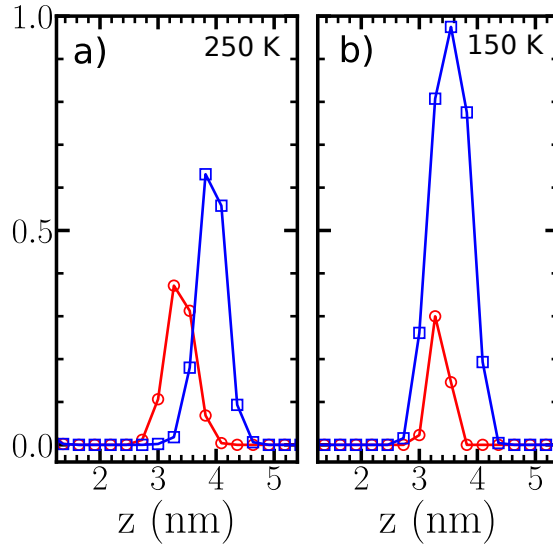
Figure 2.8: Fraction of molecules in a non-crystalline profile along the z direction of the simulation cell at 250 K (a) and 150 K (b). Red lines correspond to initial profiles corresponding to the snaphots A in Fig. 2.5 a) and b). Blue lines show result after shearing over a distance of 5 nm, corresponding to molecular snaphots F in Fig. 2.5 a) and b).

temperatures, for 250 K the initial fraction profile is wider and has a larger maximum compared to 150 K, which is consistent with the visualizations of snapshots A in Fig. 2.5 a) and b), in which the GB region for the lower temperature is narrower and less disordered. After sliding over 5 nm, on the other hand, this scenario changes significantly. At 250 K, the thickness of the GB layer at 250 K remains essentially the same, as discussed above, although the shift in the peak signals that the GB layer has migrated upward, as can be seen in snapshot F of Fig. 2.5a). The degree of disorder upon sliding increases only moderately from $\sim 40\%$ to $\sim 65\%$. For 150 K, on the other hand, not only does the width of the GB region increase substantially, the fraction of non-crystalline molecules attains almost 100% in the steady state. This indicates that, even in the presence of a substantial portion of molecules in a crystalline environment at 250 K, the GB layer still substantially reduces the sliding friction when compared to the entirely disordered interface at 150 K.

This is also consistent with the difference between the molecular mobilities for both temperatures, as shown in Fig. 2.9. It plots the distributions of the molecular displacements in the x, y and z directions with respect to their initial positions of the molecules labeled as non-crystalline at the end of the sliding process over 5 nm along the y direction. Fig. 2.9 c) shows that this distribution for the y direction is very wide, indicating that the displacements are far from homogeneous, with some particles moving along with the imposed sliding process, while others hardly move at all. Comparing the
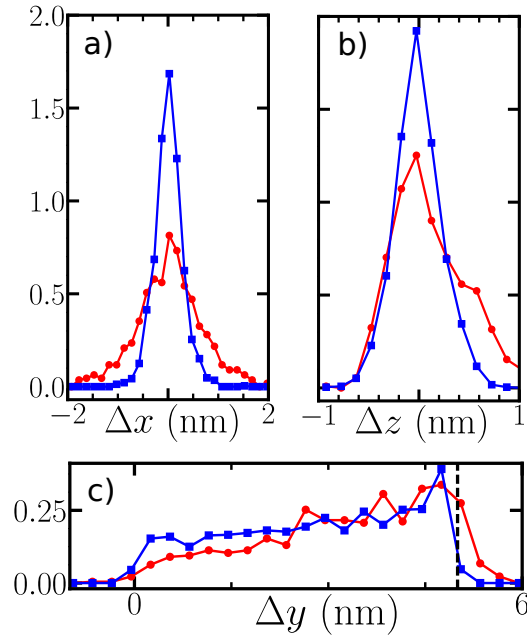
Figure 2.9: Normalized distributions of the displacement components (a) Δx, (b) Δz, and (c) Δy, with respect to the initial configuration, of the oxygens atoms classified as disordered by the IDS parameter after 50 ns at a sliding velocity of 0.1 m/s in the y direction. Colors correspond to different temperatures: 250 K (red), and 150 K (blue). The dashed black line indicates the total displacement of the upper grain with respect to the lower grain

distributions for both temperatures, at 250 K the molecules are seen to move more easily, with some of them moving across distances in the y direction that are larger than the 5-nm displacement of the upper constrained layer. This is also seen for the displacements in the x component, the in-plane direction perpendicular to that of the sliding. While for 150 K these displacements remain well within 5 Å, for 250 K they can be three to four times as large. In the z-direction, on the other hand, the displacement distributions are quite narrow for both temperatures, reflecting the 2D confinement provided by both crystal grains. These results are consistent with a picture in which, for 150 K, the molecular mobility in the amorphous GB region is relatively low, giving rise to a comparatively large sliding friction. For 250 K, on the other hand, the in-plane mobility of the molecules in the liquid-like layer is enhanced, leading to a reduced friction.

2.4   Conclusions

In summary, we have carried out molecular dynamics simulations to investigate the process of GB sliding in proton-disordered hexagonal ice I$_h$ as described by the explicit-proton TIP4P/Ice model. In particular, we have considered the $\Sigma35$ symmetric tilt boundary, which has been observed experimentally in polycrystalline samples. In all cases the shear stress response during the process resembles that of viscoelastic substances, with an initial linear elastic regime followed by a maximum yield stress and a final relaxation toward a steady-state value that corresponds to a stationary sliding state. To assess the influence of the molecular structure and dynamics of the GB region we consider different sliding velocities and directions, as well as various temperatures. With regard to the latter, we contrast two situations: one in which the GB interface features the presence of a liquid-like layer at 250 K and another in which there is not, at 150 K. We find that the liquid-like layer facilitates GB sliding at 250 K, acting as a boundary lubricant. Both the yield stress as well as the steady-state stress required to maintain sliding, which can be interpreted in terms of effective static and dynamic frictional agents, respectively, are significantly lower compared to the case at 150 K. While at 150 K the GB region undergoes large-scale amorphization in the frictional process, the thickness of the liquid-like layer at 250 K only increases moderately, reflecting its effectiveness in facilitating the sliding process. The present results provide valuable information regarding the viscous relaxation processes and the role of the disordered GB layer in the frictional behavior at the nanoscale during GB sliding in ice I$_h$. Even though these simulations are performed with high shear rates compared to the timescale of ice deformation processes in nature, for smaller shear rates we would expect the same viscoelastic behavior, with the linear elastic region independent on the shear rate, and different values for the yield and the steady-state stress.

Chapter 3

Effect of sodium chloride on internal quasi-liquid layers in ice I$_h$

This chapter was reproduced from [I. de Almeida Ribeiro, R. Gomes de Aguiar Veiga, and M. de Koning, J. Phys. Chem. C 125(33), 18526-18535 (2021)]. Copyright 2021 by American Chemical Society.

3.1   Introduction

Sodium and chloride ions are among the most common solvated impurities in liquid water. In sea water, for example, sodium chloride is present in molarities of the order of ~0.5 and there has been a significant interest in its role on the properties of liquid water. [122, 123, 124, 125, 126, 127] Similarly, the influence of sodium chloride on solid phases of water, in particular the hexagonal proton-disordered ice I$_h$, [20] has also attracted substantial attention. [22, 128, 129, 130] For instance, in addition to atmospheric processes involving the nucleation of ice crystals, [131, 132] sodium chloride is known to affect the mechanical properties of large ice masses on Earth, including sea ice as well as glaciers. [133, 134]

Although sodium chloride dissolves easily in the liquid form of water, it has an extremely low solubility in ice I$_h$. As a result, when saline water is frozen to a temperature between the freezing point and the eutectic temperature, the system will consist of

almost pure polycrystalline ice in equilibrium with a concentrated aqueous salt solution, also known as brine. [20] When the temperature falls below the eutectic temperature of $\sim 252\,K$, on the other hand, the eutectic reaction results in the transformation of brine into ice and a secondary crystalline phase known as sodium chloride dihydrate, NaCl·2H$_2$O. [135] In either case, the negligible solubility of sodium chloride in ice I$_h$ gives rise to salt concentrations in regions of the ice microstructure in which segregation is favored.

Grain boundaries (GBs), the internal interfaces that separate adjacent grains with different crystallographic orientations in polycrystals, [86, 87] are natural regions of such enhanced segregation, which, due to their larger free volume and associated enhanced disorder, are known to act as sinks for impurities that are insoluble in the crystalline phase. Indeed, for the case of ice I$_h$, there is ample experimental evidence [136, 137, 138, 139, 140, 141, 142] that GBs represent preferred locations for insoluble impurities such as sodium and chloride ions, contributing to a network of interconnected brine channels. Moreover, both optical scattering experiments [12] as well as nuclear magnetic resonance spectroscopy (NMR) measurements [21] indicate that, similar to the case for pristine ice samples, [11, 12, 13, 14, 15, 16, 17, 143] these regions are liquid-like. In fact, the NMR experiments suggest that this liquid-like behavior of these so-called quasi-brine layers (QBL) [21] persist even at ~ 20 K below the eutectic point for which, in bulk equilibrium, all NaCl would have precipitated as crystalline sodium chloride dihydrate. [21]

Despite the compelling evidence for the existence of internal liquid-like or quasi-liquid layers (QLL), very little is known about the structure and dynamics of these regions. For pristine ice, atomistic simulations indicate that the mobility of water molecules in such layers is significantly lower than in bulk supercooled liquid water at the same temperature, displaying sub-diffusive behavior on time scales of ~ 100 ns. [16, 17] This enhanced sluggishness has been linked to the confined nature of these quasi-liquid regions, with the restraining presence of adjacent crystal grains restricting molecular motion. [16, 23, 144, 145] However, whether or not this sluggishness is affected when sodium chloride is dissolved is an open question and it is directly related to, for instance, mass transport along the GB regions and mechanical deformation mechanisms based on grain sliding processes.

In this light, the purpose of the present paper is to investigate the structural and dynamical properties of GB regions in the presence of dissolved sodium chloride at conditions substantially below the melting point of pristine ice. In particular, we consider the $\Sigma 35$ symmetric tilt boundary, which, in addition to having been observed

experimentally, has been subject of previous atomistic simulation studies focusing on diffusion and sliding dynamics in pristine ice I$_h$, at a temperature of 20 K below the melting temperature. [143] To this end we use molecular dynamics (MD) simulations based on the rigid, nonpolarizable TIP4P/2005 water model [62, 146] in conjunction with the "Madrid-2019" force field for the description of the interactions between the sodium and chloride ions, and the water molecules. [126, 147]

3.2   Computational details

3.2.1   Model

To describe the interactions between the water molecules and the ions we employ the Madrid-2019 force field [126, 147], which is a non-polarizable description developed specifically for the rigid TIP4P/2005 water model. [62, 146] It is based on the method of scaled charges [148] and is calibrated using solution densities, radial distribution functions, hydration numbers, and densities related to those of the melt and of the solid. [126] It has been used to study ice growth and the ice/liquid interface doped with NaCl [129], as well as the physical properties of seawater. [149]

3.2.2   Computational cells

All simulations are based on computational cells similar to that employed in previous work, [16, 143] implementing a bicrystal set-up in which two grains are separated by a $\Sigma 35$ GB region as shown in Fig. 3.1. The cells are periodic in all three directions and measure approximately 7.6 nm $\times$ 7.5 nm $\times$ 15.4 nm in x, y and z, respectively. The z-direction includes a vacuum layer of ~ 10 nm such that the system contains only one GB region and two free surfaces. In addition to allowing one to focus on single GB region, this arrangement permits implementing sliding simulations in which the top and bottom halves of the bicrystal can be displaced relative to each other. [143] The cells contain 10800 water molecules and varying numbers of ions depending on the considered sodium-chloride concentrations. Specifically, in addition to pure ice I$_h$, we consider the cases in which the global salinity, defined as the mass proportion of NaCl to H$_2$O in the entire cell, is 1.5% (50 pairs of ions in the cell) and 3.5% (117 pairs of ions in the cell),

with the latter being close to the average salinity of the oceans. [19] Given the insolubility of sodium chloride in ice I$_h$ all the ions are placed directly within the GB region, using randomly selected positions.

For reference purposes we have also carried out a number of simulations for bulk liquid sodium-chloride solutions, which are based on cubic periodic cells containing 2000 water molecules and varying numbers of sodium and chloride ions depending on the concentration of interest.

3.2.3   Equilibration

To obtain equilibrated samples after randomly inserting sodium and chloride ions into the GB region we adopt the following procedure. First, to eliminate possible overlaps due to the initial random placement of the ions, we perform an energy minimization while keeping fixed the positions and orientations of the water molecules. The minimization and all further calculations have been carried out using the `LAMMPS` MD package,[57] handling long-range electrostatic interactions using the particle-particle particle-mesh (PPPM) scheme [56] and constraining intramolecular bond lengths and angles are held fixed using the SHAKE algorithm. [64] Subsequently, to allow relaxation of the cell dimensions, we carry out an unconstrained MD simulation over a time interval of 10 ns at zero external pressure and the target temperature of $T = 228K$, which is ~20 K below the melting point of the TIP4P/2005 water model. [150, 151, 152, 153] Pressure and temperature are controlled using a Parrinello-Rahman-type barostat [55, 107, 108] allowing only the x and y dimensions of the cell to vary, and a Langevin thermostat, [53] with the damping parameters of 2 ps and 0.2 ps, respectively. The corresponding equations of motion are integrated using a time step of 2 fs. Next, given the slow translational and rotational motion at 228 K, we further equilibrate the ionic distribution by selecting a thin layer around the center of the GB region that encloses all sodium and chloride ions and raising the temperature of all particles inside to $350\,K$ while keeping fixed the water molecules outside this layer. After evolving at $350\,K$ for 10 ns, the layer is cooled back to the target temperature of $228\,K$ at a rate of $60\,K/\text{ns}$. Lastly, to allow a final relaxation of the simulation cell, the entire system is released and allowed to evolve at zero pressure and $T = 228\,K$ during 10 ns. As shown by the total-energy evolution in Fig. 3.1c), this is sufficiently long for the system to equilibrate. By measuring the volume of the equilibrated GB regions as detailed below, the global concentrations of 1.5% and

3.5% lead to effective local salinities of ~ 22 and $\sim 32\%$ in the GB regions. These values correspond to highly concentrated solutions of sodium chloride that can be formed during brine rejection from freezing salt solutions. [22, 128, 129] In the remainder of the paper the GB systems with local sodium chloride concentrations of ~ 22 and $\sim 32\%$ will also be referred to as cases of intermediate and high salinity, respectively. All averaged quantities reported below are obtained from 500 configurations extracted from 100 ns long constant volume MD runs initiated from the equilibrated simulation cells.

3.2.4 GB sliding simulations

To assess the role of the sodium and chloride ions in GB sliding processes, we employ the same simulation setup as used recently for the case of pristine ice I$_h$. [143] Based on the equilibrated cell we define two subsets of molecules that are located in slabs with a thickness $\Delta z \simeq 7$ Å at the top and bottom free-surface regions of cells. The sliding process is then implemented by rigidly moving the molecules in the top slab with a constant velocity $v = 0.1$ m/s parallel to the GB region, while fixing those in the bottom slab. Thermostatting is applied only to the molecules outside these two constrained slabs. The equations of motion for the sliding simulations are integrated using a time step of 1 fs.

3.3 Results and discussion

Figure 3.1a) and b) displays snapshots of the computational cell before and after equilibration for the intermediate salinity. To facilitate visualization, only the oxygens and the ions are shown. To quantify the degree of disorder in the ice I$_h$ structure we compute the `Identify-diamond-structure` (IDS) order parameter [99] as implemented in the Open Visualization Tool (`Ovito`) package [100] for the set of oxygen positions. IDS is a modification of the common-neighbor-analysis approach that includes up to second neighbors, allowing one to distinguish between cubic and hexagonal diamond structures, as well as identify their first and second neighbors. It has shown to be useful in the analysis of ice-based systems, where it correctly recognizes crystallinity even in symmetry-breaking situations at a free surface. [104] The oxygens shown in cyan are classified as being part of a crystalline environment, either in a fully hexagonal-diamond (HD) surrounding, or
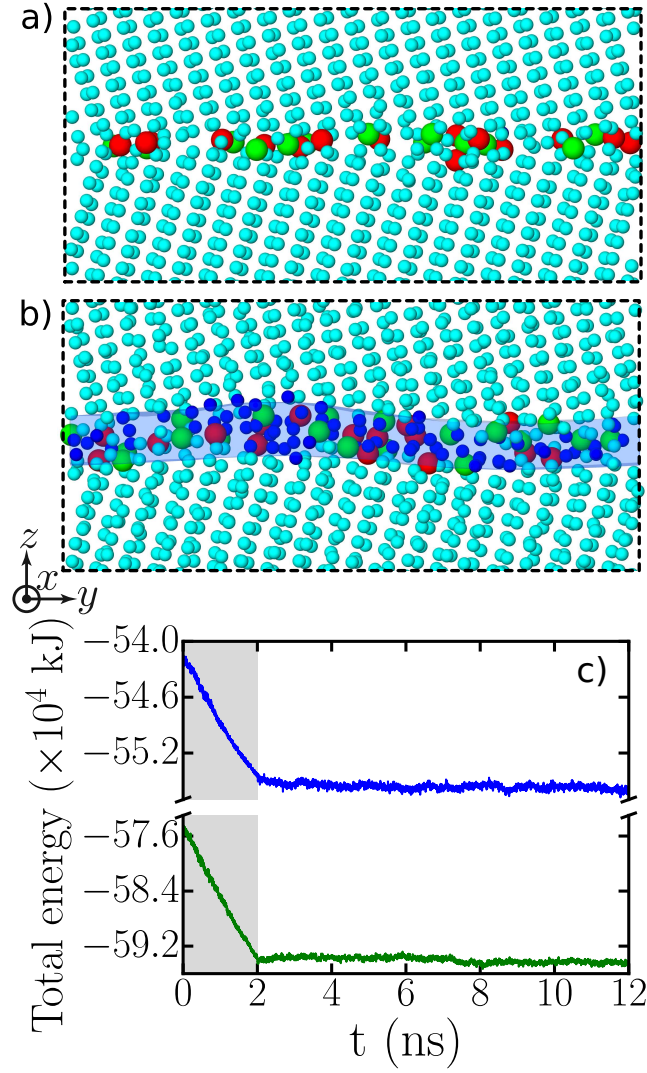
Figure 3.1: Structure of the bi-crystal ice I$_h$ cell containing a $\Sigma 35$ symmetric tilt grain boundary for the intermediate salinity, showing only the ions and the oxygens. Na$^+$ and Cl$^-$ ions are displayed in red and green, respectively. Oxygens painted cyan and blue are classified as being in a crystalline environment and non-crystalline surroundings, respectively, as determined using the IDS order parameter (see text). (a) Initial configuration after random insertion of sodium and chloride ions in GB region. (b) Snapshot of system after equilibration at $T = 228\,K$. Light blue-shaded area depicts the extent of non-crystalline region as determined using the polyhedral surface-mesh algorithm. [110] (c) Total energy of the computational cell during the equilibration process for the intermediate (blue) and high (green) salinities.

as a HD first or second neighbor. The oxygens painted in blue, on the other hand, are assigned as belonging to non-crystalline, disordered surroundings.

Comparing the configurations before and after the equilibration at 228 K, the latter has developed a disordered GB region of appreciable thickness. To quantify this disorder profile and assess its dependence on the salinity, we determine the average fraction of non-
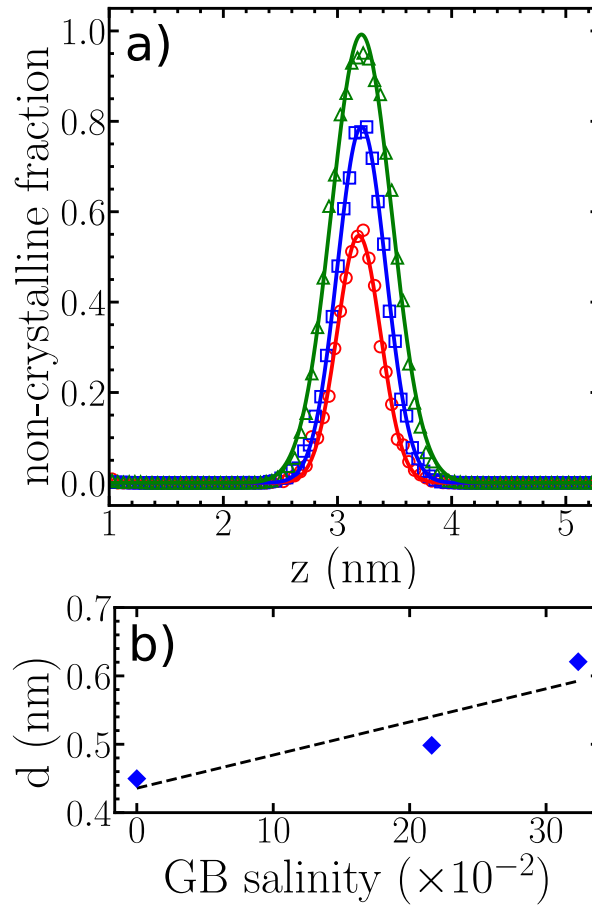
Figure 3.2: a) Fraction of non-crystalline water molecules as a function of the z direction in absence of impurities (circles), and for the intermediate (squares) and high (triangles) salinities. Lines correspond to Gaussian fits to atomistic data. b) Average GB thickness d, estimated from Gaussian FWHM values of non-crystalline-oxygen profiles, as a function of the local salinity at the GB. Statistical uncertainties from Gaussian fits are smaller than symbol size. Dashed line serves as a guide to the eye.

crystalline oxygens as a function of the z-coordinate, with the results shown in Fig. 3.2 a). For pristine ice I$_h$ the degree of disorder in the center of the GB region, at the peak in its profile, is still only ∼50 %, meaning that a considerable degree of crystallinity persists. As sodium chloride is added, however, the disorder increases considerably, as reflected by the greater peak height as the ionic concentration becomes larger. Moreover, the inclusion of sodium chloride also leads to a broadening of the profile, signaling an increase of the extent of the GB region. To quantify the evolution of the GB thickness with the salinity we fit the non-crystalline-oxygen profiles to Gaussian functions and define the GB thickness d as their full-width-at-half-maximum (FWHM) values, as shown in Fig. 3.2 b). The value of d increases with the salinity, which is consistent with experimental optical scattering data for polycrystalline ice samples, [12] which report an approximately linearly trend.

While the non-crystalline water profiles of Fig. 3.2 quantify average properties such as the overall behavior of the non-crystallinity profiles and the average GB thickness, they do not provide insight into the local structural characteristics of the GB region. To obtain such information we employ the polyhedral surface mesh (PSM) tool as implemented in the `Ovito` package. It creates a geometric representation of the inner and outer surfaces of a three-dimensional area that encloses a specified group of atoms/molecules, providing information about the surface area, volume and possible porosity of the region. [110] Here, we construct the surface mesh for the region enclosing the water molecules classified as non-crystalline. Figure 3.3 a) shows a typical xy projection of the positions of the non-crystalline oxygens (blue circles) and the generated surface mesh (light-blue-shaded areas) for the pristine ice I$_h$ case. The picture clearly shows the disordered GB region to be porous in the absence of ions, with the white areas representing holes in the surface mesh. These signal the absence of non-crystalline water molecules in those regions and are responsible for the fact that the peak values of the profiles in Fig. 3.2 are below 1. Indeed, the water molecules located in these holes belong to crystalline environments, as shown by the bond network depicted in cyan, and these pockets form crystalline bridges between the two grains. Nevertheless, these domains are dynamic in nature, constantly being dissolved and formed due to the incessant melting and recrystallization at the GBs. Similar structures have also been found for ice premelting at low temperature.[71] The presence of sodium chloride in the GB region, however, progressively reduces the number and size of these crystalline pockets with the ionic concentration, as shown in Figs. 3.3 b) and c). At the high salinity the GB region is almost entirely covered by the disordered layer, with the two grains becoming almost completely disconnected. Such ionic effects have also been observed at the external ice-air interface for the case of lithium chloride. [154]

Aside from the substantial increase of the GB thickness, the presence of sodium chloride also leads to notable differences in the molecular structure. Fig. 3.4 shows the ionic-concentration dependence of the radial distribution functions (RDF) for the water molecules in the GB region which have been computed by considering the water molecules located within slabs with a thickness of 5 Å in the z direction around the center of the GB regions. The results for the bulk solutions were obtained by analyzing data for slabs of the same thickness using the 2000-molecule cell, with 130 and 200 NaCl ion pairs for the intermediate and high salinities, respectively. Contrasting the GB results for the different salinities, the RDFs show that the presence of sodium chloride progressively diminishes the degree of structure of the water in the GB region, with the peak heights reducing as the salinity is increased. For the high salinity, for instance, only the first peak in the
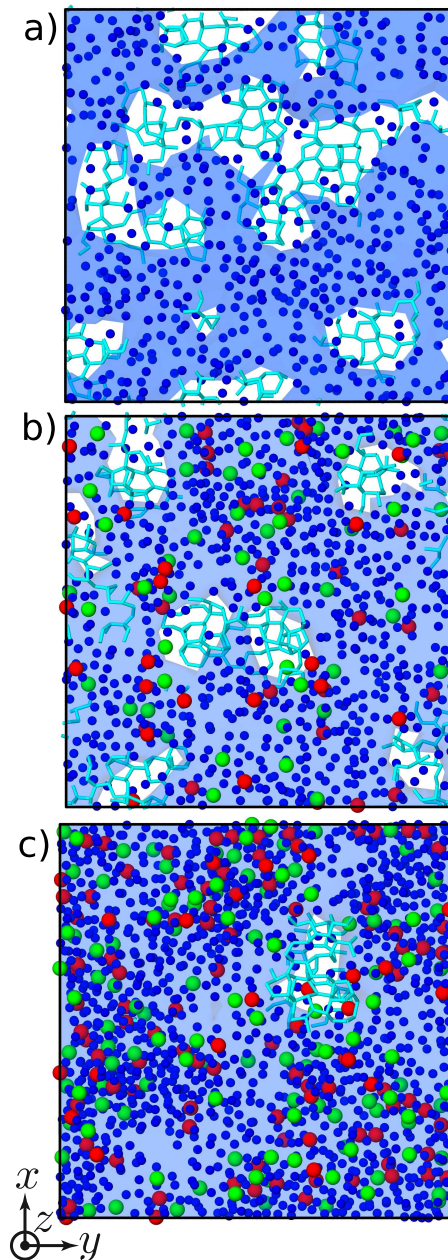
Figure 3.3: Snapshots showing a top view (xy projection) of GB plane of an equilibrated configuration for (a) pristine ice, (b) the intermediate salinity and (c) high salinity. Oxygens classified as disordered within the GB are shown as the blue circles, whereas the sodium and chloride ions are depicted in red and green, respectively. Blue-shaded areas represents surface-mesh region enclosing the disordered oxygens. The white areas are holes in the surface mesh, indicating the porosity of the region. Cyan bonds connect the oxygens classified as crystalline.

RDF for oxygen-oxygen pairs remains well defined. It is illuminating to compare the GB RDFs to the corresponding bulk sodium chloride solutions, i.e., in absence of crystal grains, for which such structure-reducing effects have also been registered [123, 155]. The bulk solution results, shown as the black dashed lines in Fig. 3.4, were obtained
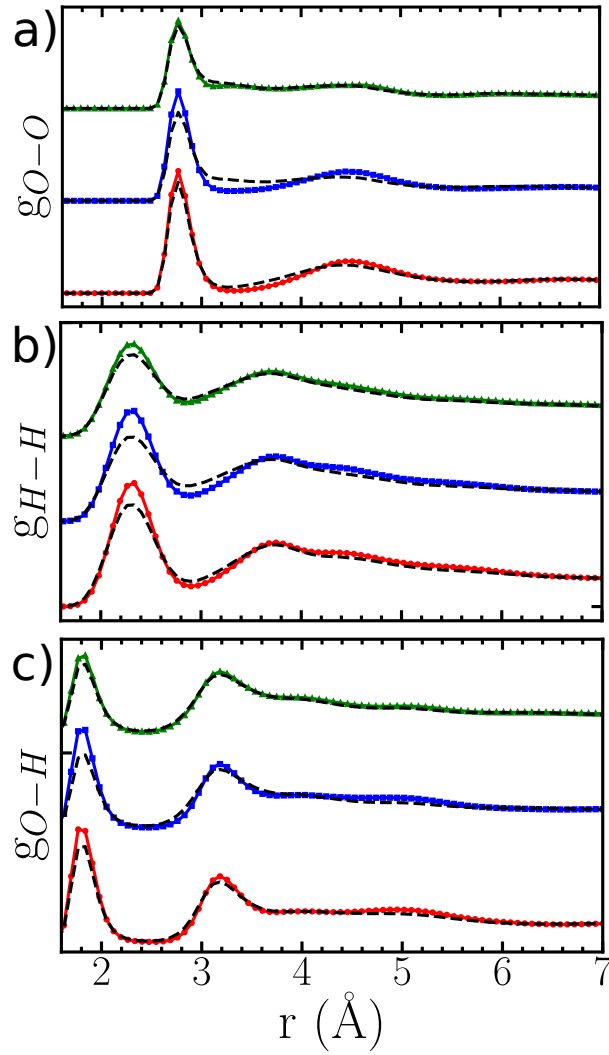
Figure 3.4: Radial distribution functions for the water molecules in the GB region with a), b) and c) showing the results for the oxygen-oxygen, hydrogen-hydrogen and oxygen-hydrogen correlations, respectively. Red, blue and green lines correspond results for the pristine sample, the intermediate salinity and high salinity, respectively. RDFs for different concentrations have been shifted vertically for clarity. Dashed lines represent results for corresponding bulk liquids at same conditions of temperature, pressure and salinity.

using computational cells containing 2000 water molecules and 130 and 200 NaCl pairs for the intermediate and high salinities, respectively, and the RDFs were obtained by analyzing data for slabs of the same thickness of 5 Å. Whereas for pristine water and the intermediate salinity the RDFs in the GB regions are more structured compared to those in the corresponding bulk liquids, for the high salinity this effect almost entirely disappeared, and the water-molecule structure in the GB layer has become very close to that of the bulk briny solution. This indicates that the structure reduction in the GB region is associated with the progressive dissolution of crystalline domains and the increasing thickness of the GB layer as the sodium chloride concentration is raised.

Fig. 3.5 shows the corresponding ion-water RDFs for both salinities. Overall, their structures are essentially equal in both environments, indicating that the ionic solvation structure is mostly the same in the GB region and the bulk solution. However, the correlation between the protons and the chlorine ions is an exception. Similar to the water RDFs in Fig. 3.4 the first peaks in the H-Cl RDFs in the GB regions are higher compared to those in the bulk solution. This enhanced structuring is related to the fact that, in contrast to sodium, chlorine ions are able to act as substitutional impurities at unoccupied lattice sites in defected ice structures, effectively serving as proton acceptors for surrounding water molecules. [129, 156] While absent in the bulk liquid solution, such crystalline substitutional sites are always present in the crystalline GB region, providing potential trapping sites for the chlorine ions. This is also consistent with the fact that the excess H-Cl structuring with respect to the bulk solution is smaller for the GB region with the high salinity, in which the thickness of the disordered, liquid-like region is larger.

Next, we turn to the dynamical properties of the briny GB regions. For this purpose, we first focus on the molecular diffusivities, monitoring the mean-squared displacement (MSD) of the water molecules that are initially within slabs with a thickness of 4 Å in the z direction centered around the disordered GB region. Given that the contribution perpendicular to the GB is restricted due to the enclosing crystal grains, we focus on the in-plane part of the MSD. Fig. 3.6 shows the time evolution of the molecular MSD for the pristine sample as well as for both salinities. In all cases, the GB region is manifestly liquid-like, even at a temperature 20 K below ice I$_h$'s melting point for which the NaCl-H$_2$O system is close to its eutectic transition. [157, 158] Nevertheless, the presence of sodium chloride significantly alters the mobility of the water molecules. First, the magnitude of the displacement over the considered time interval of 100 ns is almost an order of magnitude larger for the high salinity case as compared to the pristine ice sample. Furthermore, it also alters the character of the diffusion. For both pristine ice as well as at the medium salinity, the time-evolution of the MSD is manifestly sub-linear in nature, as indicated by the red and blue lines. This sub-diffusive behavior is related to the mixed crystalline/disordered character in the GB region shown in Fig. 3.3, which gives rise to intermittent molecular motion characterized by a sequence of waiting periods followed by rapid jumps and is consistent with previous findings of such non-Brownian diffusion in GBs in ice I$_h$. [16, 17] For the highest salinity, on the other hand, normal Brownian diffusion is restored on the entire time interval. This can be verified in the inset of Fig. 3.6 in which the MSDs for the intermediate and high salinities are plotted on a log-log scale. Whereas the slope of the intermediate salinity MSD is less than unity, ~ 0.75, meaning
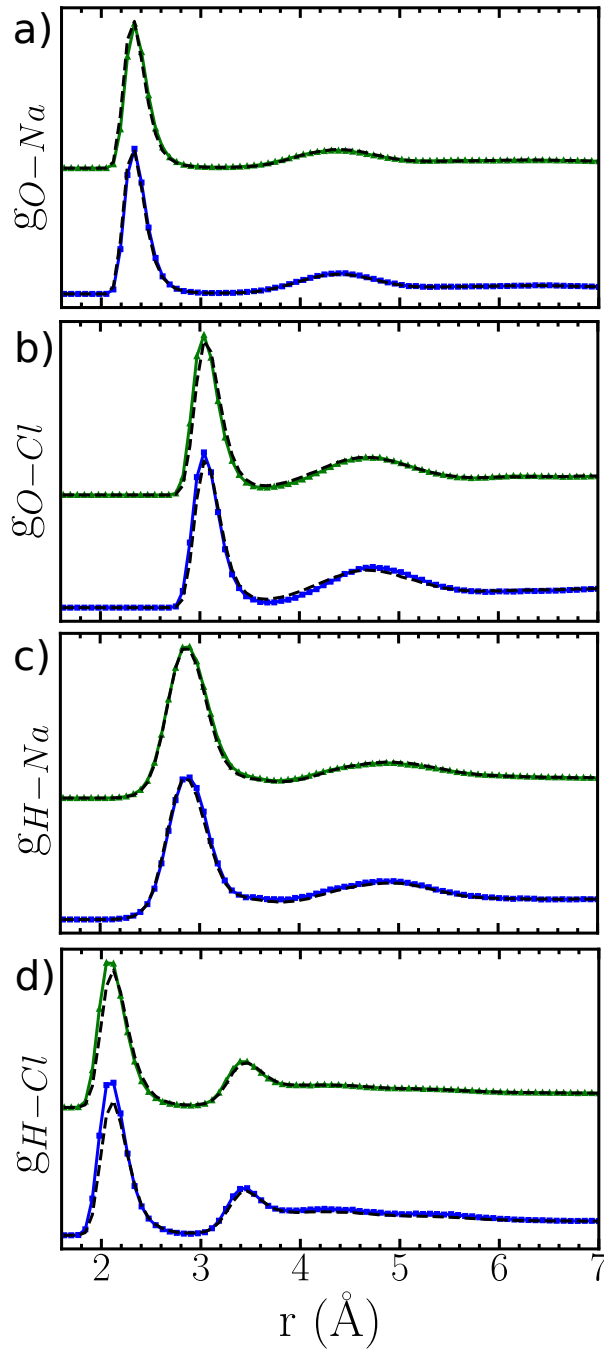
Figure 3.5: Water-ion radial distribution functions in the GB region, with a), b), c) and d) showing the results for the oxygen-sodium, oxygen-chloride, hydrogen-sodium and hydrogen-chloride correlations, respectively. Blue and green lines correspond results for the intermediate salinity and high salinity, respectively. RDFs for different concentrations have been shifted vertically for clarity. Dashed lines represent results for corresponding bulk liquid solutions at same conditions of temperature, pressure and salinity.

that it increases sub-diffusively according to $\sim t^{0.75}$, the high-salinity diffusion is normal, increasing linearly with time. Both the increase of the magnitude of the MSD as well as the restoration of Brownian diffusion as the sodium chloride concentration increases are
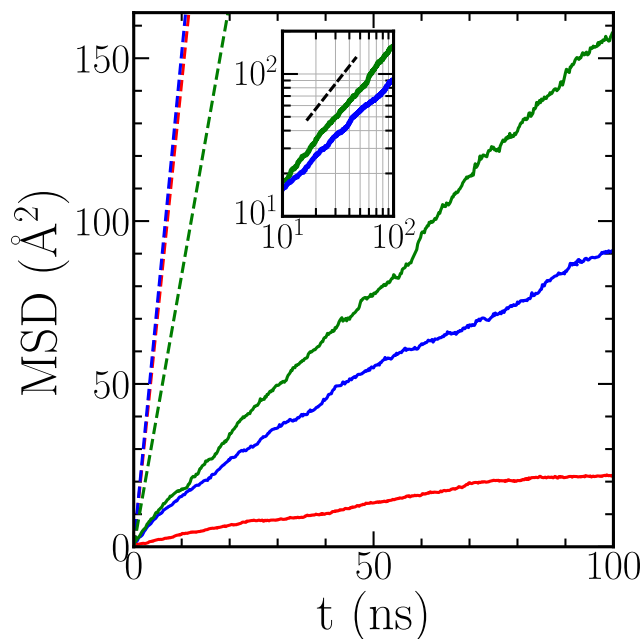
Figure 3.6: In-plane MSD as a function of time for the oxygen atoms. Results for the pristine sample and those with intermediate and high salinities are shown as red, blue and green lines respectively. Inset displays MSD evolution for intermediate and high salinities on a log-log scale. Black dashed line serves as reference with slope equal to unity, corresponding to Brownian diffusion. Colored dashed lines represent the corresponding bulk solutions at the same conditions of temperature, pressure and salinity.

related to the reduction of crystalline domains and the accompanying growth of the disordered layer. This shows that the ion-induced influence on the water mobility is specific to the particular structural properties of the confined GB regions. Indeed, this becomes even more apparent when comparing the results to the MSDs in the corresponding bulk solutions, as shown by the dashed lines in Fig. 3.6. The diffusivity in the latter is very much greater than in the GB regions, even though the structural characteristics as shown in the RDFs, in particular for the highest salinity, are quite similar. As such, the briny disordered region behaves as a quasi-liquid layer (QLL) in the sense that it is characterized by dynamical properties that are manifestly different from those of the corresponding bulk solution at the same conditions of temperature, pressure and sodium-chloride content. Even so, these internal QLLs behave quite differently from those at the free ice surface. [77, 84] Whereas the GB QLLs are sandwiched between two crystalline grains, the free-surface QLL is much less confined, bordering on the vapor phase at the top of the layer, giving rise to quite different mobilities. Indeed, in particular close to the QLL-vapor interface for pristine ice, diffusivities have found to be actually larger than those in the bulk liquid at the same temperature. [77, 84]
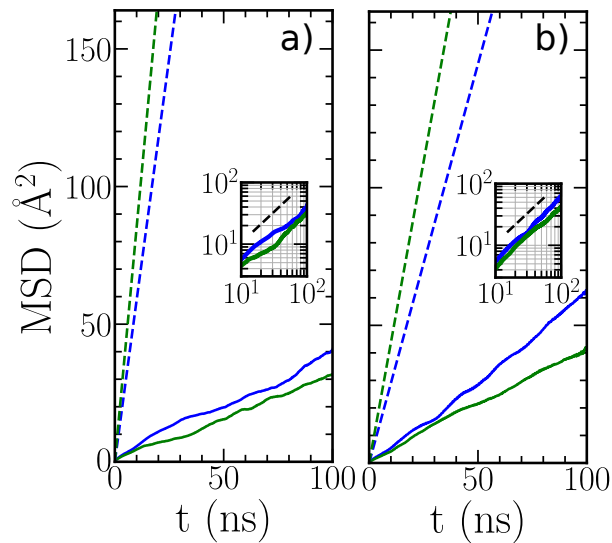
Figure 3.7: In-plane MSD as a function of time for the Na$^+$ (blue) and Cl$^-$ (green) ions with results for the a) intermediate and b) high salinities. Inset displays MSD evolution for intermediate and high salinities on a log-log scale. Black dashed line serves as reference with slope equal to unity, corresponding to Brownian diffusion. Colored dashed lines represent the corresponding bulk solutions at the same conditions of temperature, pressure and salinity.

Similar behavior is seen for the ionic diffusivities, as depicted in Fig. 3.7. In the GB regions they are much smaller as compared to the bulk solutions, by ratios that are similar to those observed in Fig. 3.6, indicating that the mobility of the ions is hampered by the sluggish water diffusivities. The log-log plots in the insets in Fig. 3.7 do not seem to signal sub-diffusive behavior in the ionic MSDs, although the statistics is limited due to the relatively low number of ions in the cell. A notable feature, however, concerns the relation between the sodium and chlorine diffusivities. While in the bulk solutions chlorine ions are found to diffuse faster than sodium, in agreement with previous reports [147], this relation is inverted in the GB region. This effect appears consistent with the enhanced H-Cl structuring shown in Fig. 3.5, in which chlorine ions are able to act as substitutional impurities at unoccupied lattice sites serving as temporary trapping sites and hampering diffusion.

Finally, we assess the effect of sodium chloride on the mechanical deformation mode mediated by GB sliding. The latter involves the process by which two crystal grains slide relative to each other along the GB interface, and constitutes one of the fundamental mechanisms contributing to the mechanical deformation of polycrystalline solids. Recent simulations [143] considered GB sliding in pristine ice I$_h$ for different temperatures, showing that the presence of an internal QLL facilitates both the onset
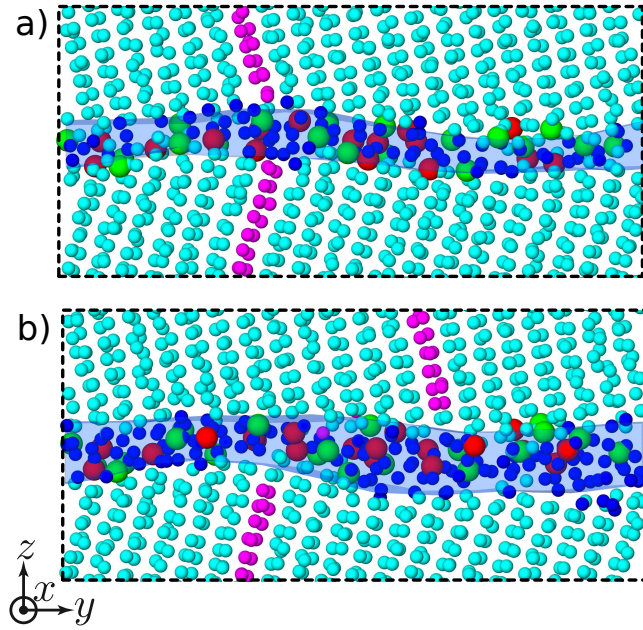
Figure 3.8: Typical evolution of molecular configuration for the intermediate salinity during sliding simulation in which the top grain slips past the lower grain in the y-direction at a velocity of 0.1 m/s. Na$^+$ and Cl$^-$ ions are displayed in red and green, respectively. Oxygens painted cyan and blue are classified as being in a crystalline environment and non-crystalline surroundings, respectively. Oxygens shown in magenta are reference rows used to track relative translation of grains. Light-blue-shaded area depicts the extent of non-crystalline region as determined using the PSM algorithm. (a) Snapshot of configuration before sliding. (b) Snapshot of system after shearing over a distance of 2.6 nm.

as well as reduces the steady-state sliding resistance as compared to low-temperature conditions in which the GB region is amorphous in nature. Here, we investigate the effect of the presence of sodium chloride in the briny GB regions on the sliding behavior.

Figure 3.8 shows typical snapshots of the molecular configuration for the intermediate salinity during a sliding process in which the upper grain slides past the lower one in the y-direction at a velocity of 0.1 m/s. Fig. 3.8 a) depicts the configuration immediately before the process, while Fig. 3.8 b) represents the situation after the upper grain has sheared over a distance of 2.6 nm and a steady-state sliding regime has been attained. As before, the blue-shaded areas represent the extent of the noncrystalline GB region as determined using the PSM algorithm. Aside from a small increase of the thickness of the GB layer for the displaced configurations, both snapshots are very similar, indicating a comparatively smooth sliding process.

To quantify the influence of the ions we monitor the evolution of the shear stress σ in the system during the sliding process, based on the standard virial expressions. [109]
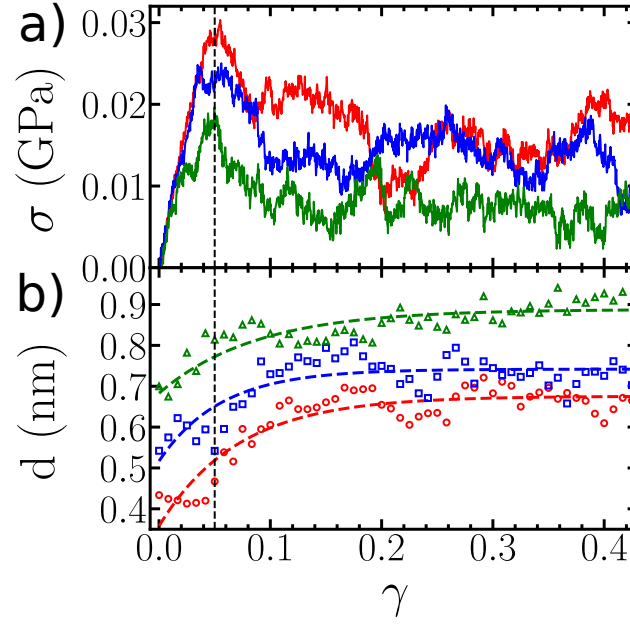
Figure 3.9: (a) Shear stress σ_{yz} and (b) GB layer thickness d as a function of the strain γ at $T = 228K$ and a sliding velocity of $v = 0.1$ m/s. Results for pristine sample and the intermediate and high salinities are shown in red, blue and green, respectively. Colored dashed lines in (b) serve as guides to the eye.

Figure 3.9a) displays its behavior for the three considered salinities as a function of the shear strain, defined as $\gamma \equiv \Delta y / L_z$, with Δy the relative displacement of the grains in the y-direction and L_z the size of the bicrystal in the z direction. The stress-strain curves are qualitatively the same for all cases and resemble the typical behavior of viscoelastic systems. [111, 112, 113, 114, 115, 116, 117, 118, 119, 120] The initial response is elastic in nature, with the shear stress increasing linearly with the strain. In this regime the displacement of the upper grain is small, giving rise to elastic shear deformations of the crystal grains but without evoking any sliding at the GB region. Since the ions are not involved in these small elastic deformations of the crystal grains, the stress-strain curves in this stage are independent of the salinity and overlap. Subsequently, viscous relaxation processes at the GB region start becoming active, first reducing the elastic increase of the shear stress to reach a maximum, known as the yield stress $\sigma_{\max}$, followed by a final decay to a stationary viscous sliding regime at a plateau value σ_{∞}. The yield and stationary-state stresses can be interpreted in terms of effective static and dynamic frictional agents, respectively, with the first representing the stress required to initiate the sliding process, and the second quantifying how much is needed to sustain a steady state.

It is evident that these frictional parameters are affected by the salinity, both of them reducing as the sodium chloride concentration increases. At the same time, the
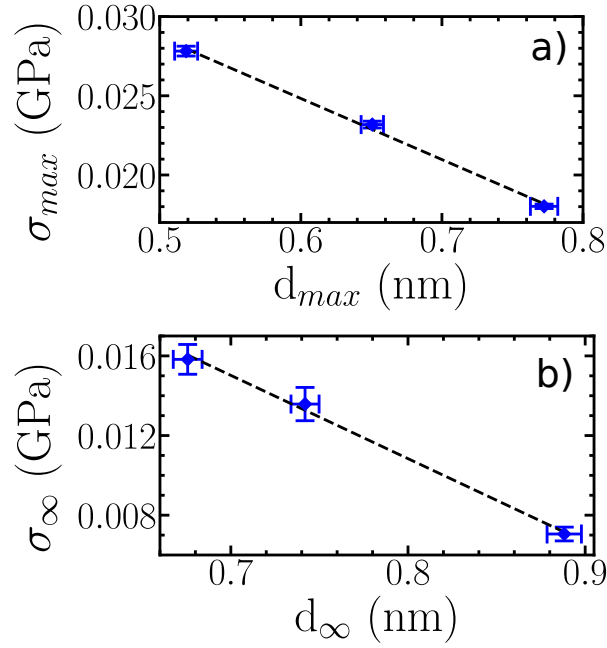
Figure 3.10: Yield stress σ_{max} (a) and the steady-state stress σ_∞ (b) as a function of the GB thickness d. For the yield stress we use the value $d_{\max}$ at which the yield stress is reached, whereas the plateau value d_∞ is utilized in representing the steady-state stress.

thickness of the GB layer during the sliding process also evolves differently for the 3 cases, as shown in Fig. 3.9b). Starting from their equilibrium values, the GB thicknesses rapidly increase in the initial stage of the sliding process after which a plateau value in the steady-state sliding regime is reached. The latter is $\sim 20\%$ larger than the corresponding equilibrium value. Indeed, both the yield stress and the steady-state stress values correlate with the thickness of the GB layer. This is depicted in Fig. 3.10, which displays $\sigma_{\max}$ and σ_∞ as a function of thickness values from Fig. 3.9 b). The yield stress $\sigma_{\max}$ is shown as a function of $d_{\max}$, which is the thickness of the layer when the stress maximum is reached, whereas the stationary values σ_∞ are plotted against the steady-state thickness d_∞. In both cases, there is a distinct linear decrease of the frictional parameters with the GB thickness. Together with the fact that the initial elastic part of the stress-strain curves is independent of the ionic presence, this suggests that the reduction in the frictional parameters is due to the induced increased thickness of the GB region rather than because of specific characteristics of the sodium and chloride ions themselves. This appears consistent with experimental insight that the tensile strength of polycrystalline ice reduces significantly with the brine volume. [159]

3.3.1   Conclusions

In summary, using molecular dynamics simulations based on the TIP4P/2005 water model and the Madrid-2019 force field we have investigated the influence of sodium chloride on the structural and dynamical properties of internal interfaces in proton-disordered hexagonal ice I$_h$. In particular, we consider the interface for the $\Sigma35$ symmetric tilt boundary at 20 K below TIP4P/2005's melting point for different ionic concentrations. In all cases the briny disordered layer at the GB is found to display liquid-like behavior, with structural and dynamical properties that depend on the salinity. In addition to increasing its thickness, the RDFs for water show that the presence of sodium chloride progressively diminishes the degree of structure in the GB region. Comparison to the RDFs in the corresponding bulk sodium chloride solutions, i.e., in absence of crystalline grains, indicates that the structure reduction in the GB region is associated with the progressive dissolution of crystalline domains and the increasing thickness of the GB layer as the sodium chloride concentration is raised.

With regard to the dynamical properties, the presence of the ions substantially alters the mobility of the water molecules in the GB region. Whereas in the pristine sample the time-dependence of the water MSD is sub-diffusive in nature up to time intervals of 100 ns, the highest salt concentration displays Brownian diffusion throughout and MSD values that are almost an order of magnitude larger. At the same time, however, the GB diffusivities are much smaller than those in the corresponding bulk liquid solutions, both for the ions as well as the water molecules. This implies that, even though liquid-like, the briny GB regions behave as quasi-liquid layers, with dynamical properties that are very different from those of the bulk solutions under the same conditions of temperature, pressure and sodium-chloride concentration.

Finally, the briny quasi-liquid layers also affect the GB-sliding process, which involves the relative motion of two crystal grains across the GB plane and constitutes one of the fundamental mechanisms for plastic deformation of polycrystalline systems. As for pristine ice, the sliding process is found to resemble viscoelastic behavior in which the shear stress response to the displacement initiates with a linear-elastic regime, then reaches a stress maximum and finally relaxes to a viscous steady-state value. Both the maximum, which is the stress required to initiate the relative motion, as well as the steady-state value, needed to sustain a steady-state sliding process at a particular velocity, diminish as the ionic concentration in the briny GB layers increases. This is consistent with the

general notion that the presence of sodium chloride facilitates mechanical deformation of ice and indicates that GB sliding is one of the processes contributing to this observation.

Chapter 4

Non-Newtonian flow effects in supercooled water

4.1 Introduction

Supercooled liquid water has been the subject of intense investigation for decades [23, 160] and continues to attract significant attention [161, 162, 163]. Besides the hotly debated issue concerning the possible existence of a second critical point in the supercooled regime [164, 165, 166], there has been a long-standing interest in the behavior of water's viscosity below the melting temperature. Particular topics of interest include the existence of a fragile-to-strong transition [167, 168], the relation between viscosity and molecular diffusion [30] and the effect of pressure [169].

The viscosity η of a viscous fluid is defined as the proportionality constant between the shear stress σ and the corresponding strain rate $\dot{\gamma}$ according to $\sigma = \eta \dot{\gamma}$ [31, 32]. If, for given temperature and pressure, the relation between σ and $\dot{\gamma}$ is linear, i.e., η is constant, the flow behavior of the fluid is said to be Newtonian [32]. Conversely, fluids for which this linearity is violated are referred to as non-Newtonian, with colloidal suspensions, many polymer melts and granular fluids as typical examples [32, 170].

Many fluids display Newtonian flow behavior for sufficiently small rates $\dot{\gamma}$. Liquid water in thermodynamic equilibrium is an example, with a viscosity that is known to be constant across several orders of magnitude of $\dot{\gamma}$ [33]. Much less is known, however, about the dynamical effects on the viscosity of water in its supercooled state. Although its magnitude is known to rise sharply as the temperature is lowered [30, 171], this increase has so far only been probed for the low-rate, Newtonian limit and the question as to whether it displays a shear-rate dependence remains open.

In this chapter we consider this issue for the first time, investigating the influence of the flow-rate on the shear viscosity of supercooled water using atomistic-level simulations. In particular, we employ non-equilibrium molecular dynamics (NEMD) simulations in which we impose shear deformations at a constant rate $\dot{\gamma}$ and measure the associated shear stress σ. To describe the interactions between the water molecules we employ the TIP4P/Ice water model [61], which is among the best molecular models for water [172] and has a melting point $T_m = 271\,K$ that is close to the experimental value. All simulations have been carried out using the LAMMPS package [57]. The long-range intermolecular electrostatic interactions for the TIP4P/Ice model are calculated using the particle-particle particle-mesh (PPPM) scheme [56] and the intramolecular bond lengths and angles are held fixed using the SHAKE algorithm [64].

4.2 Computational details

All the flow simulations are carried out using a computational cell containing 10800 water molecules. The cells are first allowed to equilibrate at zero external pressure and constant temperature, allowing fully flexible cells. This is achieved using a Parrinello-Rahman-type barostat [108] and a Langevin thermostat [53] with damping constants of 2 and 0.2 ps, respectively. The corresponding equations of motion are integrated using velocity-Verlet algorithm with a time step of $\Delta t = 1$ fs. Subsequently, the nonequilibrium flow simulations are carried out at constant volume and isothermally, with temperature control implemented using a Langevin thermostat with a damping constant of 0.2 ps. The pure shear deformations are imposed using LAMMPS's `fix deform` command with the `remap x` option, allowing the molecules to adjust to the cell deformation without requiring an explicit velocity profile. This approach has shown to give good agreement with the alternative SLLOD approach [173]. Due to the appreciable cell distortions during the

NEMD simulations, the reciprocal space part of the PPPM scheme is reset several times during a run, approximately after every $\sim 1\%$ of deformation.

4.3 Results and discussion

Fig. 4.1 displays the evolution of the shear stress as a function of the accumulated strain, $\gamma = \dot{\gamma} t$, along six flow simulations at the deeply supercooled condition at $T = 226\,K$.

The stress-strain curves display non-monotonic behavior that is typical of viscoelastic fluids, as has been observed in a variety of systems, both experimentally as well as in simulations [111, 112, 113, 114, 115, 116, 117]. At the early stages of the flow process the stress increases linearly with strain, typifying a solid-like elastic response characterized by a modulus that is independent of the deformation rate. Subsequently, the contribution of viscous relaxation processes becomes significant, first reducing the elastic increase of the shear stress to reach a maximum, σ_{max}, followed by a final decay to a steady-state plateau value, σ_∞. Both σ_{max} and σ_∞ decrease as the flow rate is reduced, as the stress relaxation processes are active during longer periods of time for a given state of deformation. Indeed,
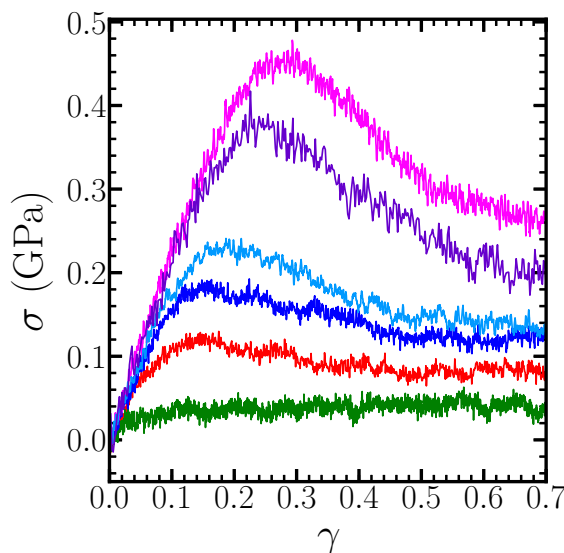
Figure 4.1: Shear stress as a function of the accumulated strain at $T = 226\,K$ for $\dot{\gamma} = 2 \times 10^7$ s^{-1} (green), 2×10^8 s^{-1} (red), 1×10^9 s^{-1} (dark blue), 2.5×10^9 s^{-1} (light blue), 2.5×10^{10} s^{-1} (purple), and 5×10^{10} s^{-1} (magenta).

for $\dot\gamma = 2 \times 10^7$ s^{-1} the stress maximum has disappeared altogether and the stress-strain curve rises monotonically to its steady-state value.

The plateau value σ_∞ is the shear stress that is required to maintain steady-state flow at a prescribed rate $\dot\gamma$ and the corresponding steady-state shear viscosity is then given by

$$\eta_\infty(\dot\gamma) \equiv \sigma_\infty(\dot\gamma)/\dot\gamma. \tag{4.1}$$

Fig. 4.2a) displays this viscosity as a function of flow rate for supercooled TIP4P/Ice water at 226 K, 246 K and 266 K, respectively. For all three temperatures the flow response can be classified into two regimes. For low rates the viscosity is independent of $\dot\gamma$, meaning that flow is Newtonian under these conditions. Subsequently, there is a cross-over into a non-Newtonian regime in which the viscosity decreases with growing flow rates, also known as shear thinning. Furthermore, this cross-over depends strongly on the temperature: while at 226 K non-Newtonian behavior sets in for $\dot\gamma \gtrsim 10^7$ s^{-1}, the Newtonian flow regime persists up to flow rates of $\dot\gamma \sim 10^{10}$ s^{-1} at 266 K.

To quantify the cross-over between Newtonian and non-Newtonian flow we analyze the simulation data in terms of the Carreau model [174, 175, 176, 177], which provides a
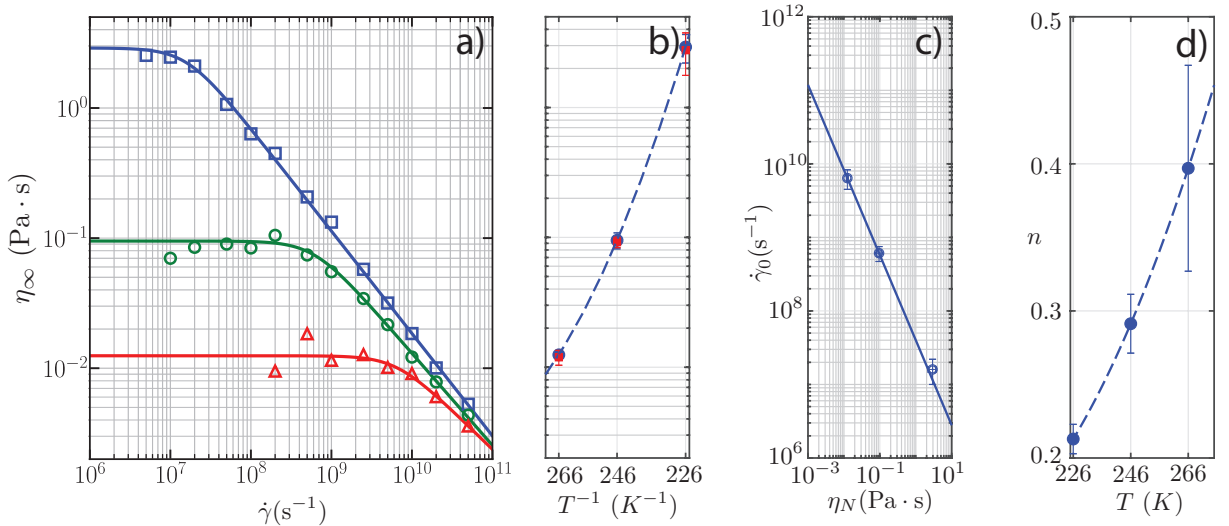
Figure 4.2: a) NEMD shear viscosity as a function of the flow rate for supercooled TIP4P/Ice water at $T = 226$ (squares), 246 (circles) and 266 K (triangles). Error bars are smaller than symbol size and are not shown. Solid lines correspond to fits of the viscosity data to the Carreau model, Eq. (4.2). b) Comparison of Carreau estimate for η_N (circles) to Green-Kubo results (squares), as a function of the inverse temperature $1/T$. c) Characteristic cross-over rate $\dot\gamma_0$ as a function of η_N. Full line represents power-law fit with exponent -1.16 ± 0.01. d) Shear thinning exponent n as a function of temperature T. Dashed lines in b) and d) represent guides to the eye. Error bars in b), c) and d) correspond to 95% confidence intervals.

phenomenological description of shear thinning that has shown to be accurate for fluids with relatively low Newtonian viscosities, $\eta_N \lesssim 1$ Pa·s [177], which is the case for the present TIP4P/Ice simulations. The Carreau model treats shear flow as a stress-assisted thermally activated process involving a broad distribution of energy barriers and gives a shear viscosity that depends on the flow rate according to [174, 175, 177]

$$\frac{\eta_\infty}{\eta_N} = \left[1 + \left(\frac{\dot{\gamma}}{\dot{\gamma}_0}\right)^2\right]^{\frac{n-1}{2}}, \tag{4.2}$$

where η_N is the Newtonian viscosity, $\dot{\gamma}_0$ is a characteristic cross-over rate and n is the shear-thinning exponent with a value between 0 and 1. In the limit of large flow rates this model gives rise to a power-law decay of the viscosity according to $\eta_\infty \sim \dot{\gamma}^{n-1}$.

The lines in Fig. 4.2a) depict the least-squares regression results for the Carreau model of Eq. (4.2) with respect to the NEMD viscosity data. The agreement between model and simulation is very good across the entire range of flow rates for all three temperatures, clearly showing a power-law dependence of the viscosity in the shear thinning regime. The accuracy of the Carreau model can be further verified by comparing its estimate for the Newtonian viscosity η_N to results from independent equilibrium calculations. Specifically, since η_N represents the shear viscosity in the limit of vanishing flow rate, it can be computed using the Green-Kubo (GK) formalism [109, 178, 179], which expresses it in terms of stress-stress autocorrelation functions that can be computed using equilibrium MD simulations. The equilibrium runs used to compute the GK viscosities are based on a cubic cell containing 2000 water molecules that are first equilibrated at zero pressure and constant temperature using the same approach used for the 10800-molecule cells. Subsequently, five independent NVT equilibrium runs are carried out to sample the components of the stress tensor and determine the stress-stress autocorrelation functions $\langle P_{\alpha\beta}(0)P_{\alpha\beta}(t) \rangle$, where $P_{\alpha\beta}$ is an off-diagonal component of the stress tensor. The Green-Kubo viscosities are then computed as

$$\eta_N = \frac{V}{k_B T} \int_0^\infty \langle P_{\alpha\beta}(0)P_{\alpha\beta}(t) \rangle dt,$$

with V the volume of the system, T the temperature, and k_B Boltzmann's constant. Aside from the three off-diagonal components P_{xy}, P_{xz}, and P_{zy}, there are two other independent components, $\frac{1}{2}(P_{xx} - P_{yy})$ and $\frac{1}{2}(P_{yy} - P_{zz})$, that can be used due to rotational invariance [180]. Accordingly, η_N is estimated using the average over these five components

and over five independent equilibrium runs.

Fig. 4.2b) presents a comparison between the NEMD Carreau results and equilibrium GK shear viscosities. The agreement is excellent for all three temperatures, providing further validation of the Carreau model as an adequate descriptor of the rate dependence of the shear viscosity in supercooled TIP4P/Ice water. A further observation based on the results in Fig. 4.2b) is that supercooled TIP4P/Ice water behaves as a fragile liquid for the considered temperatures [181], given that the logarithm of η_N as a function of the inverse temperature $1/T$ is supralinear, constituting super-Arrhenius behavior.

The two other parameters of the Carreau model quantify the nature of the Newtonian to non-Newtonian transition and their behavior is plotted in Figs. 4.2c) and d). Fig. 4.2c) plots the characteristic rate $\dot{\gamma}_0$ as a function of the Newtonian viscosity η_N. As noted before, the transition to the shear-thinning regime sets in for lower flow rates as the temperature reduces and the Newtonian viscosity grows. More interestingly, the functional dependence is well described by a power law with exponent -1.16 ± 0.01, implying a direct relationship between the nonequilibrium parameter $\dot{\gamma}_0$ and the equilibrium property η_N. Fig. 4.3c) shows that the shear thinning exponent n decreases substantially as the degree of supercooling is enhanced, implying that the shear-thinning effect becomes more pronounced as the temperature is reduced. We will further discuss this point below.

There are a number of microscopic processes that can lead to the power-law viscosity behavior of the Carreau model seen in Fig. 4.2a) [177]. A common mechanism concerns a change in some order parameter that describes correlations between neighboring molecules [177, 182]. For instance, for shear thinning in fluids composed of chain molecules, a relevant order parameter is one that measures their alignment along the flow direction [183, 184]. Here, we investigate the evolution of the hydrogen bonding during the flow simulations. To determine the hydrogen-bond statistics, we adopt the definition that a HB is present whenever the distance between a proton and an oxygen satisfies 1.1 Å$< d_{\mathrm{OH}} < 2$ Å. Fig. 4.3a) displays the mean number of hydrogen bonds (HBs) per molecule, n_{hb}, as a function of strain at $T = 246\ K$ for the flow rates $\dot{\gamma} = 2 \times 10^8$, 2.5×10^9 and 5×10^{10} s^{-1}. These particular three values correspond to the Newtonian, the cross-over and shear-thinning regimes for this temperature, respectively. In the Newtonian regime n_{hb} remains constant throughout the entire simulation and the connectivity of the HB network remains unaffected by the flow. As the rate increases to the Carreau cross-over value, however, the steady-state HB connectivity becomes discernibly lower, reducing even further for the highest flow rate.
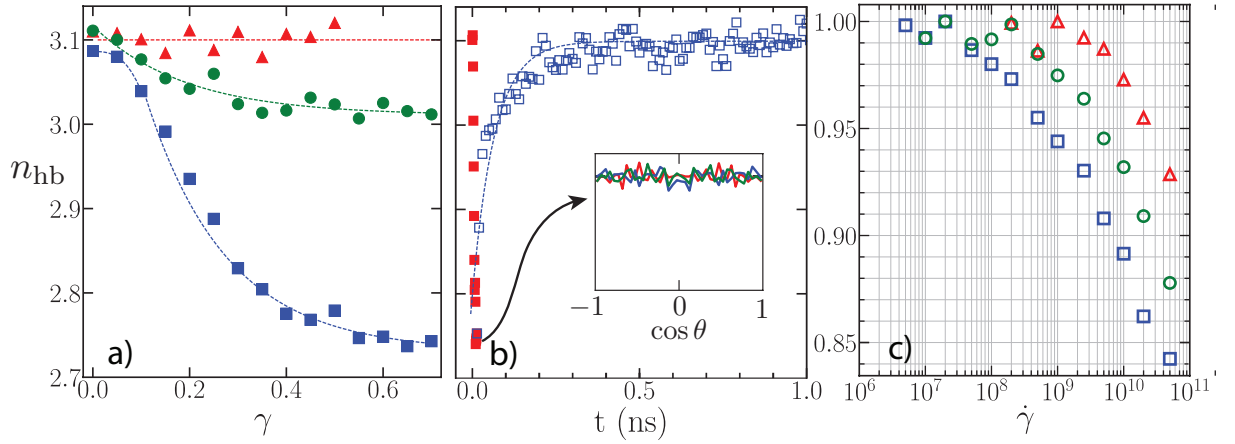
Figure 4.3: Average number of hydrogen bonds per molecule n_{hb} during flow simulations at $T = 246$ K. (a) Results for $\dot{\gamma} = 2 \times 10^8$ (triangles), 2.5×10^9 (circles) and 5×10^{10} s^{-1}, respectively. Dashed lines serve as guides to the eye. (b) Temporal evolution of n_{hb} during a simulation in which the system is first subjected to a constant flow rate of $\dot{\gamma} = 5 \times 10^{10}$ s^{-1} until reaching a total shear of $\gamma = 0.7$ (filled squares), after which the deformation is instantaneously halted and the system is allowed to relax at a fixed cell geometry (open squares). Lines in inset display distribution of HB direction cosines with respect to x (red), y (blue) and z (green) directions at $\gamma = 0.7$.(c) Variation of n_{hb} normalized by its equilibrium value as a function of $\dot{\gamma}$.

As mentioned above, molecular alignment during the shearing process may also possibly play a role in the shear thinning, as is the case in systems where elongated molecules are involved [183, 184]. To verify this possibility for water we analyze the statistics of HB directions during the shearing process. As seen in the inset of Fig. 4.3b), the HB direction cosines with respect to the x, y and z directions are uniformly distributed, indicating that the HB directionality is isotropic, displaying no preferred alignment direction.

These results indicate that the shear thinning arises from the reduction of HB connectivity, which is consistent with theoretical arguments [185]. The origin of this decrease and its dependence on the flow rate is associated with time-scale differences between the imposed flow and molecular rearrangements. In the Newtonian regime the latter is sufficiently short for the molecular rearrangements to accompany the imposed flow and maintain the average connectivity of the HB network. In the non-Newtonian shear-thinning regime this is no longer the case, with the molecular orientations systematically lagging behind the imposed flow, leading to the reduction of the HB connectivity in the steady state flow. This is illustrated in Fig. 4.3b) which depicts the time evolution of n_{hb} along a simulation in which the system is first subjected to a constant flow rate of $\dot{\gamma} = 5 \times 10^{10}$ s^{-1} at 246 K until reaching its steady state, after which the deformation

is halted and the system is allowed to relax at a fixed cell geometry. During the flow stage the mean number of HBs per molecule rapidly decreases to its steady-state value. Subsequently, after halting the deformation, n_{hb} relaxes to its equilibrium value by an approximately exponential process with a time constant $\tau_m \simeq 0.07$ ns. While this time scale is ~ 300 times shorter than that associated with the lowest flow rate in Fig. 4.3a), it is ~ 3 times larger compared to that of the highest.

Finally, the increasing intensity of the shear-thinning effect with reducing temperature, as reflected by the decrease of the Carreau exponent n in Fig. 4.2d), also correlates with the evolution of the average number of n_{hb}. This is shown in Fig. 4.3c) which depicts the steady-state flow values of n_{hb}, normalized by their equilibrium values n_{hb}^0, as a function of the flow rate for $T = 226$, 246 and 266 K, respectively. Due to the shear thinning effect, as seen in Fig. 4.2a), n_{hb} decreases as the flow rate grows. Moreover, this decrease is stronger in relative terms as the temperature is lowered: whereas for $\dot{\gamma} = 5 \times 10^{10}$ s^{-1} a reduction of $\sim 15\%$ with respect to its equilibrium value is observed at 226 K, it is only $\sim 6.5\%$ at 266 K.

4.4   Conclusions

In conclusion, we have performed a series of NEMD simulations to investigate the shear-rate dependence of the viscosity of supercooled water as described by the TIP4P/Ice model for three different degrees of supercooling. In all cases we find a distinct Newtonian-to-shear-thinning crossover that is well-described by the Carreau model. The shear-thinning effect becomes stronger as the temperature is reduced, with a thinning exponent that decreases and with non-Newtonian behavior setting in for lower deformation rates. Interestingly, the results suggest a power-law relationship between the nonequilibrium cross-over rate parameter $\dot{\gamma}_0$ and the equilibrium Newtonian viscosity property η_N. On the molecular scale the shear thinning correlates with a significant reduction in the connectivity of the HB network, which is associated with time-scale differences between the deformation protocol and molecular rearrangements. Moreover, the connectivity reduction increases in relative terms as the temperature is lowered, giving rise to the stronger shear-thinning effect at lower temperatures.

Chapter 5

Sampling supercooled water states by pulsed heating simulations

5.1 Introduction

It is known that many water properties display unusual behavior, and there is a lot of debate whether or not this anomalies arises from structurally distinct components, corresponding to high- and low-density regions. Based on different water models, and on the criteria to sort the water molecules into two different categories [37, 38, 39, 40, 41, 42], computer simulations show a sigmoid-like dependence of each component with respect to the temperature. At ambient conditions, it is experimentally difficult to assign the signature of these local components, because such structural motifs would form and disappear very fast due to large thermal fluctuations. On the other hand, even with slower water dynamics in the supercooled region, it is difficult to overcome the rapid crystallization kinetics in the timescale of the experimental measurements. There have been many recent experimental attempts to probe supercooled water properties in the temperature region known as "no man's land", that is above $\sim$160 K and below $\sim$230 K. [43, 44, 45, 46, 47, 48]. Recently, based on a novel experimental technique to bypass the fast kinetics of crystallization, Kringle *et al.* [43] provided evidence that supercooled water can be described as a mixture of two structurally distinct components.

The experimental technique based on a pulsed laser heating system was developed by Xu *et al.* [186] to investigate the dynamics and kinetics of nanoscale liquid films on

the nanosecond time scale. In this laser heating scheme, a $\sim$15 nm water film on Pt(111) or graphene/Pt(111) with the structure of low-density amorphous (LDA) ice is prepared by vapor deposition at 70 K, followed by annealing at a temperature just below the glass transition ($T_g \sim$ 136 K). The LDA film is then repeatedly heated to a temperature T_{max} with nanosecond laser pulses with heating rates greater than 10^9 K/s. [186] For each pulse, the films spent $\sim$3 ns near T_{max}, where the sample is supposed to be in the liquid state, and then the system is quenched to the base temperature $T_0 = 70$ K with cooling rates also greater than 10^9 K/s. [186] After quenching, the system stays at the glassy state for a much larger period of time, about 1 s during which its structure is interrogated with infrared spectroscopy to assign the fraction of water molecules with vibrational signals of ice, LDA and high temperature liquid water. The reference for the latter is the structure of hyperquenched water (HQW). The fast heating and cooling pulses are repeated for a finite number of times while the evolution of the film is followed at $T_0 = 70$ K. This procedure allows for a decoupling of the measurement time at T_0 from the relaxation time at T_{max}. The methodology has been used to study the diffusivity of supercooled water [187], the homogeneous ice nucleation rate and crystallization kinetics [188, 189], as well as the structural and relaxation properties of deeply supercooled water [43, 44]. Their use of this methodology to derive properties of liquid supercooled water are based on two assumptions. First, that evolving the film through a series of pulses that transiently heat water to near T_{max}, is equivalent to evolving the film in an isothermal experiment during a time that corresponds to the sum of those of the heating pulses. Second, that the quenched IR spectra measured at T_0 reflects the steady-state structure of water at T_{max}. To date, the validity of these assumptions has not been verified.

By using infrared (IR) spectroscopy to track the structural transformations, Kringle *et al.* [43, 44] estimated the fraction of high- and low-temperature structural motifs in supercooled water within the framework of a two-state "mixture" model for water. [38, 41, 190, 191, 192, 193, 194] Based on the ratio on the intensities of vibrational bands assigned to the two different structural motifs, Kringle *et al.* concluded that the Widom temperature at ambient pressure is located at 210 K $\pm$ 3 K [43]. This is significantly lower than the 229 K Widom temperature predicted from isothermal compressibility and correlation lengths computed from x-ray scattering data.[46]. This raises the question of why the Widom line location is shifted to lower temperatures in the pulsed experiments.

Here we implement the methodology of Kringle *et al.* [43, 44] in molecular dynamics (MD) simulations with the TIP4P/Ice model of water. [61] Our aim is to assess whether

the evolution of water through discrete pulses between T_0 and T_{max} is equivalent in both structures and relaxation times to the continuous evolution of the system at T_{max}. To test the core assumptions of the methodology we consider bulk water instead of thin films, and test both "square" pulses that heat and cool the sample instantaneously as well as "trapezoidal" pulses with the timescales of heating, cooling and constant temperature at its top that mimic the shape of the pulses reported in the experiments. [43, 44] We find that supercooled water can be equilibrated by heating pulses independently of the shape of the pulse. However, the structure measured at T_0 overestimates the tetrahedrality, and as a consequence, the Widom temperature is shifted to higher temperatures. We also find that the Widom temperature based on the analysis of the structure is quite sensitive to the normalization procedure, i.e. where the fraction of the low-temperature liquid is set to be zero. Furthermore, the structural relaxation time depends on the shape of the pulse, and also on the initial configurations. Thus, the structural relaxation rates do not correspond to equilibrium relaxation rates.

5.2   Methods

We carry out all-atom simulations by using the molecular dynamics (MD) package `LAMMPS`. [57] The interactions between the water molecules is described by the TIP4P/Ice model. [61] The long-range intermolecular electrostatic interactions for the TIP4P/Ice model are handled using the particle-particle particle-mesh (PPPM) scheme [56], the intramolecular bond lengths and angles are held fixed using the SHAKE algorithm [64], and the corresponding equations of motion are integrated using a time step of 1 fs. The number of neighbors are computed up to the first minimum of the oxygen-oxygen pair distribution functions -computed with the Open Visualization Tool (`Ovito`) package. [100]-, at 3.35 Å.

While the temperature is kept at T_{max} or T_0, the system is relaxed at zero external pressure through the isothermal isobaric (NPT) ensemble using a Nosé-Hoover thermostat and barostat with damping parameters of 0.1 ps and 1 ps, respectively. For all simulations, T_0 is always 100 K. In order to quench (or heat) the system, we use the velocity rescaling method (using the standard `fix temp/rescale` combined with `fix nve` for time integration) for 10 MD steps, where the thermostat enforces rescaling every step for all atoms. In this case, we assume that the rate of cooling and heating are infinite, thus producing a

periodic "square" pulse. Additionally, without the velocity rescaling method, we perform heating and cooling ramps in the NPT ensemble to produce a periodic "trapezoid" pulse. We also run isothermal simulations in the NPT ensemble, where the temperature is kept at T_{max} for the entire simulation time.

To prepare the initial sample, we start with a 4000 water molecules cubic periodic cell. In order to obtain an initial less structured liquid without any thermal effects, the water cells are first equilibrated in the NPT ensemble at 350 K and zero external pressure, followed by energy minimization to obtain the inherent structure (IS) [23, 39, 195]. This is equivalent to the hyperquenched water (HQW) initial sample used in the pulsed heating experiments. We also use a low-density amorphous (LDA) initial sample at 100 K prepared by isobaric cooling at 5 K/ns.

5.3   Results and discussion

5.3.1   Supercooled water can be equilibrated through heating pulses

To assess whether the structure of supercooled water can be evolved from hyperquenched water (HQW) to the equilibrium structure at a temperature T_{max} in the deeply supercooled region through the application of discrete heating pulses, we perform simulations using the TIP4P/Ice model, which reproduces well the properties of water, [61] including the structure of the liquid and the melting temperature $T_m = 271$ K [103]. A recent study indicates that TIP4P/Ice has a metastable liquid-liquid critical point at $T_c = 188 \pm 1$ K and $P_c = 1739 \pm 6$ bar [102], and previous calculations of the isothermal compressibility at 1 bar place the Widom line at around 245 K [196] for ambient pressure.

To mimic the experimental procedure, we start from water glass and evolve it to a temperature T_{max} between 220 and 250 K following three protocols: continuous heating, square pulse heating and trapezoidal pulse heating. In the continuous heating, we start from the inherent structure of HQW made from water at 350 K or LDA obtained by isobaric cooling water to 100 K at a rate of 5 K/ns, turn the thermostat to T_{max} and evolve the system continuously at that temperature. For the square pulse heating we start from HQW and evolve the system through a series of "square" pulses that instantaneously
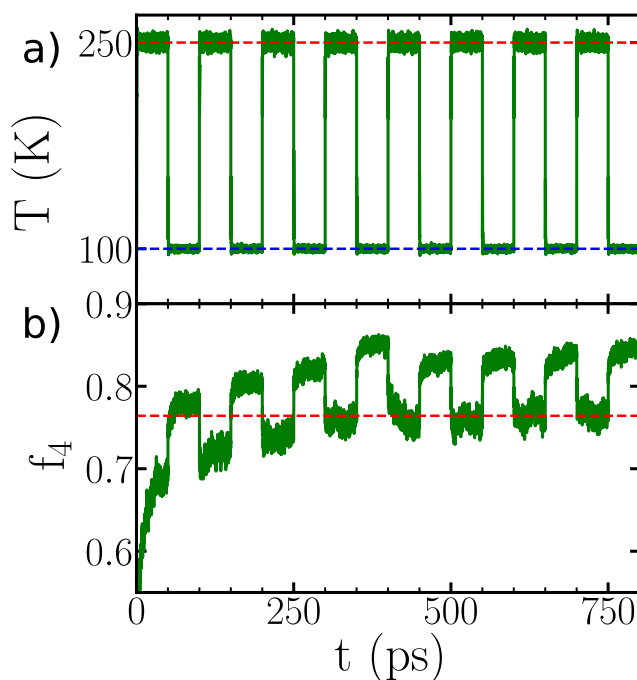
Figure 5.1: Structural evolution of the liquid in our pulsed heating simulations. Time evolution of the (a) temperature and the (b) fraction of four-coordinated molecules within the first coordination shell up to a cutoff distance of 3.35 Å. The dashed lines in (a) indicate $T_{max} = 250$ K (red) and $T_0 = 100$ K (blue), while the red dashed line in (b) is the average of f_4 at 250 K obtained from isothermal simulations at 250 K. The cooling and heating rates correspond to $\sim \pm 10^5$ K/ns.

shift the thermostat from $T_0 = 100$ K to a T_{max} where the system is evolved for $\Delta t_H = 50$ ps and then instantaneously cooled back to T_0 and evolved at the cold temperature for $\Delta t_L = 50$ ps. For the third protocol, we start from HQW and evolve the system with "trapezoidal" pulses, each consisting of heating from $T_0 = 100$ K to T_{max} in 100 ps, evolve the system continuously at T_{max} for 50 ps, cooling from T_{max} to $T_0 = 100$ K in 400 ps, and evolve at the cold temperature $T_0 = 100$ K for 50 ps. In this way, the heating and cooling ramps correspond to 2 and 8 times the time spent at T_{max}, while in the experiment, this ratio corresponds to 2.5 and 10 times, respectively, as illustrated in Fig. 5.5 a). The pulses used in the simulations are shorter than the $\sim$3 ns ones of the experiments, because -we show below- the relaxation of TIP4P/Ice water is faster than that for real water. We characterize the structure of liquid water through the oxygen-oxygen pair distribution function fraction and the fraction of four-coordinated molecules f_4 within the first coordination shell. [38]

Fig. 5.1 a) represents the time evolution of the temperature in our square pulse heating simulations. This choice of $\Delta t_H = 50$ ps and $\Delta t_L = 50$ ps allows enough time

for the barostat to relax the computational cell volume, and maintain the pressure close to zero at both T_{max} = 250 K and T_0 = 100 K. In the time scale of Fig. 5.1 a), the temperature pulses are almost perfectly square, as it takes only ~1 ps for the system to reach the target temperature. Fig. 5.1b) shows the time evolution of f_4 in the pulsed heating simulations with T_{max} = 250 K. In the initial state, ~55 % of the water molecules have four neighbors in their first shell if the relaxation starts from the IS of water at 350 K. The fraction of four-coordinated molecules increases when the temperature is switched to T_{max} = 250 K, as the structure of the liquid relaxes from the glass with the IS of water at 350 K towards the more tetrahedral order at 250 K. Furthermore, the rapid quenching to 100 K results in further increase of f_4. Thus, even though the system is under fast heating and cooling conditions, f_4 at 250 K gradually evolves to a steady-state value characteristic of that temperature, obtained from isothermal simulations at 250 K. Fig. 5.2 a) shows that for the "square" pulses, the stationary values f_4^{SS} at T_{max} between 220 and 250 K are very close to the ones obtained from isothermal simulations, which validates our procedure for other temperatures below 250 K and indicate that the supercooled liquid can be equilibrated by "square" pulses. By following the third protocol with T_{max} = 220 K, the temperature and structure evolve in a similar way, that is with stationary values similar to those of the "square" pulses. Thus, the stationary value f_4^{SS} at T_{max} is also close to the expected value as indicated in Fig. 5.2 a). Therefore, the supercooled liquid can be equilibrated independently of the shape of the pulse.

5.3.2 Structure measured at T_0 overestimates the tetrahedrality

Because of the high cooling rates used in the experimental procedure of Kringle *et al.* [43], it was assumed that the structure measured at T_0 = 70 K corresponded to the inherent structure of the water film. Fig. 5.1b) shows that f_4 at T_0 = 100 K evolves to a different steady-state value. Fig. 5.2 a) shows that the stationary values f_4^{SS} obtained at T_0 are very close to the f_4 values computed from the corresponding inherent structure of T_{max}. Thus, the structural measurements at T_0 are equivalent to the inherent structure of T_{max}. One striking difference between the steady-state structures obtained at T_{max} = 250 K and T_0 = 100 K for the "square" pulses is the normalized distribution of the fourth and fifth neighbor distances, as shown Figure 5.3 a) and b), respectively. When the system reaches a steady-state configuration at T_{max} = 250 K, both distributions are broader. After rescaling the velocities, which corresponds to cooling from 250 to 100 K, the distributions are still very similar; however, after 0.05 ps, while the volume is being
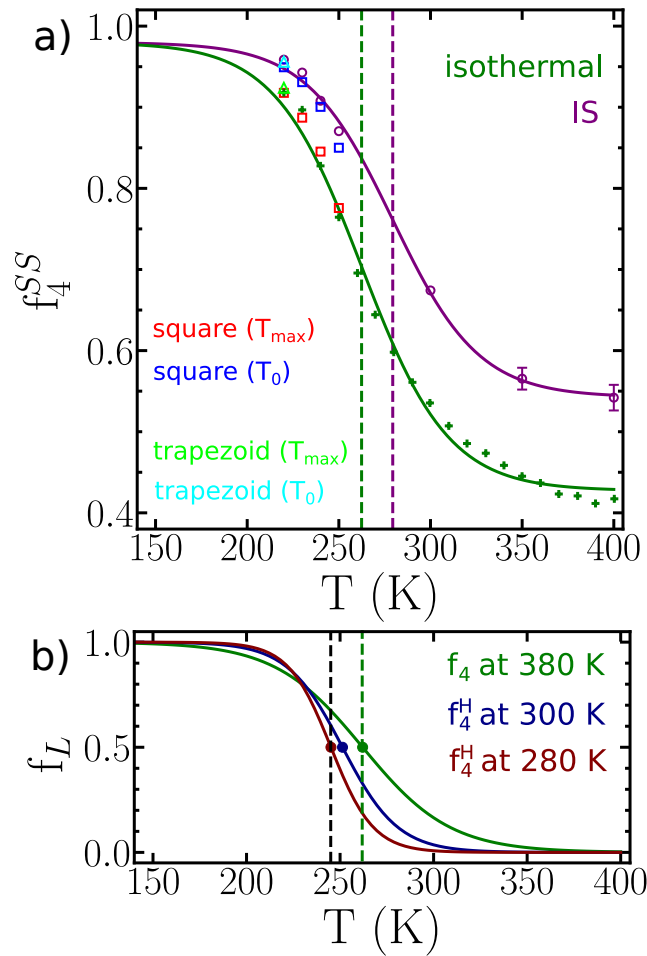
Figure 5.2: The (a) steady-state fraction of four-coordinated molecules, and the (b) normalized fraction of the low temperature liquid f_L as a function of temperature. In a) data points correspond to the average of three independent simulations: isothermal simulations (dark green crosses), the inherent structure (purple circles), the steady-state values obtained for the "square" pulses at T_{max} (red squares), and at $T_0 = 100$ K (blue squares), as well as for the "trapezoidal" pulses at T_{max} (light green triangle) and at T_0 (cyan triangle). Continuous lines correspond to a fit of Eq. 5.1 to the data, and the dashed lines indicate the location of the inflection point. All points were obtained with the same cutoff of 3.35 Å. In b), colors correspond to different values of the fraction of four coordinated molecules in the high temperature liquid f_4^H. The continuous lines correspond to a sigmoid curve fit, the circles indicate the location of the inflection point, and the black dashed line indicates the maxima in isothermal compressibility K_T located at ~245 K. [196]

adjusted by the barostat, we observe an intermediate distribution in both cases. After 1 ps, the volume decreases by ~2.6 % to keep the targeted pressure close to zero, and both distributions are similar to the steady-state structure obtained at the end of the cooling cycle at $T_0 = 100$ K. In average, these neighbor distance changes seem to happen very quickly - less than 1 ps. It seems that after cooling followed by volume relaxation, the fourth neighbor, which is inside the first coordination shell, tend to become closer to the
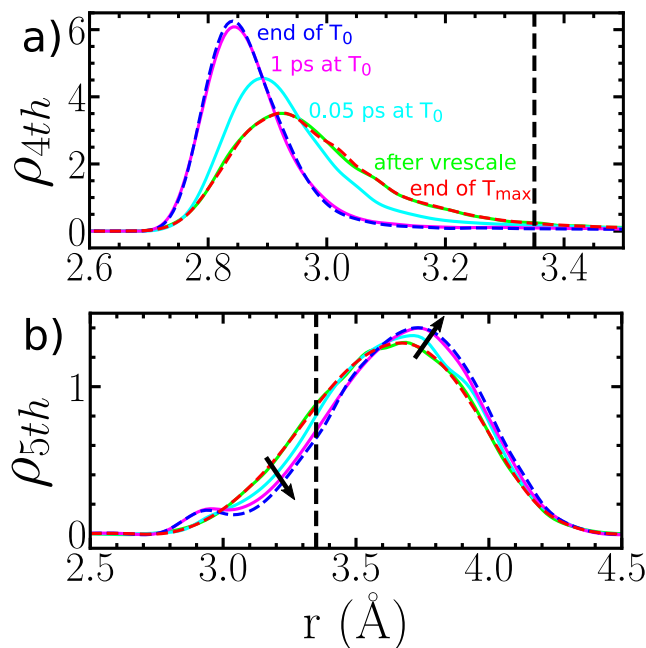
Figure 5.3: Average changes in the fourth- and fifth-neighbor distances after cooling abruptly. Normalized distributions of (a) fourth-neighbor, and (b) fifth-neighbor distances for the steady-state configuration obtained at the end of the heating (T_{max} = 250 K, red dashed line) and cooling (T_0 = 100 K, blue dashed line) cycles during the pulsed heating simulations. Different colors represent intermediate configurations: after rescaling the velocities (light green) from 250 to 100 K, after 0.05 ps (cyan) and 1 ps (magenta) at T_0 = 100 K .

central molecule, while the fifth neighbor tends to move out of the first coordination shell, indicating that the structure captured at T_0 is in fact more tetrahedral than the one at T_{max}. Therefore, the structure obtained at T_0 is not representative of T_{max}.

5.3.3   Implication for the Widom temperature

The Widom temperature T_W signals the point of maximum correlation length of the liquid and is expected to be close to the temperature of maxima of isothermal compressibility K_T and heat capacity C_p. For TIP4P/Ice at 1 bar the maximum in K_T is at ∼245 K [196] and the maximum in C_p at ∼240 K [17]. It is noteworthy that these two extrema are so similar, considering that the maximum in C_p and K_T separate far from the liquid-liquid critical point [197] that has been recently located at T_c = 188 ± 1 K and P_c = 1739 ± 6 bar for the TIP4P/Ice model. [102]

To compare our predictions with those of ref. [44], we here compute the Widom

temperature not from the correlation length but from the change in the structure of the liquid. We compute T_W from the temperature dependence of the stationary state fraction of four-coordinated water molecules f_4^{SS} obtained from continuous isothermal simulations (as they reach the same stationary state as square pulses but are computationally less expensive). We follow the procedure of ref. [44] and obtain the Widom temperature from a fit of f_4^{SS} to the the logistic function as represented by the full lines in Fig. 5.2 a),

$$f_4^{SS}(T) = f_4^L + \frac{f_4^H - f_4^L}{1 + e^{-(T-T_W)/\Delta T_W}}, \tag{5.1}$$

where we fit the inflection point T_W, the steepness of the curve ΔT_W and the fraction of four coordinated molecules in the high temperature liquid f_4^H, while setting the maximum fraction of four-coordinated molecules in the low temperature liquid f_4^L. The need to set f_4^L arises from a lack of equilibrated data points at very low temperatures. The Widom temperature for the change in structure in TIP4P/Ice is $T_W = 262 \pm 1$ K if 3.35 Å is used as cutoff for the counting of neighbors, and 254 ± 1 K if the cutoff increases to 3.5 Å, while the steepness ΔT_W is insensitive to the selection of the cutoff. Although the T_W obtained from the analysis of the structure are close to the maxima in isothermal compressibility, $\sim$245 K, [196] and heat capacity, $\sim$240 K, [17] of the model, their dependence on the criterion used to divide the liquid into two distinct local orders indicates that there is not a unique way of identifying the Widom line from an analysis of the structure of liquid water.

The structure of water in the pulsed experiments of Kringle *et al.* [43, 44] was not followed at T_{max} but at $T_0 = 100$ K, which above we show results in structure indistinguishable from the inherent structures of the liquid. We repeat the procedure above through a logistics function fit of the fraction of four coordinated molecules on the inherent structures to obtain a Widom temperature $T_W^{IS} = 279 \pm 2$ K , with a steepness $\Delta T_W = 23 \pm 1$ K identical to the one from the thermal simulations, as shown in Fig. 5.2 a). We note that T_W^{IS} is 17 ± 4 K higher than the T_W determined from the corresponding thermal trajectories with the same cutoff for the number of neighbors, and $\sim$35 K higher than those of the maxima in C_p and K_T for the model.

Through the characterization of the inherent structures, Kringle *et al.* [43] estimated that the Widom temperature is located at 210 K $\pm$ 3 K. As the stationary f_4^{IS} is always higher than the thermal f_4 (see Figure 5.1), the $T_W^{IS} = 210$ K obtained from the experiments at 100 K must be an upper limit to the "true" thermal T_W. Nevertheless,
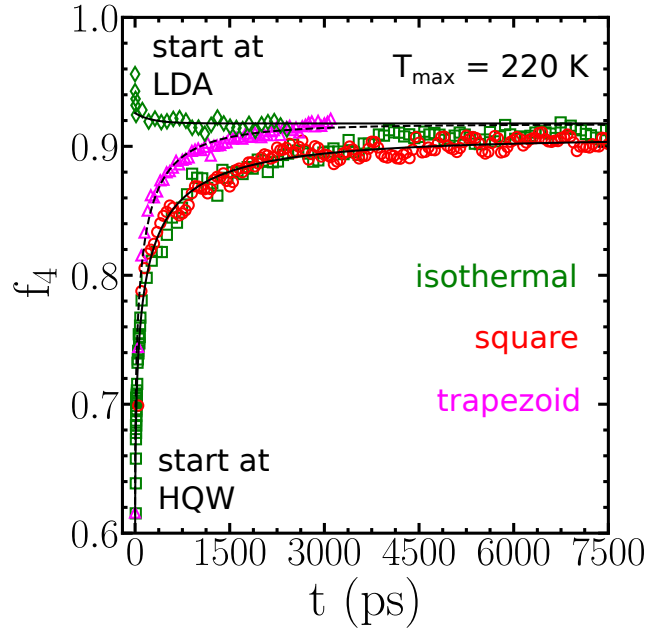
Figure 5.4: Structural evolution of the liquid by counting only the time when the temperature is set to $T_{max} = 220$ K. Starting from HQW, data points correspond to the fraction of four-coordinated molecules f_4 for the isothermal case (green squares), "square" (red circles) and "trapezoidal" (magenta triangles) pulses, as well as the isothermal case when starting from the LDA (green diamonds). The dashed and continuous lines represent a stretched exponential fit to the data, and the parameters β and τ_{rel} are plotted in Fig. 5.6 a) and b), respectively.

$T_W^{IS} = 210$ K is ~ 20 K below the Widom line estimated from the maxima in isothermal compressibility and correlation length extracted from x-ray scattering experiments. [47] We compute the normalized fraction of the low temperature liquid f_L within the two-state analysis. [193] We observe that both the inflection point T_W and the steepness ΔT_W change significantly on where f_L is set to be 0, that is at which temperature one of the normalizing factors f_4^H is selected. In Fig. 5.2 b), if we select f_4^H at 380, 300 and 280 K, T_W is close to 262, 251 and 245 K, respectively. Since the IR spectra measurements cannot resolve differences in structure at temperatures above ~ 245 K, the fraction of the low temperature liquid f_L goes to 0 around ~ 260 K. [43] The lack of data above ~ 260 K may be one possible reason to get a much lower T_W.
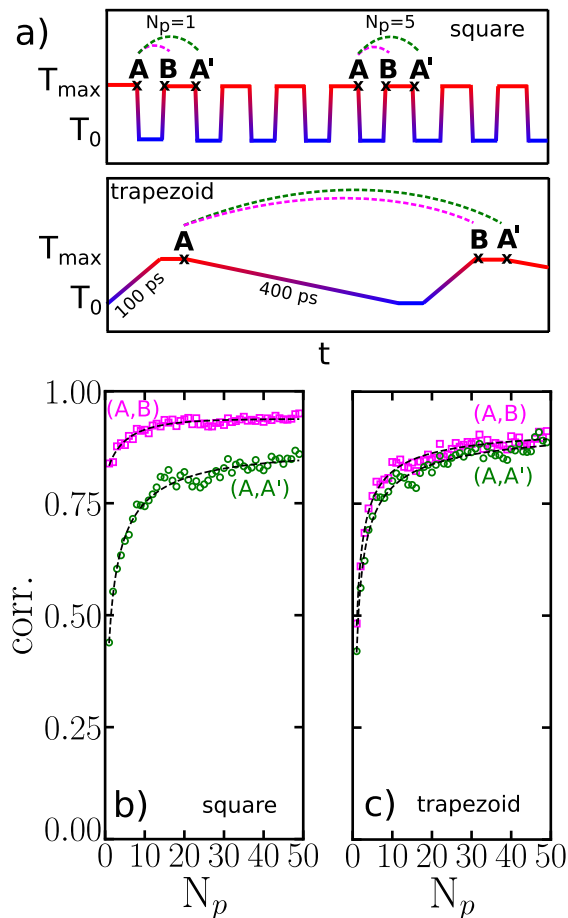
Figure 5.5: Correlation based on the exact same four closest neighbors to quantify the discontinuity introduced after cooling from T_{max} = 220 K to T_0 = 100 K. (a) Scheme for comparing different molecular configurations for two different pulsed heating shapes: square and trapezoid. As illustrated in (a), configuration A represents the end of a particular heating cycle, while B is at the beginning, and A' is at the end of the next one. In order to quantify how much the local structure of the liquid changes after cooling to T_0 = 100 K, we correlate individual molecules and its four closest neighbors when comparing A and B or A and A'. Correlation between configurations A and B (magenta), and A and A' (green) for the (b) square, and (c) trapezoid heating shapes.

5.3.4 The structural relaxation time depends on the shape of the pulse

We follow the time evolution of the fraction of four-coordinated molecules f_4 by counting only the time when the temperature is set to T_{max}, that is, at the top of the pulse, for both the "square" and "trapezoidal" cases. In this way, we can compare the evolution of f_4 with the isothermal case, and check whether or not quenching from T_{max} to T_0 multiple times affects the dynamics at T_{max} towards equilibrium. Following the analysis of Kringle *et al.* [44], the time evolution data can be fitted to the stretched

exponential,

$$f_4(t) = (f_4^0 - f_4^{SS}) \cdot e^{-(t/\tau)^\beta} + f_4^{SS}, \tag{5.2}$$

where f_4^0 and f_4^{SS} are constants and represent the initial and stationary states, respectively, τ is a characteristic time, and β is the stretching parameter. For a stretched exponential, the mean relaxation time is defined by $\tau_{rel} = \frac{\tau}{\beta}\Gamma\left(\frac{1}{\beta}\right)$.

Fig. 5.4 shows the fraction of four-coordinated molecules f_4 as a function of time for $T_{max} = 220$ K. Starting from HQW, the relaxation of f_4 for the square pulse heating looks very similar to the isothermal case, while for the trapezoid pulse heating, f_4 seems to be reaching a steady-state value much faster. Based on the stretched exponential fit, Fig. 5.6 a) and b) indicates that indeed the stretching parameter β and the mean relaxation time τ_{rel} for the "square" and isothermal cases are very similar, even for other temperatures than 220 K. On the other hand, τ_{rel} is significantly smaller for the "trapezoid" one.

In order to quantify how much discontinuity is being introduced after structural relaxation at T_0, as well as the introduction of heating and cooling ramps, Fig. 5.5 a) illustrates the comparison between the two different molecular configurations along the pulses for the two different heating schemes. Considering only the four closest neighbors, we check if each molecule has exactly the same four nearest neighbors in both A and B or A and A' to quantify how much these configurations are correlated. Since we compute this for all molecules, a value of 1 indicates that all the molecules have the exact same four nearest neighbors in both configurations, and a value of 0 indicates the opposite. Fig. 5.5 b) shows that when comparing A and B for the "square" pulse at $T_{max} = 220$ K, ~90 % of molecules have exactly the same four nearest neighbors, indicating that the four closest neighbors are longer-lived neighbors, even though there is significant changes in the neighbor distances after quenching to $T_0 = 100$ K. On the other hand, once the velocities are rescaled to achieve $T_{max} = 220$ K again, part of that correlation is lost when comparing A and A' due to larger thermal fluctuations at such temperature. Thus, it means that the correlations are not lost between the "square" pulses, and quenching to T_0 does not strongly interfere with the dynamics at T_{max}. By doing the same four nearest neighbors analysis for the "trapezoid" pulse with $T_{max} = 220$ K, Fig. 5.5 c) indicates that there is significant relaxation during the cooling and heating ramps, since the correlations (A, B) and (A, A') are similar.
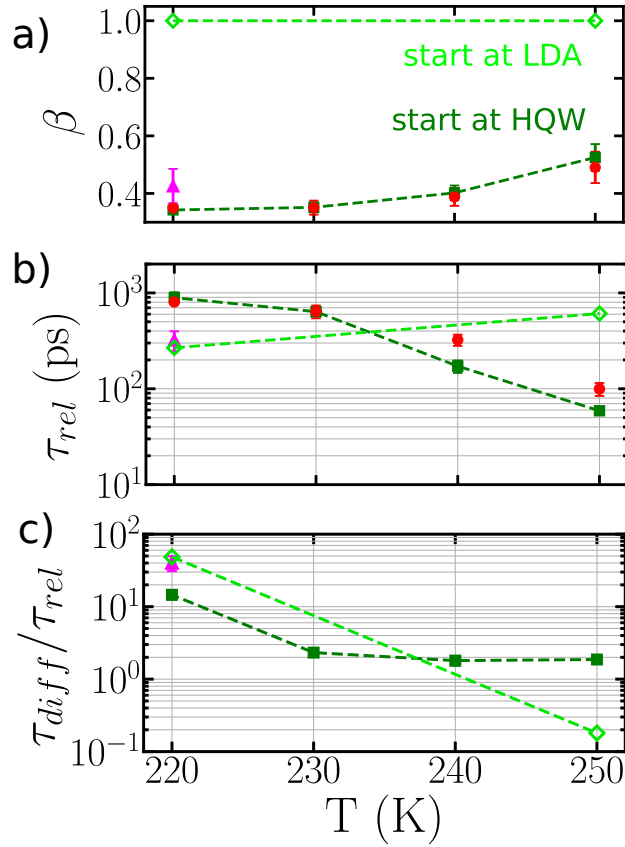
Figure 5.6: Temperature dependence of the relaxation parameters obtained from the stretched exponential fit. The (a) stretching parameter and the (b) relaxation time obtained from the stretched exponential fit of f_4 for different temperatures for the isothermal case (dark green squares), the squared (red circles) and trapezoidal (magenta triangle) heating shapes. To add more statistics, we run three independent simulations, all starting from the HQW. We also compare the isothermal simulations starting from the LDA (light green diamonds). (c) The ratio between the relaxation time obtained from diffusion calculations [196] and the relaxation times obtained from the stretched exponential fit of f_4.

5.3.5 The structural relaxation time depends on the initial configuration

We also follow the time evolution of f_4 when starting from the LDA initial sample for the isothermal case when $T_{max} = 220$ and 250 K. Compared to the τ_{rel} obtained when the HQW is isothermally heated, Fig. 5.6 b) shows that, τ_{rel} is smaller at $T_{max} = 220$ K when starting from the LDA, it is larger at $T_{max} = 250$ K. Fig. 5.6 a) indicates simple exponential relaxation kinetics with the stretching parameter being 1 for the LDA, and increasingly nonexponential relaxation is for the HQW as the temperature decreases. Thus, these observations are in good agreement with the experiment. [44] Comparing

these relaxation times from both HQW and LDA with the characteristic diffusion times for TIP4P/Ice [196], Fig. 5.6 c) shows that τ_{rel} is 1 to almost 2 orders of magnitude smaller than τ_{diff} for the lowest temperature, and τ_{rel} is approximately 1 order of magnitude larger at the highest temperature when starting from the LDA. Therefore, τ_{rel} does not correspond to the equilibrium relaxation rate, since the non-equilibrium relaxation time is always shorter than the equilibrium relaxation rate τ_{relax}^{non-eq} ¡ τ_{relax}^{diff}, when starting from the HQW.

5.4   Conclusions

In summary, using molecular dynamics simulations based on the TIP4P/Ice model we have investigated the core assumptions of the methodology of Kringle *et al.* which uses a nanosecond pulsed laser heating system to evolve amorphous solid water films to an equilibrated structure representative of supercooled water. In particular, we consider bulk water, and test both "square" pulses that heat and cool the sample instantaneously as well as "trapezoidal" pulses with cooling and heating ramps. From the structural analysis, we find that supercooled water can be equilibrated by heating pulses independently of the shape of the pulse. However, the structure measured at T_0 overestimates the tetrahedrality. Since the quenched structure is not representative of T_{max}, this can affect the interpretation of the results when extracting information from quenched configurations. We also find that the Widom temperature based on the analysis of the structure is quite sensitive to where the fraction of the low-temperature liquid is set to be zero. Furthermore, the structural relaxation time depends on the shape of the pulse, and also on the initial configurations, if it is either the low-density amorphous or hyperquenched water. Thus, the structural relaxation rates do not correspond to equilibrium relaxation rates, since the non-equilibrium relaxation time is always shorter than the equilibrium relaxation rate, when starting from the hyperquenched water sample.

Chapter 6

Conclusion and outlook

6.1 Conclusion

In this chapter, we summarize the main conclusions from the work presented in this Thesis.

In Chapter 2, the sliding process closely resembles that observed in viscoelastic substances. By contrasting two cases, one in which the GB interface features the presence of a liquid-like layer at 250 K and another in which there is not, at 150 K, we find that the liquid-like layer significantly facilitates GB sliding, acting as a boundary lubricant. Both the yield stress as well as the steady-state stress required to maintain sliding, which can be interpreted in terms of effective static and dynamic frictional forces, respectively, are significantly lower than those obtained at 150 K. Whereas in the latter case, the GB region undergoes large-scale amorphization in the frictional process; the thickness of the liquid-like layer at 250 K only increases moderately, reflecting its effectiveness in facilitating the sliding process. The present results provide valuable information regarding the viscous relaxation processes and the role of the disordered GB layer in the frictional behavior at the nanoscale during GB sliding in ice I_h.

In Chapter 3, the results show that the presence of the NaCl ions significantly affects both the structural and dynamical characteristics of the disordered layers at the GB regions. Compared to pristine ice samples, in addition to reducing the degree of water structure, the ions enhance the mobility of the water molecules in the GB region. Even so, the briny GB regions display quasi-liquid behavior in that the molecular diffusivities are

substantially lower than in the corresponding bulk liquid solutions at the same conditions of temperature, pressure and salinity. Finally, the presence of sodium chloride in the GB regions is found to facilitate the GB sliding process, which is consistent with experimental insight.

In Chapter 4, we show the existence of a distinct cross-over from Newtonian to non-Newtonian behavior characterized by a power-law shear-thinning regime. The viscosity reduction is due to the decrease in the connectivity of the hydrogen-bond network. Moreover, the shear thinning intensifies as the degree of supercooling increases, whereas the cross-over flow rate is approximately inversely proportional to the Newtonian viscosity. These results stimulate further investigation into possible fundamental relations between these nonequilibrium effects and the quasi-static Newtonian viscosity behavior of supercooled water.

In Chapter 5, we exhibit that supercooled water can be equilibrated by heating pulses independently of the shape of the pulse; however, the structure captured at the glassy state overestimates the tetrahedrality. Furthermore, we found that the structural relaxation time depends on the shape of the pulse, and also on the initial conditions. Our results represent a theoretical validation of the experimental procedure, and may give a better understanding of the kinetics and dynamics during the pulsed heating experiments.

6.2 Outlook

Despite these new contributions to the field of mechanical properties of ice I_h, there is still a lot to investigate. Theoretical investigations in this area of research are illuminating, as it is experimentally challenging to do *in situ* measurements at the internal interfaces of ice. Related to Chapters 2 and 3, the next step should include the sliding processes of more complex cases, such as triple junctions and polycristalline samples. Furthermore, it would be interesting to investigate the possible role of other different kind of ions and organics at these internal interfaces.

Regarding Chapter 4, further investigation into possible fundamental relations between these nonequilibrium effects and the quasi-static Newtonian viscosity behavior of supercooled water should be the next step. As it is difficult to perform any kind of measurement in supercooled water, it would be great to experimentally observe the shear-rate

dependence in the deeply supercooled liquid. Chapter 5 represents an example of how simulations can supplement the interpretation of the experimental results. The next step should seek to verify if the pulsed heating experiments is also a possible tool to explore strucural and relaxation properties of other systems than pristine water.

References

[1] W. S. Benedict and N. Gailar and Earle K. PlylerRotation-vibration spectra of deuterated water vapor. *The Journal of Chemical Physics* **24**, 1139–1165 (1956). (Cited on page 19.)

[2] Christoph G. SalzmannAdvances in the experimental exploration of water's phase diagram. *The Journal of Chemical Physics* **150**, 060901 (2019). (Cited on pages 9 and 20.)

[3] Prockter, Louise MIce in the solar system. *Johns Hopkins APL technical digest* **26**, 175–188 (2005). (Cited on page 21.)

[4] Pauling, LinusThe structure and entropy of ice and of other crystals with some randomness of atomic arrangement. *J. Am. Chem. Soc.* **57**, 2680–2684 (1935). (Cited on page 21.)

[5] Bernal, JD and Fowler, RHA theory of water and ionic solution, with particular reference to hydrogen and hydroxyl ions. *J. Chem. Phys.* **1**, 515–548 (1933). (Cited on page 21.)

[6] Creep (deformation) (2021). (Cited on pages 9 and 21.)

[7] Givetash, LindaPolar bears could disappear by 2100 due to melting ice, climate change, study says (2020). (Cited on pages 9 and 21.)

[8] Miller, Robert V and Whyte, Lyle *Polar Microbiology: Life in a Deep Freeze* (American Society for Microbiology Press, 2011). (Cited on pages 9 and 22.)

[9] Hondoh, T. and Higashi, A.X-ray diffraction topographic observations of the large-angle grain boundary in ice under deformation. *J. Glaciol.* **21**, 629–638 (1978). (Cited on pages 23, 36, and 38.)

[10] Hondoh, T. and Higashi, A.Anisotopy of migration and faceting of large-angle grain boundaries in ice bicrystals. *Philos. Mag. A* **39**, 137–149 (1979). (Cited on pages 23, 36, and 38.)

[11] Dash, J. G. and Rempel, A. W. and Wettlaufer, J. S.The physics of premelted ice and its geophysical consequences. *Rev. Mod. Phys.* **78**, 695–741 (2006). (Cited on pages 23, 35, 36, and 50.)

[12] Thomson, E. S. and Hansen-Goos, Hendrik and Wettlaufer, J. S. and Wilen, L. A.Grain boundary melting in ice. *J. Chem. Phys.* **138**, 124707 (2013). (Cited on pages 23, 36, 50, and 55.)

[13] Chen, Jialu and Maki, Takao and Nagashima, Ken and Murata, Ken-Ichiro and Sazaki, GenQuasi-liquid layers in grooves of grain boundaries and on grain surfaces of polycrystalline ice thin films. *Cryst. Growth Des.* (2020). (Cited on pages 23, 36, and 50.)

[14] Benatov, L. and Wettlaufer, J. S.Abrupt grain boundary melting in ice. *Phys. Rev. E* **70**, 061606– (2004). (Cited on pages 23, 36, and 50.)

[15] Thomson, E. S. and Benatov, L. and Wettlaufer, J. S.Erratum: Abrupt grain boundary melting in ice [phys. rev. e 70, 061606 (2004)]. *Phys. Rev. E* **82**, 039907– (2010). (Cited on pages 23, 36, and 50.)

[16] Moreira, Pedro Augusto Franco Pinheiro and de Aguiar Veiga, Roberto Gomes and de Almeida Ribeiro, Ingrid and Freitas, Rodrigo and Helfferich, Julian and de Koning, MauriceAnomalous diffusion of water molecules at grain boundaries in ice i h. *Phys. Chem. Chem. Phys.* **20**, 13944–13951 (2018). (Cited on pages 23, 36, 38, 50, 51, and 59.)

[17] Takuma Yagasaki and Masakazu Matsumoto and Hideki TanakaMolecular dynamics study of grain boundaries and triple junctions in ice. *The Journal of Chemical Physics* **153**, 124502 (2020). (Cited on pages 23, 36, 41, 50, 59, 83, and 84.)

[18] Bluhm, Hendrik and Ogletree, D Frank and Fadley, Charles S and Hussain, Zahid and Salmeron, MiquelThe premelting of ice studied with photoelectron spectroscopy. *J. Phys.: Condens. Matter* **14**, L227– (2002). (Cited on pages 9 and 23.)

[19] Frank J. Millero and Rainer Feistel and Daniel G. Wright and Trevor J. Mc-DougallThe composition of standard seawater and the definition of the reference-composition salinity scale. *Deep Sea Research Part I: Oceanographic Research Papers* **55**, 50–72 (2008). (Cited on pages 24 and 52.)

[20] V. F. Petrenko and R. W. Whitworth *Physics of ice* (Oxford University Press, New York, 1999). (Cited on pages 24, 35, 49, and 50.)

[21] Cho, H. and Shepson, P. B. and Barrie, L. A. and Cowin, J. P. and Zaveri, R.Nmr investigation of the quasi-brine layer in ice/brine mixtures. *The Journal of Physical Chemistry B* **106**, 11226–11232 (2002). (Cited on pages 24 and 50.)

[22] Ifigeneia Tsironi and Daniel Schlesinger and Alexander Spah and Lars Eriksson and Mo Segad and Fivos PerakisBrine rejection and hydrate formation upon freezing of NaCl aqueous solutions. *Physical Chemistry Chemical Physics* **22**, 7625–7632 (2020). (Cited on pages 9, 24, 49, and 53.)

[23] Gallo, Paola and Amann-Winkel, Katrin and Angell, Charles Austen and Anisimov, Mikhail Alexeevich and Caupin, Frédéric and Chakravarty, Charusita and Lascaris, Erik and Loerting, Thomas and Panagiotopoulos, Athanassios Zois and Russo, John and Sellberg, Jonas Alexander and Stanley, Harry Eugene and Tanaka, Hajime and Vega, Carlos and Xu, Limei and Pettersson, Lars Gunnar MoodyWater: A tale of two liquids. *Chem. Rev.* **116**, 7463–7500 (2016). (Cited on pages 9, 25, 26, 50, 68, and 79.)

[24] Martin ChaplinForty-one anomalies of water. (Cited on page 25.)

[25] Martin GoldsteinViscous liquids and the glass transition: A potential energy barrier picture. *The Journal of Chemical Physics* **51**, 3728–3739 (1969). (Cited on page 26.)

[26] Stillinger, Frank H.A topographic view of supercooled liquids and glass formation. *Science* **267**, 1935– (1995). (Cited on page 26.)

[27] Stillinger, F.H. *Energy Landscapes, Inherent Structures, and Condensed-Matter Phenomena* (Princeton University Press, 2015). (Cited on page 26.)

[28] Andrea CavagnaSupercooled liquids for pedestrians. *Physics Reports* **476**, 51–124 (2009). (Cited on page 26.)

[29] C. A. AngellFormation of glasses from liquids and biopolymers. *Science* **267**, 1924–1935 (1995). (Cited on page 27.)

[30] Dehaoui, Amine and Issenmann, Bruno and Caupin, FrédéricViscosity of deeply supercooled water and its coupling to molecular diffusion. *Proc Natl Acad Sci USA* **112**, 12020 (2015). (Cited on pages 9, 27, 68, and 69.)

[31] Lakes, Roderic S *Viscoelastic Materials* (Cambridge University Press, 2009). (Cited on pages 27 and 68.)

[32] Krishnan, J Murali and Deshpande, Abhijit P and Kumar, PB Sunil *Rheology of complex fluids* (Springer, 2010). (Cited on pages 27 and 68.)

[33] Khatibi, Milad and Time, Rune W. and Shaibu, RashidDynamical feature of particle dunes in newtonian and shear-thinning flows: Relevance to hole-cleaning in pipe and annulus. *International Journal of Multiphase Flow* **99**, 284–293 (2018). (Cited on pages 27 and 69.)

[34] Poole, Peter H. and Sciortino, Francesco and Essmann, Ulrich and Stanley, H. EugenePhase behaviour of metastable water. *Nature* **360**, 324–328 (1992). (Cited on page 28.)

[35] Sastry, S. and Debenedetti, P. G. and Sciortino, F. and Stanley, H. E.Singularity-free interpretation of the thermodynamics of supercooled water. *Phys. Rev. E* **53**, 6144–6154 (1996). (Cited on page 28.)

[36] Robin J. SpeedyStability-limit conjecture. an interpretation of the properties of water. *The Journal of Physical Chemistry* **86**, 982–991 (1982). (Cited on page 28.)

[37] Eli Shiratani and Masaki SasaiMolecular scale precursor of the liquid–liquid phase transition of water. *The Journal of Chemical Physics* **108**, 3264–3276 (1998). (Cited on pages 28 and 76.)

[38] Emily B. Moore and Valeria MolineroGrowing correlation length in supercooled water. *The Journal of Chemical Physics* **130**, 244505 (2009). (Cited on pages 28, 76, 77, and 80.)

[39] K. T. Wikfeldt and A. Nilsson and L. G. M. PetterssonSpatially inhomogeneous bimodal inherent structure of simulated liquid water. *Physical Chemistry Chemical Physics* **13**, 19918 (2011). (Cited on pages 28, 76, and 79.)

[40] Megan J. Cuthbertson and Peter H. PooleMixturelike behavior near a liquid-liquid phase transition in simulations of supercooled water. *Physical Review Letters* **106**, 115706 (2011). (Cited on pages 28 and 76.)

[41] John Russo and Hajime TanakaUnderstanding water's anomalies with locally favoured structures. *Nature Communications* **5** (2014). (Cited on pages 28, 76, and 77.)

[42] Shinji Saito and Biman Bagchi and Iwao OhmineCrucial role of fragmented and isolated defects in persistent relaxation of deeply supercooled water. *The Journal of Chemical Physics* **149**, 124504 (2018). (Cited on pages 28 and 76.)

[43] Loni Kringle and Wyatt A. Thornley and Bruce D. Kay and Greg A. KimmelReversible structural transformations in supercooled liquid water from 135 to 245 k. *Science* **369**, 1490–1492 (2020). (Cited on pages 10, 28, 29, 76, 77, 78, 81, 84, and 85.)

[44] Loni Kringle and Wyatt A. Thornley and Bruce D. Kay and Greg A. Kimmel-Structural relaxation and crystallization in supercooled water from 170 to 260 k. *Proceedings of the National Academy of Sciences* **118**, e2022884118 (2021). (Cited on pages 28, 76, 77, 78, 83, 84, 86, and 88.)

[45] Sellberg, J. A. and Huang, C. and McQueen, T. A. and Loh, N. D. and Laksmono, H. and Schlesinger, D. and Sierra, R. G. and Nordlund, D. and Hampton, C. Y. and Starodub, D. and DePonte, D. P. and Beye, M. and Chen, C. and Martin, A. V. and Barty, A. and Wikfeldt, K. T. and Weiss, T. M. and Caronna, C. and Feldkamp, J. and Skinner, L. B. and Seibert, M. M. and Messerschmidt, M. and Williams, G. J. and Boutet, S. and Pettersson, L. G. M. and Bogan, M. J. and Nilsson, A.Ultrafast x-ray probing of water structure below the homogeneous ice nucleation temperature. *Nature* **510**, 381–384 (2014). (Cited on pages 28 and 76.)

[46] Kim, Kyung Hwan and Späh, Alexander and Pathak, Harshad and Perakis, Fivos and Mariedahl, Daniel and Amann-Winkel, Katrin and Sellberg, Jonas A. and Lee, Jae Hyuk and Kim, Sangsoo and Park, Jaehyun and Nam, Ki Hyun and Katayama, Tetsuo and Nilsson, AndersMaxima in the thermodynamic response and correlation functions of deeply supercooled water. *Science* **358**, 1589– (2017). (Cited on pages 28, 76, and 77.)

[47] Kyung Hwan Kim and Alexander Späh and Harshad Pathak and Fivos Perakis and Daniel Mariedahl and Katrin Amann-Winkel and Jonas A. Sellberg and Jae Hyuk Lee and Sangsoo Kim and Jaehyun Park and Ki Hyun Nam and Tetsuo Katayama and Anders NilssonMaxima in the thermodynamic response and correla-

tion functions of deeply supercooled water. *Science* **358**, 1589–1593 (2017). (Cited on pages 28, 76, and 85.)

[48] Kyung Hwan Kim and Katrin Amann-Winkel and Nicolas Giovambattista and Alexander Späh and Fivos Perakis and Harshad Pathak and Marjorie Ladd Parada and Cheolhee Yang and Daniel Mariedahl and Tobias Eklund and Thomas. J. Lane and Seonju You and Sangmin Jeong and Matthew Weston and Jae Hyuk Lee and Intae Eom and Minseok Kim and Jaeku Park and Sae Hwan Chun and Peter H. Poole and Anders NilssonExperimental observation of the liquid-liquid transition in bulk supercooled water under pressure. *Science* **370**, 978–982 (2020). (Cited on pages 28 and 76.)

[49] M. P. Allen and D. J. Tildesley *Computer Simulation of Liquids* (Oxford University Press, 1987). (Cited on page 30.)

[50] Frenkel, Daan and Smit, Berend *Understanding Molecular Simulation* (Academic Press, San Diego, San Diego, 2002). (Cited on page 30.)

[51] Efrem Braun and Justin Gilmer and Heather B. Mayes and David L. Mobley and Jacob I. Monroe and Samarjeet Prasad and Daniel M. ZuckermanBest practices for foundations in molecular simulations [article v1.0]. *Living Journal of Computational Molecular Science* **1** (2019). (Cited on page 30.)

[52] Philippe H. HünenbergerThermostat algorithms for molecular dynamics simulations. In *Advanced Computer Simulation*, 105–149 (Springer Berlin Heidelberg, 2005). (Cited on page 30.)

[53] Schneider, T. and Stoll, E.Molecular-dynamics study of a three-dimensional one-component model for distortive phase transitions. *Phys. Rev. B* **17**, 1302–1322 (1978). (Cited on pages 30, 39, 52, and 69.)

[54] Hans C. AndersenMolecular dynamics simulations at constant pressure and/or temperature. *The Journal of Chemical Physics* **72**, 2384–2393 (1980). (Cited on page 31.)

[55] Parrinello, M. and Rahman, A.Polymorphic transitions in single crystals: A new molecular dynamics method. *J. Appl. Phys.* **52**, 7182–7190 (1981). (Cited on pages 32, 39, and 52.)

[56] Hockney, R. W. *Computer Simulation Using Particles* (Taylor & Francis Group, 2017). (Cited on pages 32, 39, 52, 69, and 78.)

[57] Plimpton, SteveFast parallel algorithms for short-range molecular dynamics. *J. Comput. Phys.* **117**, 1–19 (1995). (Cited on pages 32, 38, 52, 69, and 78.)

[58] Berendsen, H. J. C. and Grigera, J. R. and Straatsma, T. P.The missing term in effective pair potentials. *J. Phys. Chem.* **91**, 6269–6271 (1987). (Cited on page 32.)

[59] Jorgensen, William L. and Madura, Jeffry D.Temperature and size dependence for monte carlo simulations of tip4p water. *Mol. Phys.* **56**, 1381–1392 (1985). (Cited on page 32.)

[60] Molinero, Valeria and Moore, Emily B.Water modeled as an intermediate element between carbon and silicon. *J. Phys. Chem. B* **113**, 4008–4016 (2009). (Cited on pages 32 and 38.)

[61] Abascal, J. L. F. and Sanz, E. and García Fernández, R. and Vega, C.A potential model for the study of ices and amorphous water: Tip4p/ice. *J. Chem. Phys.* **122**, 234511 (2005). (Cited on pages 32, 38, 69, 77, 78, and 79.)

[62] Abascal, J. L. F. and Vega, C.A general purpose model for the condensed phases of water: Tip4p/2005. *J. Chem. Phys.* **123**, 234505 (2005). (Cited on pages 32 and 51.)

[63] Mahoney, Michael W. and Jorgensen, William L.A five-site model for liquid water and the reproduction of the density anomaly by rigid, nonpolarizable potential functions. *J. Chem. Phys.* **112**, 8910–8922 (2000). (Cited on page 32.)

[64] Ryckaert, Jean-Paul and Ciccotti, Giovanni and Berendsen, Herman J.CNumerical integration of the cartesian equations of motion of a system with constraints: molecular dynamics of n-alkanes. *J. Comput. Phys.* **23**, 327–341 (1977). (Cited on pages 32, 39, 52, 69, and 78.)

[65] McBride , CarlTip4q model of water. (Cited on pages 10 and 33.)

[66] FaradayXXIV. on regelation, and on the conservation of force. *Philos. Mag., Ser. 4* **17**, 162–169 (1859). (Cited on page 35.)

[67] Faraday, MichaelI. note on regelation. *Proceedings of the Royal Society of London* **10**, 440–450 (1860). (Cited on page 35.)

[68] Nojima, Yuki and Shioya, Yuki and Torii, Hajime and Yamaguchi, ShoichiHydrogen order at the surface of ice ih revealed by vibrational spectroscopy. *Chem. Commun.* **56**, 4563–4566 (2020). (Cited on page 35.)

[69] Kato, Fumiaki and Sugimoto, Toshiki and Matsumoto, YoshiyasuDirect experimental evidence for markedly enhanced surface proton activity inherent to water ice. *J. Phys. Chem. Lett.* **11**, 2524–2529 (2020). (Cited on page 35.)

[70] Llombart, Pablo and Noya, Eva G. and Sibley, David N. and Archer, Andrew J. and MacDowell, Luis G.Rounded layering transitions on the surface of ice. *Phys. Rev. Lett.* **124**, 065702 (2020). (Cited on page 35.)

[71] Llombart, Pablo and Noya, Eva G. and MacDowell, Luis G.Surface phase transitions and crystal habits of ice in the atmosphere. *Sci Adv* **6**, 9322 (2020). (Cited on pages 35 and 56.)

[72] Hudait, Arpa and Moberg, Daniel R. and Qiu, Yuqing and Odendahl, Nathan and Paesani, Francesco and Molinero, ValeriaPreordering of water is not needed for ice recognition by hyperactive antifreeze proteins. *Proc Natl Acad Sci USA* **115**, 8266 (2018). (Cited on page 35.)

[73] Mochizuki, Kenji and Molinero, ValeriaAntifreeze glycoproteins bind reversibly to ice via hydrophobic groups. *J. Am. Chem. Soc.* **140**, 4803–4811 (2018). (Cited on page 35.)

[74] Dash, J G and Fu, Haiying and Wettlaufer, J SThe premelting of ice and its environmental consequences. *Rep. Prog. Phys.* **58**, 115– (1995). (Cited on page 35.)

[75] Qiu, Yuqing and Molinero, ValeriaWhy is it so difficult to identify the onset of ice premelting? *J. Phys. Chem. Lett.* **9**, 5179–5182 (2018). (Cited on page 35.)

[76] Slater, Ben and Michaelides, AngelosSurface premelting of water ice. *Nat. Rev. Chem.* **3**, 172–188 (2019). (Cited on page 35.)

[77] Kling, Tanja and Kling, Felix and Donadio, DavideStructure and dynamics of the quasi-liquid layer at the surface of ice from molecular simulations. *J. Phys. Chem. C* **122**, 24780–24787 (2018). (Cited on pages 35 and 61.)

[78] R. RosenbergWhy is ice slippery. *Phys. Today* **58**, 50 (2005). (Cited on page 35.)

[79] Oosterkamp, T. H. and Boudewijn, T. and van Leeuwen, J. M. J.Skating on slippery ice. *Europhysics News* **50**, 28–32 (2019). (Cited on page 35.)

[80] Kietzig, Anne-Marie and Hatzikiriakos, Savvas G. and Englezos, PeterIce friction: The effects of surface roughness, structure, and hydrophobicity. *Journal of Applied Physics* **106**, 024303 (2009). (Cited on page 36.)

[81] Anne-Marie Kietzig and Savvas G. Hatzikiriakos and Peter EnglezosPhysics of ice friction. *Journal of Applied Physics* **107**, 081101 (2010). (Cited on page 36.)

[82] Persson, B. N. J.Ice friction: Role of non-uniform frictional heating and ice pre-melting. *J. Chem. Phys.* **143**, 224701 (2015). (Cited on page 36.)

[83] Canale, L and Comtet, J and Niguès, A and Cohen, C and Clanet, C and Siria, A and Bocquet, LNanorheology of interfacial water during ice gliding. *Physical Review X* **9**, 041025 (2019). (Cited on page 36.)

[84] Louden, Patrick B. and Gezelter, J. DanielWhy is ice slippery? simulations of shear viscosity of the quasi-liquid layer on ice. *J. Phys. Chem. Lett.* **9**, 3686–3691 (2018). (Cited on pages 36 and 61.)

[85] Bollmann, W. *Crystal Defects and Crystalline Interfaces* (Springer-Verlag, 1970). (Cited on page 36.)

[86] Sutton, A.P. and Balluffi, R.W. *Interfaces in crystalline materials* (Clarendon Press, 1995). (Cited on pages 36 and 50.)

[87] Maurice de KoningCrystal imperfections in ice ih. *J. Chem. Phys.* **153**, 110902 (2020). (Cited on pages 36 and 50.)

[88] Langdon, Terence G.Grain boundary sliding revisited: Developments in sliding over four decades. *J. Mater. Sci.* **41**, 597–609 (2006). (Cited on page 36.)

[89] Paterson, W. S. B. *The Physics of Glaciers* (Elsevier Science, 2016). (Cited on page 36.)

[90] Weiss, J. and Schulson, E. M.Grain-boundary sliding and crack nucleation in ice. *Philos. Mag. A* **80**, 279–300 (2000). (Cited on page 36.)

[91] Tatibouet, J. and Perez, J. and Vassouille, R.Study of grain boundaries in ice by internal friction measurement. *J. Phys. Colloques* **48**, C1–197–C1–203 (1987). (Cited on page 36.)

[92] Zepeda-Ruiz, Luis A. and Stukowski, Alexander and Oppelstrup, Tomas and Bulatov, Vasily V.Probing the limits of metal plasticity with molecular dynamics simulations. *Nature* **550**, 492 (2017). (Cited on page 36.)

[93] Zepeda-Ruiz, Luis A. and Stukowski, Alexander and Oppelstrup, Tomas and Bertin, Nicolas and Barton, Nathan R. and Freitas, Rodrigo and Bulatov, Vasily V.Atomistic insights into metal hardening. *Nat. Mater.* (2020). (Cited on page 36.)

[94] Cao, Pinqiang and Wu, Jianyang and Zhang, Zhisen and Fang, Bin and Peng, Li and Li, Tianshu and Vlugt, Thijs J. H. and Ning, FulongMechanical properties of bi- and poly-crystalline ice. *AIP Advances* **8**, 125108 (2018). (Cited on pages 36 and 38.)

[95] Gonzalez Kriegel, B. J. and Di Prinzio, C. L. and Nasello, O. B.Exact coincidence site lattice in ice ih. *J. Phys. Chem. B* **101**, 6243–6246 (1997). (Cited on page 38.)

[96] Kwok, Thomas and Ho, P. S. and Yip, Sidney and Balluffi, R. W. and Bristowe, P. D. and Brokman, A.Evidence for vacancy mechanism in grain boundary diffusion in bcc iron: A molecular-dynamics study. *Phys. Rev. Lett.* **47**, 1148–1151 (1981). (Cited on page 38.)

[97] Bishop,George   H.   and   Harrison,Ralph   J.   and   Kwok,Thomas   and Yip,SidneyComputer molecular dynamics simulation studies of grain-boundary structures. ii. migration, sliding, and annihilation in a two-dimensional solid. *J. Appl. Phys.* **53**, 5609–5616 (1982). (Cited on page 38.)

[98] Bishop,George   H.   and   Harrison,Ralph   J.   and   Kwok,Thomas   and Yip,SidneyComputer molecular-dynamics studies of grain-boundary structures. i. observations of coupled sliding and migration in a three-dimensional simulation. *J. Appl. Phys.* **53**, 5596–5608 (1982). (Cited on page 38.)

[99] Maras, E. and Trushin, O. and Stukowski, A. and Ala-Nissila, T. and Jönsson, H.Global transition path search for dislocation formation in ge on si(001). *Comput. Phys. Commun.* **205**, 13–21 (2016). (Cited on pages 38 and 53.)

[100] Stukowski, AlexanderVisualization and analysis of atomistic simulation data with ovito: the open visualization tool. *Model. Simul. Mater. Sci. Eng.* **18**, 015012– (2010). (Cited on pages 10, 38, 40, 53, and 78.)

[101] Haji-Akbari, Amir and Debenedetti, Pablo G.Direct calculation of ice homogeneous nucleation rate for a molecular model of water. *Proc Natl Acad Sci USA* **112**, 10582– (2015). (Cited on page 38.)

[102] Debenedetti, Pablo G. and Sciortino, Francesco and Zerze, Gül H.Second critical point in two realistic models of water. *Science* **369**, 289 (2020). (Cited on pages 38, 79, and 83.)

[103] Conde, M. M. and Vega, C. and Patrykiejew, A.The thickness of a liquid layer on the free surface of ice as obtained from computer simulation. *J. Chem. Phys.* **129**, 014702 (2008). (Cited on pages 38 and 79.)

[104] Pedro Antonio Santos-Flórez and Carlos J. Ruestes and Maurice de KoningAtomistic simulation of nanoindentation of ice ih. *J. Phys. Chem. C* **124**, 9329–9336 (2020). (Cited on pages 38 and 53.)

[105] Chan, Henry and Cherukara, Mathew J. and Narayanan, Badri and Loeffler, Troy D. and Benmore, Chris and Gray, Stephen K. and Sankaranarayanan, Subramanian K. R. S.Machine learning coarse grained models for water. *Nat. Commun.* **10**, 379 (2019). (Cited on page 38.)

[106] Santos-Flórez, Pedro Antonio and Ruestes, Carlos J. and de Koning, MauriceUniaxial-deformation behavior of ice ih as described by the tip4p/ice and mw water models. *J. Chem. Phys.* **149**, 164711 (2018). (Cited on page 38.)

[107] Martyna, Glenn J. and Tobias, Douglas J. and Klein, Michael L.Constant pressure molecular dynamics algorithms. *J. Chem. Phys.* **101**, 4177–4189 (1994). (Cited on pages 39 and 52.)

[108] Shinoda, Wataru and Shiga, Motoyuki and Mikami, MasuhiroRapid estimation of elastic constants by molecular dynamics simulation under constant stress. *Phys. Rev. B* **69**, 134103– (2004). (Cited on pages 39, 52, and 69.)

[109] McQuarrie, D.A. *Statistical Mechanics* (University Science Books, 2000). (Cited on pages 40, 63, and 72.)

[110] Stukowski, AlexanderComputational analysis methods in atomistic modeling of crystals. *JOM* **66**, 399–407 (2014). (Cited on pages 10, 12, 40, 54, and 56.)

[111] Osaki, K. and Inoue, T. and Isomura, T.Stress overshoot of polymer solutions at high rates of shear. *J. Polym. Sci. B Polym. Phys.* **38**, 1917–1925 (2000). (Cited on pages 41, 64, and 70.)

[112] Islam, Mohammad T. and Archer, Lynden A.Nonlinear rheology of highly entangled polymer solutions in start-up and steady shear flow. *J. Polym. Sci. B Polym. Phys.* **39**, 2275–2289 (2001). (Cited on pages 41, 64, and 70.)

[113] Letwimolnun, W. and Vergnes, B. and Ausias, G. and Carreau, P. J.Stress overshoots of organoclay nanocomposites in transient shear flow. *Journal of Non-Newtonian Fluid Mechanics* **141**, 167–179 (2007). (Cited on pages 41, 64, and 70.)

[114] Varnik, F. and Bocquet, L. and Barrat, J.-L.A study of the static yield stress in a binary lennard-jones glass. *J. Chem. Phys.* **120**, 2788–2801 (2004). (Cited on pages 41, 64, and 70.)

[115] Zausch, J. and Horbach, J. and Laurati, M. and Egelhaaf, S. U. and Brader, J. M. and Voigtmann, Th and Fuchs, M.From equilibrium to steady state: the transient dynamics of colloidal liquids under shear **20**, 404210 (2008). (Cited on pages 41, 64, and 70.)

[116] Zausch, J. and Horbach, J.The build-up and relaxation of stresses in a glass-forming soft-sphere mixture under shear: A computer simulation study **88**, 60001 (2009). (Cited on pages 41, 64, and 70.)

[117] Fuereder, Ingo and Ilg, PatrickTransient inhomogeneous flow patterns in supercooled liquids under shear. *Soft Matter* **13**, 2192–2200 (2017). (Cited on pages 41, 64, and 70.)

[118] Zaccone, A. and Schall, P. and Terentjev, E. M.Microscopic origin of nonlinear nonaffine deformation in bulk metallic glasses. *Phys. Rev. B* **90**, 140203 (2014). (Cited on pages 41 and 64.)

[119] M. Laurati and P. Maßhoff and K. J. Mutch and S. U. Egelhaaf and A. ZacconeLong-lived neighbors determine the rheological response of glasses. *Physical Review Letters* **118**, 018002 (2017). (Cited on pages 41 and 64.)

[120] Ingrid de Almeida Ribeiro and Maurice de KoningNon-newtonian flow effects in supercooled water. *Phys. Rev. Res.* **2**, 022004(R) (2020). (Cited on pages 41 and 64.)

[121] Bhushan, Bharat *Nanotribology and nanomechanics: an introduction* (Springer Science & Business Media, 2008). (Cited on page 45.)

[122] K Furić and I Ciglenečki and B ĆosovićRaman spectroscopic study of sodium chloride water solutions. *Journal of Molecular Structure* **550-551**, 225–234 (2000). (Cited on page 49.)

[123] R. Mancinelli and A. Botti and F. Bruni and M. A. Ricci and A. K. SoperPerturbation of water structure due to monovalent ions in solution. *Physical Chemistry Chemical Physics* **9**, 2959 (2007). (Cited on pages 49 and 57.)

[124] Mostafa H. Sharqawy and John H. Lienhard and Syed M. ZubairThermophysical properties of seawater: a review of existing correlations and data. *Desalination and Water Treatment* **16**, 354–380 (2010). (Cited on page 49.)

[125] Alex P. Gaiduk and Giulia GalliLocal and global effects of dissolved sodium chloride on the structure of water. *The Journal of Physical Chemistry Letters* **8**, 1496–1502 (2017). (Cited on page 49.)

[126] I. M. Zeron and J. L. F. Abascal and C. VegaA force field of li$^+$, na$^+$, k$^+$, mg^{2+}, ca^{2+}, cl$^-$, and so$_4^{2-}$ in aqueous solution based on the TIP4p/2005 water model and scaled charges for the ions. *The Journal of Chemical Physics* **151**, 134504 (2019). (Cited on pages 49 and 51.)

[127] Damien Laage and Guillaume StirnemannEffect of ions on water dynamics in dilute and concentrated aqueous salt solutions. *The Journal of Physical Chemistry B* **123**, 3312–3324 (2019). (Cited on page 49.)

[128] Luboš Vrbka and Pavel JungwirthBrine rejection from freezing salt solutions: A molecular dynamics study. *Phys. Rev. Lett.* **95**, 148501 (2005). (Cited on pages 49 and 53.)

[129] M. M. Conde and M. Rovere and P. GalloSpontaneous NaCl-doped ice at seawater conditions: focus on the mechanisms of ion inclusion. *Physical Chemistry Chemical Physics* **19**, 9566–9574 (2017). (Cited on pages 49, 51, 53, and 59.)

[130] Samuel P. Niblett and David T. LimmerIon dissociation dynamics in an aqueous premelting layer. *The Journal of Physical Chemistry B* **125**, 2174–2181 (2021). (Cited on page 49.)

[131] Pitter, Richard L. and Finnegan, William G.An experimental study of effects of soluble salt impurities on ice crystal processes during growth. *Atmos. Res.* **25**, 71–88 (1990). (Cited on page 49.)

[132] Wagner, Robert and Möhler, OttmarHeterogeneous ice nucleation ability of crystalline sodium chloride dihydrate particles. *J. Geophys. Res. Atmos.* **118**, 4610–4622 (2013). (Cited on page 49.)

[133] N. W. Riley and G. Noll and J. W. GlenThe creep of NaCl-doped ice monocrystals. *Journal of Glaciology* **21**, 501–507 (1978). (Cited on page 49.)

[134] K. M. Cuffey and H. Conway and A. Gades and B. Hallet and C. F. Raymond and S. WhitlowDeformation properties of subfreezing glacier ice: Role of crystal size, chemical impurities, and rock particles inferred from in situ measurements. *Journal of Geophysical Research: Solid Earth* **105**, 27895–27915 (2000). (Cited on page 49.)

[135] Drebushchak, V. A. and Drebushchak, T. N. and Ogienko, A. G. and Yunoshev, A. S.Crystallization of sodium chloride dihydrate (hydrohalite). *J. Cryst. Growth* **517**, 17–23 (2019). (Cited on page 50.)

[136] Masaaki Wakatsuchi and Toshiyuki KawamuraFormation processes of brine drainage channels in sea ice. *Journal of Geophysical Research* **92**, 7195 (1987). (Cited on page 50.)

[137] Toshiyuki KawamuraObservations of the internal structure of sea ice by x ray computed tomography. *Journal of Geophysical Research* **93**, 2343 (1988). (Cited on page 50.)

[138] D. Cullen and I. BakerThe chemistry of grain boundaries in greenland ice. *Journal of Glaciology* **46**, 703–706 (2000). (Cited on page 50.)

[139] D. Cullen and I. BakerObservation of impurities in ice. *Microscopy Research and Technique* **55**, 198–207 (2001). (Cited on page 50.)

[140] I Baker and D Cullen and D IliescuThe microstructural location of impurities in ice. *Canadian Journal of Physics* **81**, 1–9 (2003). (Cited on page 50.)

[141] Piers R.F. Barnes and Eric W. Wolff and David C. Mallard and Heidy M. MaderSEM studies of the morphology and chemistry of polar ice. *Microscopy Research and Technique* **62**, 62–69 (2003). (Cited on page 50.)

[142] J R Blackford and C E Jeffree and D F J Noake and B A MarmoMicrostructural evolution in sintered ice particles containing NaCl observed by low-temperature

scanning electron microscope. *Proceedings of the Institution of Mechanical Engineers, Part L: Journal of Materials: Design and Applications* **221**, 151–156 (2007). (Cited on page 50.)

[143] Ingrid de Almeida Ribeiro and Maurice de KoningGrain-boundary sliding in ice ih: Tribology and rheology at the nanoscale. *The Journal of Physical Chemistry C* **125**, 627–634 (2021). (Cited on pages 50, 51, 53, and 62.)

[144] Thangswamy, Muthulakshmi and Maheshwari, Priya and Dutta, Dhanadeep and Rane, Vinayak and Pujari, Pradeep K.Epr evidence of liquid water in ice: An intrinsic property of water or a self-confinement effect? *J. Phys. Chem. A* **122**, 5177–5189 (2018). (Cited on page 50.)

[145] Imrichová, Kamila and Veselý, Lukáš and Gasser, Tobias M. and Loerting, Thomas and Neděla, Vilém and Heger, DominikVitrification and increase of basicity in between ice ih crystals in rapidly frozen dilute nacl aqueous solutions. *J. Chem. Phys.* **151**, 014503 (2019). (Cited on page 50.)

[146] Vega, Carlos and Abascal, Jose L. F.Simulating water with rigid non-polarizable models: a general perspective. *Phys. Chem. Chem. Phys.* **13**, 19663–19688 (2011). (Cited on page 51.)

[147] A. L. Benavides and M. A. Portillo and V. C. Chamorro and J. R. Espinosa and J. L. F. Abascal and C. VegaA potential model for sodium chloride solutions based on the TIP4p/2005 water model. *The Journal of Chemical Physics* **147**, 104501 (2017). (Cited on pages 51 and 62.)

[148] Igor Leontyev and Alexei StuchebrukhovAccounting for electronic polarization in non-polarizable force fields. *Physical Chemistry Chemical Physics* **13**, 2613 (2011). (Cited on page 51.)

[149] Ivan M. Zeron and Miguel A. Gonzalez and Edoardo Errani and Carlos Vega and Jose L. F. Abascal"in silico" seawater. *Journal of Chemical Theory and Computation* **17**, 1715–1725 (2021). (Cited on page 51.)

[150] M. M. Conde and M. Rovere and P. GalloHigh precision determination of the melting points of water tip4p/2005 and water tip4p/ice models by the direct coexistence technique. *The Journal of Chemical Physics* **147**, 244506 (2017). (Cited on page 52.)

[151] Carlos Vega and Maria Martin-Conde and Andrzej PatrykiejewAbsence of super-heating for ice i$_h$ with a free surface: a new method of determining the melting point of different water models. *Molecular Physics* **104**, 3583–3592 (2006). (Cited on page 52.)

[152] García Fernández, Ramón and Abascal, José L. F. and Vega, CarlosThe melting point of ice ih for common water models calculated from direct coexistence of the solid-liquid interface. *J. Chem. Phys.* **124**, 144506 (2006). (Cited on page 52.)

[153] Vega, C. and Sanz, E. and Abascal, J. L. F.The melting temperature of the most common models of water. *J. Chem. Phys.* **122**, 114507 (2005). (Cited on page 52.)

[154] Hudait, Arpa and Allen, Michael T. and Molinero, ValeriaSink or swim: Ions and organics at the ice-air interface. *J. Am. Chem. Soc.* **139**, 10095–10103 (2017). (Cited on page 56.)

[155] Robert C. DeMille and Valeria MolineroCoarse-grained ions without charges: Reproducing the solvation structure of NaCl in water using short-ranged potentials. *The Journal of Chemical Physics* **131**, 034107 (2009). (Cited on page 57.)

[156] Pinheiro Moreira, Pedro Augusto Franco and de Koning, MauriceTrapping of hydrochloric and hydrofluoric acid at vacancies on and underneath the ice ih basal-plane surface. *J. Phys. Chem. A* **117**, 11066–11071 (2013). (Cited on page 59.)

[157] Clark, J.Solid-liquid phase diagrams: Salt solution. (Cited on page 59.)

[158] Washburn, E. W. *International Critical Tables of Numerical Data, Physics, Chemistry and Technology (1st Electronic Edition)* (Knovel, 2003). (Cited on page 59.)

[159] Weeks, W. F.Tensile strength of nacl ice. *J. Glaciol.* **4**, 25–52 (1962). (Cited on page 65.)

[160] Angell, C. A.Supercooled water. *Annu. Rev. Phys. Chem.* **34**, 593–630 (1983). (Cited on page 68.)

[161] Cerdeiriña, Claudio A. and Troncoso, Jacobo and González-Salgado, Diego and Debenedetti, Pablo G. and Stanley, H. EugeneWater's two-critical-point scenario in the ising paradigm. *J. Chem. Phys.* **150**, 244509 (2019). (Cited on page 68.)

[162] Hestand, Nicholas J. and Skinner, J. L.Perspective: Crossing the widom line in no man's land: Experiments, simulations, and the location of the liquid-liquid critical point in supercooled water. *J. Chem. Phys.* **149**, 140901 (2018). (Cited on page 68.)

[163] Naserifar, Saber and Goddard, William A.Anomalies in supercooled water at $\sim$ 230 k arise from a 1d polymer to 2d network topological transformation. *J. Phys. Chem. Lett.* **10**, 6267–6273 (2019). (Cited on page 68.)

[164] Limmer, David T. and Chandler, DavidThe putative liquid-liquid transition is a liquid-solid transition in atomistic models of water. *J. Chem. Phys.* **135**, 134503–10 (2011). (Cited on page 68.)

[165] Limmer, David T. and Chandler, DavidThe putative liquid-liquid transition is a liquid-solid transition in atomistic models of water. ii. *J. Chem. Phys.* **138**, 214504–15 (2013). (Cited on page 68.)

[166] Palmer, Jeremy C. and Haji-Akbari, Amir and Singh, Rakesh S. and Martelli, Fausto and Car, Roberto and Panagiotopoulos, Athanassios Z. and Debenedetti, Pablo G.Comment on "the putative liquid-liquid transition is a liquid-solid transition in atomistic models of water" [i and ii: J. chem. phys. 135, 134503 (2011); j. chem. phys. 138, 214504 (2013)]. *J. Chem. Phys.* **148**, 137101 (2018). (Cited on page 68.)

[167] Ito, Kaori and Moynihan, Cornelius T. and Angell, C. AustenThermodynamic determination of fragility in liquids and a fragile-to-strong liquid transition in water. *Nature* **398**, 492–495 (1999). (Cited on page 68.)

[168] Shi, Rui and Russo, John and Tanaka, HajimeOrigin of the emergent fragile-to-strong transition in supercooled water. *Proc Natl Acad Sci USA* **115**, 9444 (2018). (Cited on page 68.)

[169] Singh, Lokendra P. and Issenmann, Bruno and Caupin, FrédéricPressure dependence of viscosity in supercooled water and a unified approach for thermodynamic and dynamic anomalies of water. *Proc Natl Acad Sci USA* **114**, 4312 (2017). (Cited on page 68.)

[170] Larson, Ronald G *The structure and rheology of complex fluids*, vol. 150 (Oxford university press New York, 1999). (Cited on page 68.)

[171] Hallett, J.The temperature dependence of the viscosity of supercooled water **82**, 1046–1050 (1963). (Cited on page 69.)

[172] Amir Haji-Akbari and Pablo G. DebenedettiComputational investigation of surface freezing in a molecular model of water. *Proceedings of the National Academy of Sciences* **114**, 3316–3321 (2017). (Cited on page 69.)

[173] Katsumi Hagita and Takahiro Murashima and Hiroshi Takano and Toshihiro KawakatsuThinning approximation for two-dimensional scattering patterns from coarse-grained polymer melts under shear flow. *Journal of the Physical Society of Japan* **86**, 124803 (2017). (Cited on page 69.)

[174] Carreau, Pierre J.Rheological equations from molecular network theories. *Transactions of the Society of Rheology* **16**, 99–127 (1972). (Cited on pages 71 and 72.)

[175] Spikes, Hugh and Jie, ZhangHistory, origins and prediction of elastohydrodynamic friction. *Tribology Letters* **56**, 1–25 (2014). (Cited on pages 71 and 72.)

[176] Valencia-Jaime, Irais and Desgranges, Caroline and Delhommelle, JeromeViscosity of a highly compressed methylated alkane via equilibrium and nonequilibrium molecular dynamics simulations. *Chemical Physics Letters* **719**, 103–109 (2019). (Cited on page 71.)

[177] Jadhao, Vikram and Robbins, Mark OProbing large viscosities in glass-formers with nonequilibrium simulations. *Proceedings of the National Academy of Sciences* **114**, 7952–7957 (2017). (Cited on pages 71, 72, and 73.)

[178] Hansen, J.P. and McDonald, I.R. *Theory of simple liquids* (Elsevier Academic Press, 2006), 3 edn. (Cited on page 72.)

[179] Allen, M. P. and Tildesley, D. J. and Tildesley, D. J. *Computer Simulation of Liquids* (Oxford University Press, 2017). (Cited on page 72.)

[180] Dario Alfè and Michael J. GillanFirst-principles calculation of transport coefficients. *Physical Review Letters* **81**, 5161–5164 (1998). (Cited on page 72.)

[181] Pablo G. Debenedetti and Frank H. StillingerSupercooled liquids and the glass transition. *Nature* **410**, 259–267 (2001). (Cited on page 73.)

[182] Loose, W and Hess, SRheology of dense model fluids via nonequilibrium molecular dynamics: shear thinning and ordering transition. *Rheologica Acta* **28**, 91–101 (1989). (Cited on page 73.)

[183] Martin Kröger and Siegfried HessViscoelasticity of polymeric melts and concentrated solutions. the effect of flow-induced alignment of chain ends. *Physica A: Statistical Mechanics and its Applications* **195**, 336–353 (1993). (Cited on pages 73 and 74.)

[184] Janka Petravic and Jerome DelhommelleHydrogen bonding in ethanol under shear. *The Journal of Chemical Physics* **122**, 234509 (2005). (Cited on pages 73 and 74.)

[185] Vassiliy LubchenkoShear thinning in deeply supercooled melts. *Proceedings of the National Academy of Sciences* **106**, 11506–11510 (2009). (Cited on page 74.)

[186] Yuntao Xu and Collin J. Dibble and Nikolay G. Petrik and R. Scott Smith and Alan G. Joly and Russell G. Tonkyn and Bruce D. Kay and Greg A. KimmelA nanosecond pulsed laser heating system for studying liquid and supercooled liquid films in ultrahigh vacuum. *The Journal of Chemical Physics* **144**, 164201 (2016). (Cited on pages 76 and 77.)

[187] Yuntao Xu and Nikolay G. Petrik and R. Scott Smith and Bruce D. Kay and Greg A. KimmelGrowth rate of crystalline ice and the diffusivity of supercooled water from 126 to 262 K. *Proceedings of the National Academy of Sciences* **113**, 14921–14925 (2016). (Cited on page 77.)

[188] Yuntao Xu and Nikolay G. Petrik and R. Scott Smith and Bruce D. Kay and Greg A. KimmelHomogeneous nucleation of ice in transiently-heated, supercooled liquid water films. *The Journal of Physical Chemistry Letters* **8**, 5736–5743 (2017). (Cited on page 77.)

[189] Greg A. Kimmel and Yuntao Xu and Alexandra Brumberg and Nikolay G. Petrik and R. Scott Smith and Bruce D. KayHomogeneous ice nucleation rates and crystallization kinetics in transiently-heated, supercooled water films from 188 K to 230 K. *The Journal of Chemical Physics* **150**, 204509 (2019). (Cited on page 77.)

[190] Hajime TanakaSimple physical explanation of the unusual thermodynamic behavior of liquid water. *Physical Review Letters* **80**, 5750–5753 (1998). (Cited on page 77.)

[191] C. E. Bertrand and M. A. AnisimovPeculiar thermodynamics of the second critical point in supercooled water. *The Journal of Physical Chemistry B* **115**, 14099–14111 (2011). (Cited on page 77.)

[192] V. Holten and M. A. AnisimovEntropy-driven liquid–liquid separation in supercooled water. *Scientific Reports* **2** (2012). (Cited on page 77.)

[193] Vincent Holten and David T. Limmer and Valeria Molinero and Mikhail A. AnisimovNature of the anomalies in the supercooled liquid state of the mW model of water. *The Journal of Chemical Physics* **138**, 174501 (2013). (Cited on pages 77 and 85.)

[194] Singh, Rakesh S. and Biddle, John W. and Debenedetti, Pablo G. and Anisimov, Mikhail A.Two-state thermodynamics and the possibility of a liquid-liquid phase transition in supercooled tip4p/2005 water. *J. Chem. Phys.* **144**, 144504 (2016). (Cited on page 77.)

[195] Anders Nilsson and Lars G. M. PetterssonThe structural origin of anomalous properties of liquid water. *Nature Communications* **6** (2015). (Cited on page 79.)

[196] Espinosa, J. R. and Navarro, C. and Sanz, E. and Valeriani, C. and Vega, C.On the time required to freeze water. *J. Chem. Phys.* **145**, 211922 (2016). (Cited on pages 15, 16, 79, 82, 83, 84, 88, and 89.)

[197] Peter H Poole and Ivan Saika-Voivod and Francesco SciortinoDensity minimum and liquid–liquid phase transition. *Journal of Physics: Condensed Matter* **17**, L431–L437 (2005). (Cited on page 83.)